UC Merced
UC Merced Electronic Theses and Dissertations

Title
Periodic and Aperiodic Barriers to Reaction Front Propagation

Permalink
https://escholarship.org/uc/item/8d13c62t

Author
Locke, rory Alexander

Publication Date
2018

Peer reviewed|Thesis/dissertation

eScholarship.org
Powered by the California Digital Library
University of California

University of California, Merced

Dissertation

Periodic and Aperiodic Barriers to Reaction Front Propagation

by

Rory Locke

A technical report submitted
in partial fulfillment of the requirements for the degree of

Doctor of Philosophy in Physics

2018

Committee Members:

Professor Francois Blanchette

Professor Bin Liu

Professor Kevin Mitchell, Advisor, Chair

Chapter 2 © 2018 American Institute of Physics-Chaos

All other material © 2018 Rory Locke All rights reserved

The Dissertation of Rory Locke is approved, and it is acceptable
in quality and form for publication.

Committee Member:

Professor Bin Liu

Committee Member:

Professor Francois Blanchette

Research Advisor:

Professor Kevin Mitchell

Submission Date

Abstract

Periodic and Aperiodic Barriers to Reaction Front Propagation

by

Rory Locke

Doctorate in Physics

Kevin Mitchell, Chair

University of California, Merced

2018

Abstract

Fluid flows in which the particles passively advect and diffuse are common throughout nature. There are large volumes of work in the area of advection-diffusion however, despite the many applications to fluids flowing with a reaction component, no clear model of capturing front dynamics exists. Fronts propagating in two-dimensional advection-reaction-diffusion systems exhibit rich topological structure just like their advection-diffusion counterparts. It has been shown that invariant manifolds form barriers to passive transport in time-dependent or time-periodic fluid flows. Recently, analogous manifolds termed *burning*-invariant-manifolds (BIMs), have been shown to form one-sided barriers to reaction fronts in ARD systems. Here we apply the BIMs model to that of time-periodic flows. When the underlying fluid flow is time-periodic, the reaction front will often mode-lock to the driving frequency. This mode-locking phenomenon can be described by BIMs. In fact, the mode-locking front is exactly the BIM attached to a relative periodic orbit (RPO) of the front element dynamics. Changes in the type of mode-locking (and the loss of mode-locking) can be understood in terms of local and global bifurcations of these RPOs. In the first part of this thesis we illustrate the above concepts numerically using a chain of alternating vortices in a channel geometry.

In nature most flows are not time-independent or time-periodic but may have an unknown or aperiodic time dependence. Therefor we can no longer talk about infinite time structures like invariant manifolds and BIMs. In the field of advection-diffusion there exists a model for extracting coherent structures in time-aperiodic flows called Lagrangian Coherent Structures (LCSs). Recent theoretical work in ARD systems has suggested that similar one-sided barriers, termed *burning* Lagrangian coherent structures (bLCSs), exist for fluid velocity data prescribed over a finite time interval. In the second part of this thesis, we apply the bLCS model to a numerically generated flow with an aperiodic wind. The wind is used to generate time dependence in a double-vortex channel flow where we can then demonstrate that the (locally) most attracting or repelling curves are the bLCSs.

Finally we model an experimental flow performed by Solomon et. al [23]. The experiment utilizes a single vortex in a windy channel. In the reference frame of the vortex, a constant wind is blowing from left to right, while a swirling wind blows in the lateral direction. First we extract the BIMs for the steady, constant, left to right wind, then we show the time evolved BIMs for the fully unsteady case and comment on the validity of evolving the BIMs.

Acknowledgments

I gratefully acknowledge my advisor Kevin Mitchell for his mentorship and advice throughout this study, and for helping me improve myself as a researcher. I am thankful for committee members Francois Blanchette and Bin Liu for their continued feedback and advice on improving my work and its presentation. I acknowledge the support of the US National Science Foundation under grants PHY-0748828 and CMMI-1201236.

Preface

The thesis is intended to be a complete research report. However, an effort was made to keep the chapters independent from each other to facilitate their publication. Some chapters have or will be submitted for publication in their present forms:

- Locke, Mahoney and Mitchell. *Mode-locking in advection-reaction-diffusion systems: an invariant manifold perspective*, Journal of Chaos (2017)

Contents

Signature Page iii

Abstract **iv**

Acknowledgments **vi**

Preface **vii**

Table of Contents **viii**

List of Figures **x**

List of Tables **xxi**

Curriculum Vitae **xxiii**

1 Motivation and Background **1**

1.1 Chaotic Advection 2

1.1.1 Steady and time periodic flows-Invariant Manifolds 4

1.1.2 Unsteady Flows-Lagrangian Coherent Structures 7

1.2 Active enhancement of advective flows 10

1.2.1 Steady Flows-Burning Invariant Manifolds 10

1.2.2 Unsteady Flows-Burning Lagrangian Coherent Structures 14

1.3 Summary of Manuscript 18

2 Time Periodic barriers and Mode-locking 20

2.1 Introduction 20

2.2 Preliminaries 22

2.2.1 Front-element dynamics 22

2.2.2 Burning invariant manifolds (BIMs) and frozen fronts 23

2.3 Mode-Locking 25

2.3.1 Numerical Simulations 25

2.3.2 Mode-locked fronts are composed of BIMs 29

2.4 Changes in mode-locking as v_0 is increased. 33

3 Time Aperiodic 37

3.1 Introduction 37

3.2 Preliminaries 38

3.2.1 Front-element dynamics 38

3.2.2 Burning Lagrangian Coherent Structures (bLCSs) 39

3.3 Numerical Simulations 44

3.3.1 Linear time varying wind 44

3.3.2 Stochastic Time Varying Wind 54

3.3.3 Stochastic Time Varying Wind-sliding window 61

3.4 BLCS(s) as finite time barriers to ARD systems. 63

3.4.1 Bounding Nature of BLCSs 63

4 Experimental Application to Unsteady Active flow 66

4.1 Introduction 66

4.2 Reproducing Velocity Fields 67

4.3 Numerical Simulations 68

4.3.1 Convergence 70

4.3.2 Aperiodic Forcing 70

5 Summary and Future Work 77

5.1 Summary 77

5.2 Future Work 78

6 Appendix **80**

6.1 Mode Locking - Numerical computation of RPOs 80

6.1.1 Multishooting approach 80

6.1.2 Choosing initial seeds 81

6.2 bLCS - Numerical Techniques for bLCS extraction. 83

6.2.1 Boostrapping 83

6.2.2 Artificial Dissipation 83

List of Figures

1.1 Numerical simulation of steady double gyre. Initial sample of fluid particles shown in blue and subsequent samples shown as time moves forward under the flow. The initial sample is both advected along while being stretched. Fixed points lie at the channel boundary at $(0,0)$ and $(0,1)$. The unstable manifold of these fixed points is shown in red. The unstable manifold serves as a separatrix between the two vortices. Fluid particles can not pass from the left to right of the separatrix and vice versa, thus the unstable manifold forms a barrier to fluid particles. 5

1.2 Time periodic double gyre with lateral oscillations, eq. 1.8. The unstable manifold (red), now has more complicated structure, and intersects with the stable manifold(blue). Also notice how the fixed points themselves have shifted and that the manifolds are now only attached to one hyperbolic fixed point on the channel wall. These lobes formed by the intersection of the stable and unstable manifolds now provide a means of long range transport and a much more efficient means of mixing. 7

1.3 LCSs in the double gyre. (a) Shows the elliptic LCSs in green along with the attracting LCSs in blue. (b) Shows the elliptic LCSs in green and the repelling LCSs in red. 9

1.4 A front is defined as the oriented boundary between reacted and unreacted regions where the local orientation vector $\hat{\mathbf{n}}$ is normal to the reaction front and points *away* from the burned region. If $\mathbf{r}$ is used to denote the xy-position of a front element and θ as the angle between the positive x-axis and $\hat{\mathbf{g}}$, each front element, specified by $(\mathbf{r}(t), \theta(t))$, evolves via eq. (1.10) 11

1.5 Numerical simulation of steady double gyre with an active enhancement. Initial reaction stimulation shown in blue and subsequent samples shown as from blue to red as time moves forward under the flow. The separatrix in the purely advective case has split into two *burning* fixed points with one burning to the left and the other to the right. The unstable *burning* invariant manifolds are shown in red with their burning direction noted by the red arrows. The BIMs are one sided barriers to reaction fronts propagating in the same direction. (a) shows an initial reaction stimulation in between the two BIMs. Here the fronts are confined between the BIMs as the reaction front propagates outward since the front propagation direction is the same as the burning direction for each BIM. (b) shows an initial reaction stimulation on the right side. As the front propagates it is able to pass through the first BIM since its burning direction is opposite to the direction the front is propagating. The front however is blocked by the second, leftmost, BIM since its burning direction is the same as the front propagation direction. (c) shows an initial reaction stimulation on the left hand side, the blocking (non-blocking) nature of the BIMs follows the same reasoning as (b). 12

1.6 Numerically generated reaction front showing evidence of mode-locking. The front propagates down the channel from left to right starting with a vertical front spanning the channel. After one period the front has fully converged. Fig. 1.6 (a)-(c) shows mode-locking of types (1,1), (1,2), and (2,3) with v_0 = 0.18, 0.068, and 0.089 respectively. Dashed vertical lines indicate the vortex cells. 14

1.7 Given an initial front, a small normal displacement of a front element, $\epsilon\hat{n}$, evolves under F to a vector $\epsilon\mathbf{v}$. This new evolved front element will in general have a nonzero tangential component. We define the Lagrangian shear p over time interval t to be the projection of $\epsilon\mathbf{v}$ in the tangent direction divided by ϵ. Similarly we define the normal repulsion ρ to be the projection of $\epsilon\mathbf{v}$ in the normal direction divided by ϵ. 15

1.8 (a) Family of sheerless curves in $xy\theta$-space. Black line shows line of initial conditions and black curve shows the BIM. (b) Two dimensional projection of the family of sheerless curves in xy-space. (c) Comparison of the BIM (black) and the sheerless curve chosen as the bLCS (red), Inset shows the average normal repulsion curve as a function of the initial conditions x coordinate with the bLCS circled in red. 15

1.9 (a) Sheerless surface in $xy\theta$-space. (b) Two dimensional projection of the sheerless surface in xy-space. The coloring corresponds to the value of the normal repulsion, red being a positive value and blue denoting a negative value. 17

2.1 Experimental images of the Belousov-Zhabotinsky reaction in a quasi-two-dimensional alternating vortex channel flow. The flow is driven by an electric current passing through the fluid over a row of magnets. Left: Experimental image of mode-locking type (1,2). It takes two driving periods for the “b”-shaped front profile to repeat itself shifted by one pair of vortices. Right: Experimental image of mode-locking type (1,1) [48]. 21

2.2 (a) An initial circular burned region at $t = 0T$. Panels (b)-(d) show the forward evolution at times $t = 0.3T, 0.6T$, and $1.19T$ respectively. The front is evolved using Eq. (2.4) with v_0= 0.2 and $\mathbf{u}$ given by Eq. (3.3), with $b = 0.25$, and $\omega = 2$. . 24

2.3 Numerically generated reaction front showing evidence of mode-locking. The front propagates down the channel from left to right starting with a vertical front spanning the channel. After one period the front has fully converged. Fig. 2.3 (a)-(c) shows mode-locking of types (1,1), (1,2), and (2,3) with v_0 = 0.18, 0.068, and 0.089 respectively. Dashed vertical lines indicate the vortex cells. 26

2.4 Simulation demonstrating convergence of fronts to mode locking. (1,1) mode-locking with fronts shifted backwards showing convergence to be approximately one period. The initial condition is shown as the straight vertical line. The inset shows the rightmost point of the front as a function of the number of iterates. Beginning with the initial front we see it takes no more than two iterates to reach the mode-locked state. 27

2.5 Reaction front shows evidence of (1,1) mode locking with $v_0 = 0.18$. The front evolves from left to right down the channel beginning with a fully converged front, black curve on the left, and then evolving forward over one period where the shape of the front repeats itself one period later, black curve on the right. 28

2.6 Simulation of (1,2) mode-locked front propagating down the channel for two periods. 28

2.7 Simulation of (3,5) mode-locked front propagating down the channel for nine periods. 28

2.8 Simulation of (1,1) mode-locking demonstrates the extreme stretching experienced by the bounding front under the map $F^{(1,1)}$. Blue bounding front (a) maps to blue front (b). Small red segment (a) maps to red bounding front (b). 29

2.9 (a) Mode-locked front with RPO in red. The front has a swallowtail that extends into the burned region. Here the bounding front is composed of two segments only one of which has the RPO. (b) Mode-locked front with RPO in red, and a void (unburned region) trapped behind the bounding front. If an RPO of another type were present on any segment of the front that encompasses the void it would not persist indefinitely. All the unburned material behind the bounding front will become burned thus it is not possible to have two simultaneous mode-locking types. 31

2.10 Bifurcation diagram of the RPOs as a function of v_0. Multiple RPOs exist for the same parameters. Average front speed of dominant ML front (Eq. 2.2) is monotonic in v_0. Insets shows that each ML RPO is created in a saddle-node bifurcation. . . . 33

2.11 The mechanism by which the (1,2) mode-locked front loses its domanince with $v_0 = 0.0873$. (a) At $t = 0$ the RPO sits near the channel boundary. (b,c) The RPO moves upward while the front develops a long “finger” along the top boundary. (d) The RPO moves up, colliding with the “finger”. Oppositely oriented fronts can interpenetrate. (e) Final frame shows a bounding front with multiple components. This RPO is no longer on the bounding front, and therefore not the RPO associated with the dominant mode-locking type. 36

3.1 A front is defined as the oriented boundary between reacted and unreacted regions where the local orientation vector $\hat{\mathbf{n}}$ is normal to the reaction front and points *away* from the burned region. If $\mathbf{r}$ is used to denote the xy-position of a front element and θ as the angle between the positive x-axis and $\hat{\mathbf{g}}$, each front element, specified by $(\mathbf{r}(t), \theta(t))$, evolves via eq. (2.4) 38

3.2 Given an initial front, a small normal displacement of a front element, $\epsilon\hat{n}$, evolves under F to a vector $\epsilon\mathbf{v}$. This new evolved front element will in general have a nonzero tangential component. We define the Lagrangian shear p over time interval t to be the projection of $\epsilon\mathbf{v}$ in the tangent direction divided by ϵ. Similarly we define the normal repulsion ρ to be the projection of $\epsilon\mathbf{v}$ in the normal direction divided by ϵ. 40

3.3 (a) Shearless surface in $xy\theta$-space. (b) Two dimensional projection of the shearless surface in xy-space. The coloring corresponds to the value of the normal repulsion, red being a positive value and blue denoting a negative value. 42

3.4 (a) Family of shearless curves in $xy\theta$-space. Black line shows a line of initial conditions and black curve shows the BIM. (b) Two dimensional projection of the family of shearless curves in xy-space. (c) Comparison of the BIM (black) and the shearless curve chosen as the bLCS (red), (inset) shows the average normal repulsion curve as a function of the initial condition's x coordinate with the bLCS circled in red. 43

3.5 Fluid flow derived from the stream function eq. 3.14. The flow takes place in an infinitely long channel with two counter rotating vortices centered at $x = 0$. The channel height is $y = 1$, thus the vortex height and width are unit 1. The black arrows show the direction of rotation of the vortices. The red and blue curves are the unstable and stable burning invariant manifolds respectively. The arrows along the BIMs show their burning direction. This particular image corresponds to a γ value of 1, and $v_w = 0.15$. 44

3.6 Wind speed profile for linearly decreasing wind speed. The wind speed begins with a value of $v_w = -0.15$ and decreases linearly over a time interval $[0, 6]$ to a value of $v_w = -0.1$. It is then held constant at $v_w = -0.1$ from $[6, 10]$. Physically, this corresponds to a wind blowing across the channel from right to left decreasing in magnitude. 45

3.7 Time-independent burning invariant manifolds for constant wind speeds of $v_w = -0.15$ (left) and $v_w = -0.1$ (right). BIMs are generated using eq. 3.2 and take place in a long channel with two side-by-side counter rotating vortices, fig. 3.5. 45

3.8 Histogram of how data is generated. First the domain is discretized into a uniform grid. Within this domain a reaction is stimulated and evolved forward over some time interval. Next which grids the front propagates to is recorded. This process is repeated for many randomly selected reaction stimulations. Finally a histogram is formed which show areas of highest attraction or front accumulation. 46

3.9 Histogram of evolved front stimulations over a time interval $[0, 8]$. There are three regions of highest attraction shown as the yellow curves. The middle curve lies between the BIMs in Fig. 3.7 as expected. 47

3.10 (a) Beginning with a single initial condition, the red line is generated by integrating Eq. 3.8 producing a line of initial conditions. With these, the shearless curves are obtained by integrating Eq. 3.10 for some distance. (b) A plot of the average normal repulsion along each of the shearless curves. We choose as our bLCS the one that maximizes the average normal repulsion, (red point), which corresponds to the black curve in the family of shearless curves. 48

3.11 Histogram of evolved front stimulations over a time interval $[0, 8]$ with our chosen candidate for the bLCS in black. This was found following the method in laid out in Sec. 3.2.2. The black curve shows good agreement with the underlying region of highest attraction. 49

3.12 The shearless surface from $x = [-0.25, 0.25]$, $y = [0, 1]$ and $\theta = [1.45, 2]$ over time interval $CGT = [0, 8]$. The burning fixed point of the BIM in fig. 3.7 has a value of $\theta = \pi/2$, therefore we know apriori the corresponding branch of the shearless surface the bLCS should lie within. The colormap is scaled with the value of θ. . . 50

3.13 Histogram of evolved front stimulations over a time interval $[0, 10]$ with our chosen candidate for the bLCS in black. This was found following the method in laid out in Sec. 3.2.2. The black curve shows good agreement with the underlying region of highest attraction. 51

3.14 The shearless surface from $x = [-0.25, 0.25]$, $y = [0, 1]$ and $\theta = [1.45, 2]$ over time interval $CGT = [0, 10]$. The colormap is scaled with the value of θ 52

3.15 Evolution of bLCS under F. Statistical plot for an integration time of $t_1 = 10$. The blue curve, the bLCS extracted for $t_1 = 8$, was evolved forward one time unit to $t_1 = 9$ resulting in the red curve. Evolving the blue curve two time units, or red curve one time unit, forward results in the black curve and ultimately the same result from Fig. 3.13. 53

3.16 Comparison of shearless surfaces for (a) $CGT = [0, 8]$ and (b) $CGT = [0, 10]$ . . 54

3.17 Wind profile for a stochastic wind over a time interval $[0, 8]$. This profile is piecewise linear with speeds above and below the burning speed $v_0 = 0.1$. This resembles a swirling wind that changes direction blowing initially from left to right up until $t = 4$, then right to left from $t = 4$ to approximately $t = 6$, and finally back from left to right. 55

3.18 Histogram of front stimulations over a time interval $[0, 8]$ with the stochastic wind profile in fig. 3.17. There are three region of highest attraction like in the linearly decreasing wind in 3.3.1, but with noticeable differences. The structure on the left extends further up the channel as expected from a wind profile that on average blows from left to right. The structure on the right has also shifted right. 56

3.19 Constraint surface $t_1 = 8$. Here the shearless surface is growing quickly in complexity thus a shorter CGT was chosen to extract the bLCS.The colormap is scaled with the value of θ 57

3.20 The bLCS(s) extracted for $CGT = [0, 6]$ in blue. Evolving the blue bLCS forward one time step results in the red curves, i.e. $CGT = [0, 7]$. Finally evolving forward one more time step results in the black curves, $CGT = [0, 8]$ 58

3.21 Wind profile for a stochastic wind over a time interval $[0, 15]$. This profile is piecewise linear with speeds above and below the burning speed $v_0 = 0.1$. This resembles a swirling wind that blows on average from left to right. 59

3.22 Histograms for stochastic wind (a) $[0, 5]$, (b) $[0, 10]$, and (c) $[0, 15]$. 60

3.23 Stochastic wind shearless surface (a) $CGT = [0, 5]$, (b) $CGT = [0, 10]$, and (c) $CGT = [0, 15]$. 61

3.24 Histograms for stochastic wind (a) $[0, 5]$, (b) $[0, 10]$, and (c) $[0, 15]$ with bLCSs in black. 62

3.25 Bounding nature of bLCS for linear TV wind time interval $[0, 10]$. (a) shows point stimulations on the left side of the bLCS. (b) shows the evolution of the stimulations is (a). As expected the bLCS bounds the reactions stimulated on the left and serves as a one-sided barrier. (c-d) show the initial stimulations and their evolution. Here the reaction is stimulated to the right of the bLCS and as expected the evolution of those stimulations pass through the bLCS and fill the fluid domain. Therefore, the bLCS serves as a one-sided barrier to reaction fronts in unsteady flows in the same way that BIMs are one-sided barriers in steady flows. 63

3.26 Wind profile to $t = 25$. The same profile used in Fig. 3.21 extended by 10 more time units where the magnitude was held above v_0 64

3.27 Cusp in bLCS for stochastic wind CG $t = 20$. 64

4.1 Streamlines for the velocity field with $v_w = 0.69$. 68

4.2 Velocity field for eq. 4.1. (a) shows the velocity field with constant streamlines. (b) shows the same velocity field with the passive invariant manifold in red. 69

4.3 Numerical simulation using eq. 4.1 with active enhancement. BIMS shown with burning speeds (a) $v_0 = 0.024$, $(b)0.095$, and (c) 0.19 respectively. 69

4.4 Numerical simulations of steady flow with (a) BIM along with passive invariant manifold for a burning speed of $v_0 = 0.048$, and (b) front accumulation plot for $v_0 = 0.048$ with the BIMs shown in black. This simulation was run from $t_0 = 0$ to $T = 200$. 69

4.5 Numerical simulations of a point stimulation at the advective fixed point for the steady case of $U = 0.14$ cm/s, $w = 0.69$ and $v_0 = 0.048$. (a) Shows the point stimulation evolved forward from $t_0 = 0$ to $T = 100$. Interestingly we see that the front propagates downwards towards the center of the vortex farther than out and away from the vortex. (b) Shows the point stimulation evolved forward from $t_0 = 0$ to $T = 200$, here the front swiftly moves around the vortex center in the region bounded by the BIMs until either propagating outwards or further propagating towards the center. 71

4.6 (a) The lateral (up and down) aperiodic oscillations of the vortex over time. (b) The corresponding wind speed profile in lateral direction. Note that a negative velocity of the vortex corresponds to a wind blowing in the positive direction in the reference frame of the vortex. The labels in (a) correspond to the snapshots in time taken in fig. 4.7. 71

4.7 Reaction fronts in a vortex flow with aperiodic time dependence. Here the parameters are $U = 0.14$ cm/s, $w = 0.69$, $v_0 = 0.048$. The lateral oscillations have a range of 2.2cm and a standard deviation of 0.68 cm. A graph of the displacement versus time is shown in fig 4.6(a) with the corresponding snapshots labeled. This image take from Solomon et. al. [23]. 73

4.8 Front accumulation plots for an unsteady flow. The flow was produced by the aperiodic forcing shown in fig. 4.6. (a) shows the front accumulation at $T = 5$s. (b)-(d) show front accumulations for $T = 15$s, 25s and 35s respectively. 74

4.9 Front accumulation plots for an unsteady flow and evolved BIMs. (a) shows the front accumulation at $T = 5$s. (b)-(d) show front accumulations for $T = 15$s, 25s and 35s respectively. 75

6.1 Multishooting: The diamonds represent the seeds. These points are mapped forward under F with the assumed mode-locking type, $(2,3)$ in this example, resulting in the circles. The last point is then shifted back by $2N$ vortices. Finally to find the RPOs we take the difference between the initial and mapped forward points and use Newton's method to find the roots of this difference map. 81

6.2 Seed Finding. Panel (a) shows mode-locking of type (1,2). The blue front is mapped forward for two periods resulting in the red and black fronts, respectively. The tiny rectangle on the blue front in (a) encompasses the points that, once mapped forward, comprise the red and black fronts. Panel (b) shows the zoomed in region in (a). Here a new rectangle encompasses the region where the black front originates. Panel (c) shows the zoomed in region in (b). The black point remaining in (c) is a good starting seed for one of the two points of the RPO. 82

6.3 Numerical simulation demonstrating the bootstrapping algorithm. Initial segment was chosen at the bottom and integrated upwards with respect to the channel. For each line of initial conditions, shown are red points, the tangent vector field along the sheerless surface was integrated for a short segment. The curve which maximized the normal repulsion was chosen as the bLCS segment for that family of curves. The last point of the bLCS segment was then used to integrate the normal vector field in both directions for a line of initial conditions. From those initial conditions a new family of curves was found integrating the tangent vector field and the process was repeated for multiple segments until the bLCS of interest was extracted. 84

6.4 (a) shows the statistical plot for $T = [8, 0]$ along with the bLCS segment in black, and the lines of initial conditions in red for each bootstrapping segment. (b) shows an inset to the statistical plot in (a) zoomed into the lower portion of the bLCS segment. Figure 6.4(c-d) shows the average normal repulsion for segments 18 and 19 respectively. (c) has a clear maximum in the normal repulsion and thus a clear candidate for a bLCS segment. (d)Going one iteration further in the boostrapping algorithm, a family of sheerless curves is found however, no clear candidate sheerless curve is identified as having a maximum normal repulsion. . . . 85

6.5 Lifting from the sheerless surface using bootstrapping algorithm. Initial condition at top of the channel near $y = 0.75$ was found using newton's method. An increasing deviation from the sheerless surface was found after each subsequent segment was integrated towards the bottom. Integrating from $y = 0.75$ to $y = 0.2$, it was clear from the value of Psi the segments were no longer on the sheerless surface. 86

6.6 Using Newton's method on new initial condition for each bootstrapped segment. If there are many neighboring branches of the sheerless surface, using newtons method may result in jumping branches, or folds, of the sheerless surface and thus not extract the single bLCS of interest. 87

List of Tables

Curriculum Vitae

Education

2013–present PhD, Physics specializing in coherent structure detection techniques in dynamical systems.
Advised by Prof. Kevin Mitchell.
University of California, Merced. Merced, CA.

2009–2012 BS, Physics.
Middle Tennessee State University, Murfreesboro, TN

Publications

- Locke, Mahoney and Mitchell. *Mode-locking in advection-reaction-diffusion systems: an invariant manifold perspective*, Journal of Chaos (2017)

Teaching Experience

2013–2018 Teaching Assistant, Intro. Physics 1/2, Calculus 1/2
University of California, Merced. Merced, CA.

2018–present Full-time Lecturer, Intro. Physics 1, Astronomy 1031
Middle Tennessee State University, Murfreesboro, TN

Chapter 1

Motivation and Background

A dynamical system can be thought of as any system one wishes to model over time. How the systems evolves over time, whether it settles down to an equilibrium state or not does not matter, only the dynamics are used to analyze the behavior. Examples of a dynamical system include modeling the growth of population over time, the current or charge through an electronic circuit, or the oscillation of a mass on a spring. Remarkably, dynamical systems theory has universal properties that apply to large classes of systems irrespective of physical phenomena and scale.

The theory of dynamical systems began with the work of Issac Newton and his model of the Earth-Sun system which resulted in his law of gravitation. It took a different turn after many failed attempts at modeling the three-body problem when Henry Poincare introduced his geometric approach to modeling dynamical systems. He posed a different question, what if instead of being concerned with exact quantities, i.e. precise position of the moon in the Sun-earth-moon system at all times, we were only concerned with the long term behavior? Does the system settle down into an equilibrium or will the moon eventually leave our solar system? Poincare also first noticed that a particular set of dynamical systems exhibited aperiodic behavior that can exhibit a sensitivity to initial conditions. This sensitivity stems from an exponential growth of perturbations to the initial conditions. These nonlinear systems are termed chaotic as the sensitivity leads to a seemingly random behavior. Another way to describe chaotic systems is as nonintegrable, where integrability fails because the integrand jumps around too much. These questions and difficulties lead to an important concept in dynamical systems called the phase space.

The phase space is the set of all possible states a trajectory can have in a dynamical system. Phase spaces can tell us things about solutions to a dynamical system in a qualitative manner. For instance, does this system have any equilibrium points (fixed points) at which the system will settle down? Once fixed points are established, if any exist, they can be used to determine stable and unstable directions. The stable (unstable) sets of a fixed point in a dynamical system are loosely defined as those points which converge to the fixed point in forwards (backwards) time. This is done through a linearization of the system, which under relatively mild conditions allows us to relate the (un)stable sets (manifolds) of the non-linear system to those of the linearized system. The geometry of the stable and unstable manifolds of the fixed points encode important information about the system's dynamics. In this manuscript we will apply these and similar techniques of dynamical systems to chaotic advection with an active enhancement.

1.1 Chaotic Advection

Mixing and transport in fluids is an extremely important processes that occurs in many phenomena over a wide range of length scales. Examples of mixing and transport range from microfluidic mixing and transport in microbiology [7, 10, 21], to mixing in the Earth's mantle [29] and astrophysics [16, 20, 61]. The dispersion of contaminants in the ocean has certainly been an area of interest over the last decade with the disasters from the British Petroleum oil spill and the aftermath of the tsunami that caused the Fukushima nuclear disaster. Therefore having a model to predict transport and mixing is important for many applications from industrial to environmental.

Historically it was first believed that laminar flows were completely deterministic, and that turbulent flows could only be specified by a probabilistic velocity field [51, 59]. It is now known from the theory of dynamical systems that the solutions of deterministic equations can be chaotic in the sense of exponential sensitivity to small variations of initial conditions and parameters. A simple velocity field can result in chaotic fluid particle trajectories. [6, 13]. Although two dimensional steady flows are integrable and will not result in chaotic particle trajectories, two-dimensional unsteady flows or, three-dimensional steady flows, in general, are not integrable. The subject of chaotic advection is based on this non-integrability and many studies of stirring and mixing are based on the assumption that chaotic advection is present. Let us first clarify what is meant by advection of a particle.

A particle suspended in a fluid moving with some velocity is "passively" advected along. Passively in that the particle is presumed so light and powerless that it has no choice but to adjust it's velocity to that of the fluid. The velocity of the particle, neglecting molecular diffusion, can thus be written

$$V_{particle} = V_{fluid}\Big|_{x_p,y_p,z_p}. \tag{1.1}$$

In a three-dimensional fluid flow with a Cartesian coordinate system we may therefore write

$$V_{particle} = (\frac{dx_p}{dt}, \frac{dy_p}{dt}, \frac{dz_p}{dt}). \tag{1.2}$$

The fluid velocity, V_{fluid}, is derived from solving a set of other equations, i.e. Navier-Stokes, or Stokes. With respect to chaotic advection we may assume that these were prescribed and we are given the component velocities u, v, and w. Thus we may write

$$V_{fluid} = [u(x,y,z,t), v(x,y,z,t), w(x,y,z,t)]. \tag{1.3}$$

Looking back at Eq.1.1 and plugging in Eqs.1.2 and 1.3 we find a systems of ordinary differential equations

$$\dot{x} = u(x,y,z,t), \tag{1.4a}$$

$$\dot{y} = v(x,y,z,t), \tag{1.4b}$$

$$\dot{z} = w(x,y,z,t), \tag{1.4c}$$

In modeling fluids, one may represent a flow where individual particles are tracked, Lagrangian method, or through the use of fields, Eulerian method. Here since we have derived eqs. 1.4 for that of a particle, we are using the Lagrangian approach. Thus eqns. 1.4 are simply the advection equations that, under certain situations, may be chaotic.

If the system two dimensional and incompressible i.e.

$$\nabla\cdot \mathbf{u} = 0 \tag{1.5}$$

then we may write

$$\dot{x} = -\frac{\partial \Psi}{\partial y}, \tag{1.6a}$$

$$\dot{y} = \frac{\partial \Psi}{\partial x}, \tag{1.6b}$$

where x, and y denote the spatial coordinates of the fluid flow and Ψ is the streamfunction. It is well known that this is analogous to a one dimensional Hamiltonian systems where the streamfunction Ψ plays the role of the Hamiltonian and the $-y$ coordinate the role of the conjugate momentum [8]. The lines in which $\Psi =$ constant are called streamlines, which in terms of dynamical systems, are invariant manifolds. In steady flows, any point that begins on a streamline (manifold) will remain on the streamline (manifold), thus these structures are act as barriers within a fluid flow and serve as a good template for studying the fluids motion. For this manuscript we assume incompressibility and thus can derive the fluid velocity from a streamfunction.

1.1.1 Steady and time periodic flows-Invariant Manifolds

In the case of two dimensional incompressible steady fluid flows, the Hamiltonian is integrable thus fluid particle trajectories are not chaotic. The streamlines are closed, forming invariant tori. The stable and unstable manifolds stem from hyperbolic (saddle) fixed points having one stable and one unstable direction. The unstable manifold forms a separatrix between the two vortices. Fluid particles can not pass from the left to right of the separatrix and vice versa, thus the unstable manifold forms a barrier to fluid particles. To demonstrate this we look at a simple example of two side-by-side counter rotating vortices. The stream function for this system is given by

$$\Psi = \frac{U}{\pi}\sin(\pi x)\sin(\pi y) \tag{1.7}$$

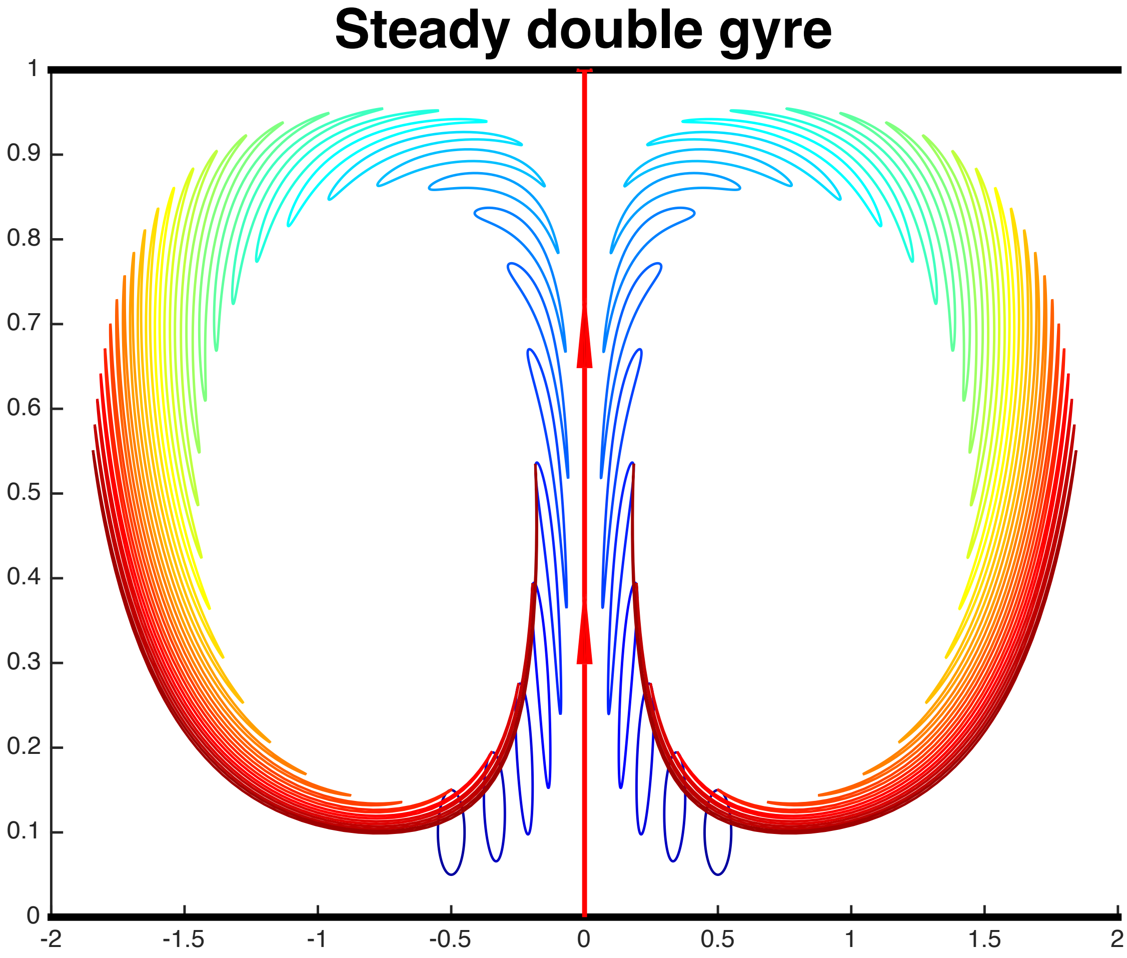

Figure 1.1. Numerical simulation of steady double gyre. Initial sample of fluid particles shown in blue and subsequent samples shown as time moves forward under the flow. The initial sample is both advected along while being stretched. Fixed points lie at the channel boundary at $(0, 0)$ and $(0, 1)$. The unstable manifold of these fixed points is shown in red. The unstable manifold serves as a separatrix between the two vortices. Fluid particles can not pass from the left to right of the separatrix and vice versa, thus the unstable manifold forms a barrier to fluid particles.

where it is scaled by U the maximum fluid velocity, and the height and width of the vortex is one. The term $\sin(\pi y)$ accounts for boundary conditions where here we have assumed them to be free slip. Figure 1.1 shows a simulation of a steady double gyre. The fixed points, where the x and y components of velocity are zero, lie at the top and bottom of the channel at $(0, 0)$ and $(0, 1)$. The unstable manifold of the bottom fixed point forms what is called a separatrix, dividing the channel into left and right halves. Fluid particles on the left side cannot pass the unstable manifold and reach the right, and vice versa, thus the unstable manifold is a barrier to fluid particles. Mixing in this case is not possible in the purely advective case. In a realistic flow diffusion would provide a means of transport from one vortex to the other albeit this would produce extremely slow mixing.

If the fluid flow is time-periodic, the flow may be nonintegrable and chaos ensues, despite the fact that the flow is still laminar, two-dimensional, and incompressible. The dynamics of such a system is typically best studied using a Poincare map. The time-independent invariant manifolds, separatrices, split into distinct, but intersecting, stable and unstable manifolds each attached to one hyperbolic fixed point on the channel wall. These intersections are formed by what are called heteroclinic and homoclinic orbits. Heteroclinic orbits begin and end at different fixed points, while homoclinic orbits begin and end at the same fixed point. The heteroclinic and homoclinic orbits result in complicated tangles, lobes formed by the intersecting manifolds allow advection between regions. A small perturbation of the time-independent fixed points, by some periodic time dependence, will result in better mixing and long range transport [18, 33, 57, 58, 62]

Time-periodicitiy is easily generated in the previous double-gyre example by oscillating the vortices from side to side. The stream function for that case is given by

$$\Psi = \frac{U}{\pi}\sin(\pi(x + B\sin(\omega t)))\sin(\pi y) \tag{1.8}$$

The term $x + B\sin(\omega t)$ accounts for the lateral oscillation of the vortices with amplitude B and frequency ω. An example of this can be seen in fig 1.2. The time-independent separatrices, unstable manifold (red), now has more complicated structure, intersecting with the stable manifold(blue). Also notice how the fixed points themselves have shifted and that the manifolds are now only attached to one hyperbolic fixed point on the channel wall. These lobes formed by the intersection

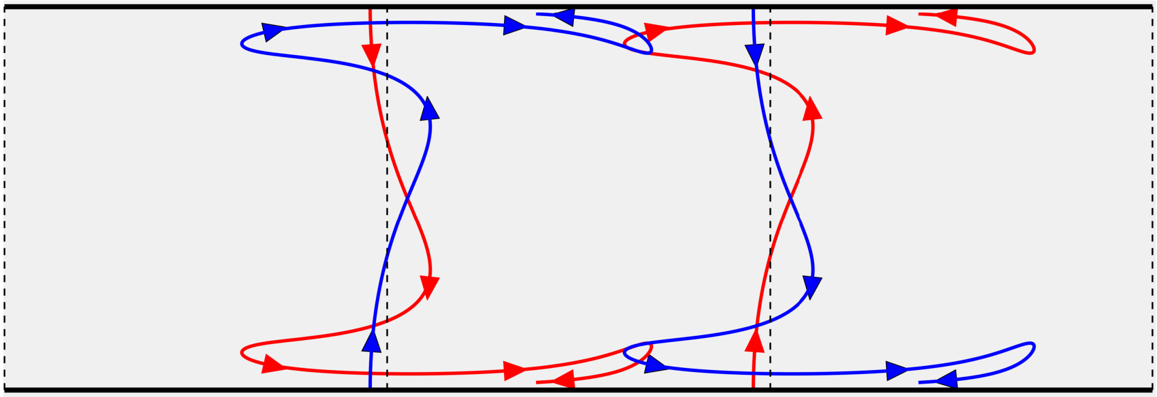

Figure 1.2. Time periodic double gyre with lateral oscillations, eq. 1.8. The unstable manifold (red), now has more complicated structure, and intersects with the stable manifold(blue). Also notice how the fixed points themselves have shifted and that the manifolds are now only attached to one hyperbolic fixed point on the channel wall. These lobes formed by the intersection of the stable and unstable manifolds now provide a means of long range transport and a much more efficient means of mixing.

of the stable and unstable manifolds now provide a means of long range transport and a much more efficient means of mixing.

1.1.2 Unsteady Flows-Lagrangian Coherent Structures

Time independent and time-periodic flows can be modeled with dynamical systems tools such as invariant manifolds and Poincare maps as outlined above, but what about more realistic flows found in nature? Most flows will have some arbitrary time dependence in which the time dependence is not analytic or is unknown. Velocity fields can be found through either computation fluid dynamics or from data attained by particle tracking, but what can be said about the overall structure of the underlying fluid flow? While a dynamical system is considered as any system that we wish to model over some finite time, this is somewhat of an oxymoron in that most mathematicians describe dynamical systems theory as the study of a system over time but in the asymptotic limit as time goes to infinity. Thus invariant manifolds are infinite ti me structures found by some iterative method in the limit as time goes to infinity. It may seem clear then that any dynamical systems analysis will not work for flows over a finite time interval, however, these geometric structures are seen along with the dynamical consequences in numerical simulations that are in fact carried out over finite time intervals [38]. The persistence of these geometric structures over the length of time we have knowledge of the underlying flow, demonstrates that the structures still exist. Therefore there is a need to develop analogous finite time tools for dynamical systems analysis.

The topic of Lagrangian based coherent structures has been a rapidly growing area of research in nonlinear dynamics for almost two decades. It provides a means to rigorously define and detect transport barriers in dynamical systems with arbitrary time dependence [5, 49]. Many different methods for Lagrangian based coherent structure detection have been developed in recent years and a comparison of these methods was recently performed showing their strengths, weaknesses and shortcomings [24]. Of particular interest to this manuscript, is the method of Lagrangian Coherent Structures (LCS) developed by Haller et. al. [25, 27]. Haller initially proposed that ridges of the finite-time Lyapunov exponent (FTLE) are heuristic indicators of hyperbolic (i.e., repelling and attracting type) LCSs. This makes sense intuitionally in that the Lyapunov exponent is a measure of the separation between neighboring trajectories, and if these trajectories are separating exponentially then there must be some "repelling" structure in between. These repelling structures can be seen as ridges in a plotof the FTLE field. However, FTLE ridges can yield both false negatives and false positives in LCS detection. Haller gives four explicit examples of dynamical systems in which there are observable LCSs and no FTLE ridges, observable FTLE ridges and no LCSs, where there is flux across a FTLE ridge, and where FTLE ridges are far from anything Lagrangian [26]. Thus a new approach of LCS detection was warranted. In the same paper, Haller outlines a variational theory for hyperbolic LCSs in which he equates LCSs with invariants of the Cauchy-Green strain tensor field. This variational technique locates LCSs as material surfaces that point-wise extremize the normal repulsion ratio of all nearby material surfaces. A numerical tool, LCS tools was released for computing LCSs using MATLAB [46]. A result of running the demo script of a double gyre is shown in fig. 1.3. Here the computed elliptic LCSs are shown in green, the attracting LCSs in blue and the repelling LCSs in red. These simulations use the latest variational technique by Haller et al. We base our approach of finding similar finite time structures in flows with an active enhancement.

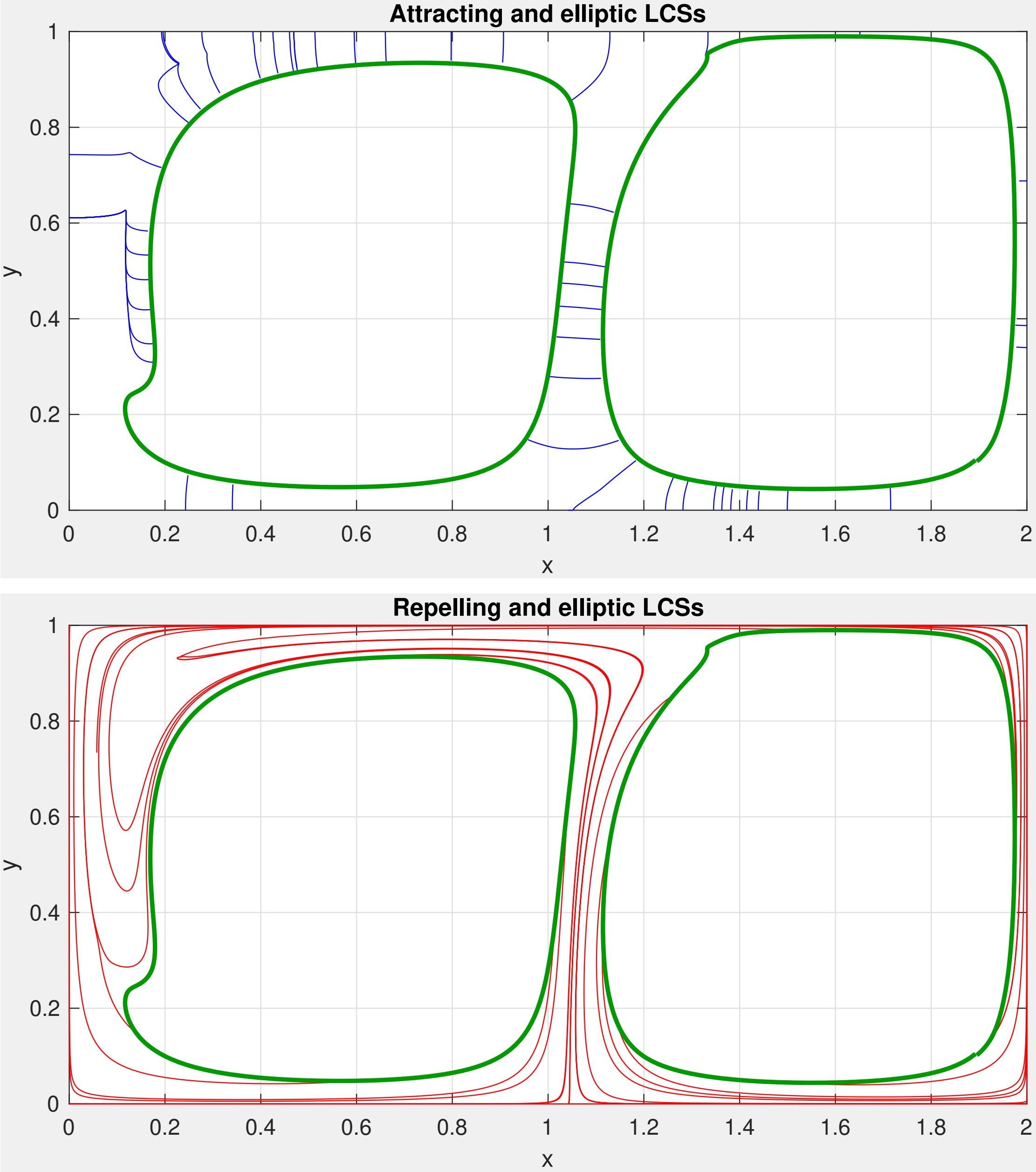

Figure 1.3. LCSs in the double gyre. (a) Shows the elliptic LCSs in green along with the attracting LCSs in blue. (b) Shows the elliptic LCSs in green and the repelling LCSs in red.

1.2 Active enhancement of advective flows

Chaotic advection of passive particles has been well studied since being formally defined by Aref in 1984. However, there are numerous examples in which flows also have a biological or chemical process that is occurring while the flow is advecting and diffusing. Examples include plankton blooms in the ocean [3, 4, 11, 12, 54], chemical reactions [40, 41, 60] and plasmas [9]. Despite this fact, no clear model of advection-reaction-diffusion (ARD) systems currently exists. Here we will highlight some methods developed by Mitchell et. al. for extracting coherent structures in time-independent [34, 42] and time dependent [36] reacting flows.

1.2.1 Steady Flows-Burning Invariant Manifolds

To model ARD systems, instead of tracking the entire burned region we consider the reaction front only. This method is more computationally efficient and, we believe, more theoretically insightful. To simplify the problem, we assume the following, first the reaction time-scale is much smaller than the diffusion time-scale resulting in a sharp front in which the fluid is divided into reacted and unreacted regions, separated by a well-defined boundary—the reaction front. Second, we assume that each front element is not dependent on the local curvature of the front, though it is known that curvature may play an important role in certain systems [44]. Last, we assume that, in the comoving fluid frame, the front propagates with a fixed speed v_0 that is homogenous and isotropic.

Formally, a front is defined as the oriented boundary between reacted and unreacted regions where the local orientation vector $\hat{\mathbf{n}}$ is normal to the reaction front and points *away* from the burned region. The orientation could alternatively be specified by the tangent vector $\hat{\mathbf{g}}$, where $\hat{\mathbf{g}}$ is orthogonal to $\hat{\mathbf{n}}$ and $\hat{\mathbf{n}} \times \hat{\mathbf{g}} = +1$. Using $\mathbf{r}$ to denote the xy-position of a front element and θ as the angle between the positive x-axis and $\hat{\mathbf{g}}$, a front in three-dimensional $xy\theta$-space is a curve $(\mathbf{r}(\lambda), \theta(\lambda))$ that satisfies the *front-compatibility criterion*

$$\frac{\mathrm{d}\mathbf{r}}{\mathrm{d}\lambda} = \hat{\mathbf{g}}(\theta), \tag{1.9}$$

where λ is the Euclidean length parameter measured in xy-space that increases in the $+\hat{\mathbf{g}}$ direction.

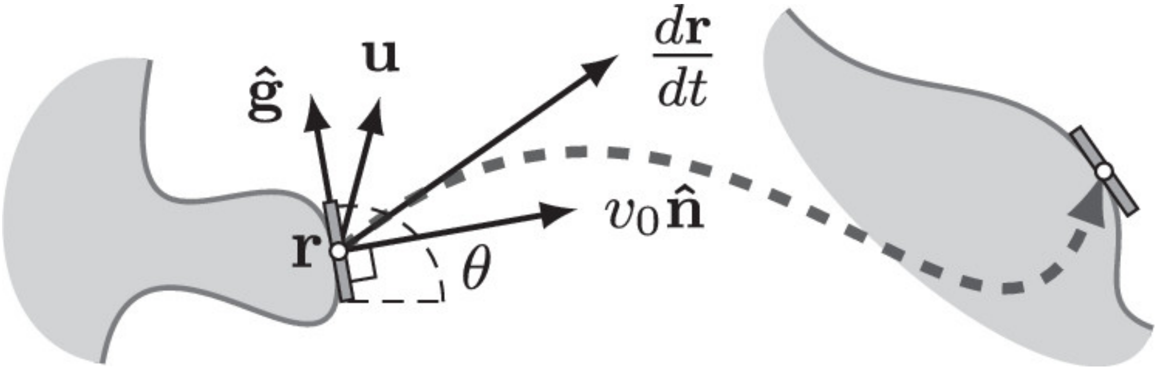

Figure 1.4. A front is defined as the oriented boundary between reacted and unreacted regions where the local orientation vector $\hat{\mathbf{n}}$ is normal to the reaction front and points *away* from the burned region. If $\mathbf{r}$ is used to denote the xy-position of a front element and θ as the angle between the positive x-axis and $\hat{\mathbf{g}}$, each front element, specified by $(\mathbf{r}(t), \theta(t))$, evolves via eq. (1.10)

Each individual front element evolves via

$$\dot{\mathbf{r}} = \mathbf{u} + v_0\hat{\mathbf{n}}, \tag{1.10a}$$

$$\dot{\theta} = -\sum_{i,j} \hat{n}_i u_{i,j} \hat{g}_j, \tag{1.10b}$$

where $\mathbf{u}$ is the incompressible fluid velocity and $u_{i,j} = \partial u_i/\partial r_j$. Therefore a reaction front is translated by the vector sum of the fluid velocity and the burning velocity, Eq. (1.10a). The change in orientation is entirely kinematic and determined by the local behavior of the fluid flow, Eq. (1.10b).

Active enhancement of fluid flows has several interesting consequences. First, new fixed points in the fluid flow can be found where the front propagation exactly counters the fluid flow. These are fixed points of Eq. (1.10) which we call *burning* fixed points. The stable-stable-unstable (SSU) burning fixed points have one unstable manifold which we call the *burning* invariant manifolds (BIMs). It has been shown that BIMs serve as *one-way* barriers to front propagation [34, 42]. The bounding behavior of BIMs is due to the "no-passing" lemma: no front can overtake another front from behind. Fronts oriented in the same direction as the BIM will be unable to directly pass through the BIM, while fronts oriented opposite the BIM will pass through unobstructed. Any arbitrary front (within some moderate basin of attraction) will ultimately converge to the BIMs. Therefore BIMs are important for understanding the evolution and long-time behavior of ARD systems.

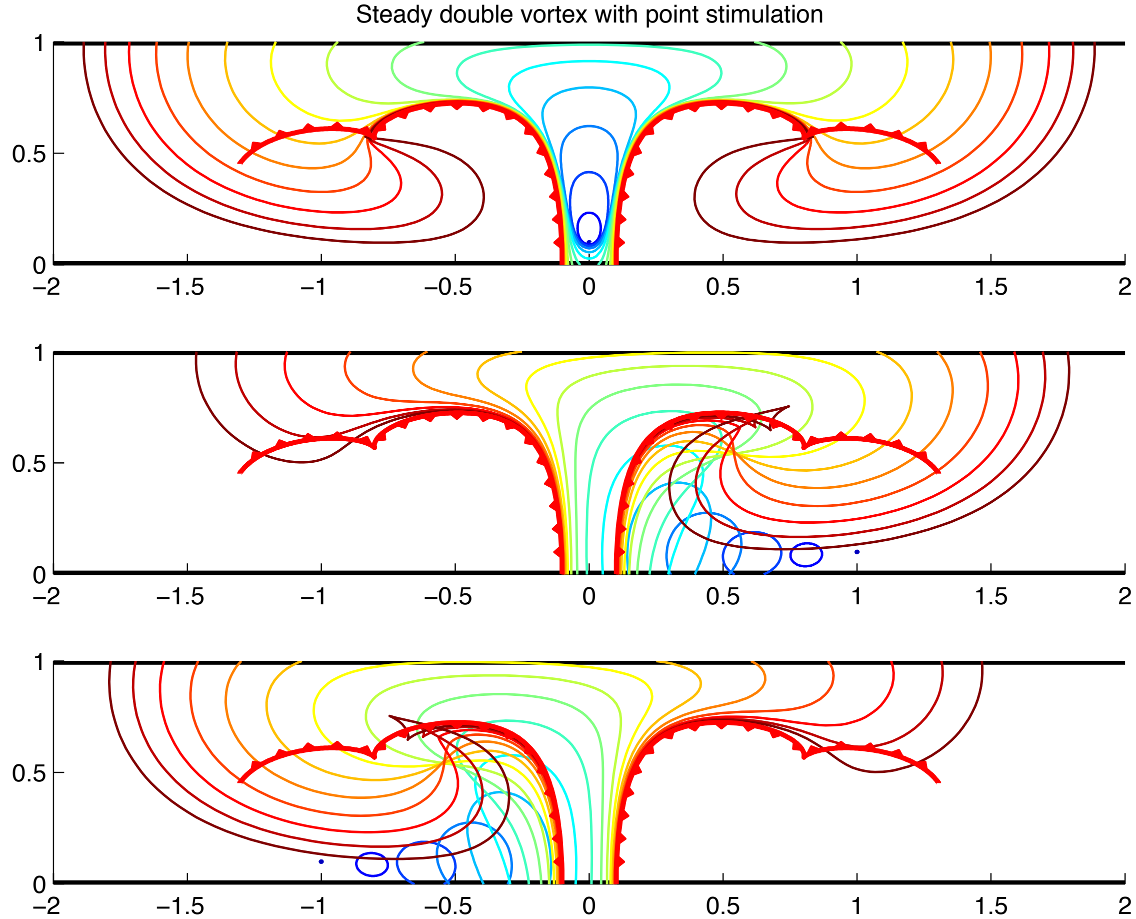

Figure 1.5. Numerical simulation of steady double gyre with an active enhancement. Initial reaction stimulation shown in blue and subsequent samples shown as from blue to red as time moves forward under the flow. The separatrix in the purely advective case has split into two *burning* fixed points with one burning to the left and the other to the right. The unstable *burning* invariant manifolds are shown in red with their burning direction noted by the red arrows. The BIMs are one sided barriers to reaction fronts propagating in the same direction. (a) shows an initial reaction stimulation in between the two BIMs. Here the fronts are confined between the BIMs as the reaction front propagates outward since the front propagation direction is the same as the burning direction for each BIM. (b) shows an initial reaction stimulation on the right side. As the front propagates it is able to pass through the first BIM since its burning direction is opposite to the direction the front is propagating. The front however is blocked by the second, leftmost, BIM since its burning direction is the same as the front propagation direction. (c) shows an initial reaction stimulation on the left hand side, the blocking (non-blocking) nature of the BIMs follows the same reasoning as (b).

Another property of BIMs that is unlike their advective invariant manifold counterparts is that BIMs can form cusps and self-intersections when projected onto the *xy*-plane. (In the full *xy*θ-phase space, BIMs do not self-intersect due to the uniqueness of solutions to ODEs.) In time-independent flows, a cusp marks the end of the physically relevant bounding behavior of the BIM. Fig 1.5 shows a numerical simulation of steady double gyre with an active enhancement. The initial reaction stimulation is shown in blue and the evolution of reaction is from blue to red as the front grows and propagates under the flow. The separatrix in the purely advective case has split into two *burning* fixed points with one burning to the left and the other to the right. The unstable *burning* invariant manifolds are shown in red with their burning direction noted by the red arrows. The BIMs are one sided barriers to reaction fronts propagating in the same direction. Fig 1.5(a) shows an initial reaction stimulation in between the two BIMs. Here the fronts are confined between the BIMs as the reaction front propagates outward since the front propagation direction is the same as the burning direction for each BIM. Fig 1.5(b) shows an initial reaction stimulation on the right side. As the front propagates it is able to pass through the first BIM since its burning direction is opposite to the direction the front is propagating. The front however is blocked by the second, leftmost, BIM since its burning direction is the same as the front propagation direction. Fig 1.5(c) shows an initial reaction stimulation on the left hand side, the blocking (non-blocking) nature of the BIMs follows the same reasoning as (b).

For time-periodic flows, the bounding behavior of BIMs is more subtle. These BIMs can stretch and fold in time (with plenty of cusps and self-intersections) allowing the reaction front to propagate down the channel via a turnstile-like mechanism [33, 37] . In spite of the apparent loss of bounding behavior (in the lab frame), time-periodic driving yields a new form of stable structure in a moving frame—mode-locked fronts. A specific type of mode-locking is specified by two integers N and M and is defined as the recurrence of a pattern which has shifted by N vortex pairs after having evolved under M forcing periods. Figure 1.6a shows snapshots of a front propagating down the channel from left to right, beginning with a vertical front that spans the channel. Each snapshot is taken after one driving period. We see that the front converges almost instantaneously (essentially after the first iterate) to a mode-locked front: the front profile repeats after $M = 1$ driving period and is translated to the right by $N = 1$ vortex pair, demonstrating type (1,1) mode-locking. Similarly,

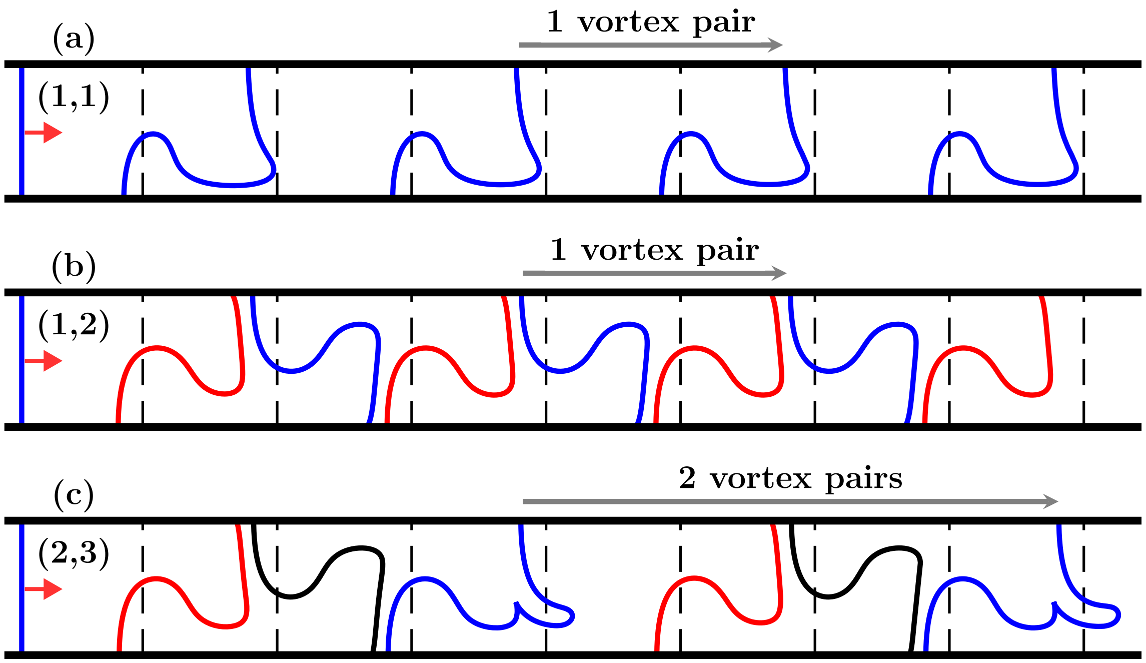

Figure 1.6. Numerically generated reaction front showing evidence of mode-locking. The front propagates down the channel from left to right starting with a vertical front spanning the channel. After one period the front has fully converged. Fig. 1.6 (a)-(c) shows mode-locking of types (1,1), (1,2), and (2,3) with v_0 = 0.18, 0.068, and 0.089 respectively. Dashed vertical lines indicate the vortex cells.

in Fig. 1.6b the front profile repeats after $M = 2$ driving periods, translated by $N = 1$ vortex pair for type (1,2) mode-locking. Finally, Fig. 1.6c shows type (2,3) mode-locking. The phenomenon of mode-locking and how it can be understood in terms of BIMs is discussed in Chapter 2.

1.2.2 Unsteady Flows-Burning Lagrangian Coherent Structures

Once the fluid flow is no longer time independent, the BIM analysis fails in the same way invariant manifold techniques fail in the purely advective case when the underlying fluid flow has some arbitrary time dependence. Thus for active flows with arbitrary time dependence, a new model must be used to capture coherent structures or fronts. Building off the success of Hallar's variational technique, a new model for extracting fronts in time dependent flows has been proposed. This new technique termed *burning* Lagrangian coherent structures (bLCSs) was formulated by Mitchell et al. [36] and is summarized as follows.

To find the bLCSs, first we assume that the fluid velocity $\mathbf{u}(\mathbf{r}, t)$ is defined between an initial time, t_0, and a later time $t_1 = t_0 + T$. There is no requirement that the flow be either

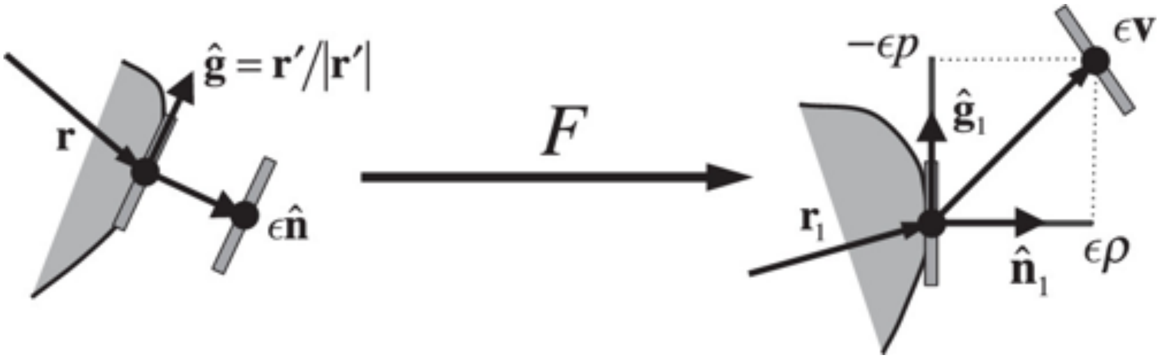
r
$\hat{\mathbf{g}} = \mathbf{r}'/|\mathbf{r}'|$
$\epsilon\hat{\mathbf{n}}$
F
$-\epsilon p$
$\epsilon\mathbf{v}$
$\hat{\mathbf{g}}_1$
$\mathbf{r}_1$
$\hat{\mathbf{n}}_1$
$\epsilon\rho$

Figure 1.7. Given an initial front, a small normal displacement of a front element, $\epsilon\hat{n}$, evolves under F to a vector $\epsilon\mathbf{v}$. This new evolved front element will in general have a nonzero tangential component. We define the Lagrangian shear p over time interval t to be the projection of $\epsilon\mathbf{v}$ in the tangent direction divided by ϵ. Similarly we define the normal repulsion ρ to be the projection of $\epsilon\mathbf{v}$ in the normal direction divided by ϵ.

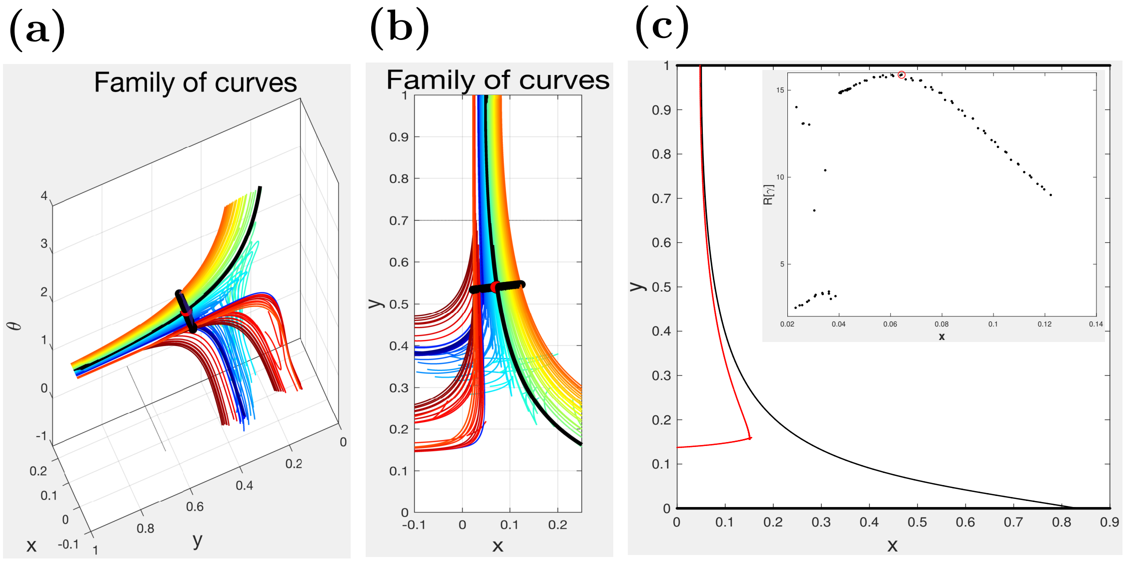

Figure 1.8. (a) Family of sheerless curves in $xy\theta$-space. Black line shows line of initial conditions and black curve shows the BIM. (b) Two dimensional projection of the family of sheerless curves in xy-space. (c) Comparison of the BIM (black) and the sheerless curve chosen as the bLCS (red), Inset shows the average normal repulsion curve as a function of the initial conditions x coordinate with the bLCS circled in red.

time-independent or time-periodic over interval $[t_0, t_1]$. The trajectory of a front element over this time interval is obtained by solving Eq. 1.10. The flow map that takes an initial point in (r, θ)-space to a final point after solving Eq. 1.10 is defined to be $F = F_{t_0}^{t}$. Lagrangian shear and normal repulsion are defined as follows (see Fig. 1.7) Given an initial front, a small normal displacement of a front element, $\epsilon \hat{n}$, evolves under F to a vector $\epsilon \mathbf{v}$. This new evolved vector will in general have a nonzero tangential component. We define the Lagrangian shear p over time interval t to be the projection of $\epsilon \mathbf{v}$ in the tangent direction divided by ϵ. Similarly we define the normal repulsion ρ to be the projection of $\epsilon \mathbf{v}$ in the normal direction divided by ϵ. Thus we can write,

$$p(\mathbf{r}, \theta) = \langle -\hat{g}_1, \mathbf{v} \rangle = -\langle \hat{g}(F(\mathbf{r}, \theta)), [\nabla F]_{xy} \hat{n} \rangle \tag{1.11a}$$

$$\rho(\mathbf{r}, \theta) = \langle \hat{n}_1, \mathbf{v} \rangle = \langle \hat{n}(F(\mathbf{r}, \theta)), [\nabla F]_{xy} \hat{n} \rangle \tag{1.11b}$$

where $[\nabla F]_{xy}$ is the 2x2 projection of the flow map gradient given by,

$$[\nabla F]_{xy} = \Pi_{xy} \nabla F \Pi_{xy}^{T}, \tag{1.12}$$

with

$$\Pi_{xy} = \begin{pmatrix} 1 & 0 & 0 \\ 0 & 1 & 0 \end{pmatrix}. \tag{1.13}$$

With the definitions of Lagrangian shear and normal repulsion we can look to the variational problem. Following Hallar et al. we seek to find a curve parameterized by γ, the Euclidean distance, that makes the average Lagrangian shear stationary under infinitesimal variations. (Eq. 1.14)

$$\overline{P}_0[\gamma] = \frac{1}{T} \int_0^T p(\mathbf{r}, \theta) d\tau, \tag{1.14}$$

We define these curves as perfect shearless fronts or shearless fronts for short. We find shearless fronts utilizing a constraint surface or shearless surface (Eq. 1.15)

$$p(\mathbf{r}, \theta) = 0. \tag{1.15}$$

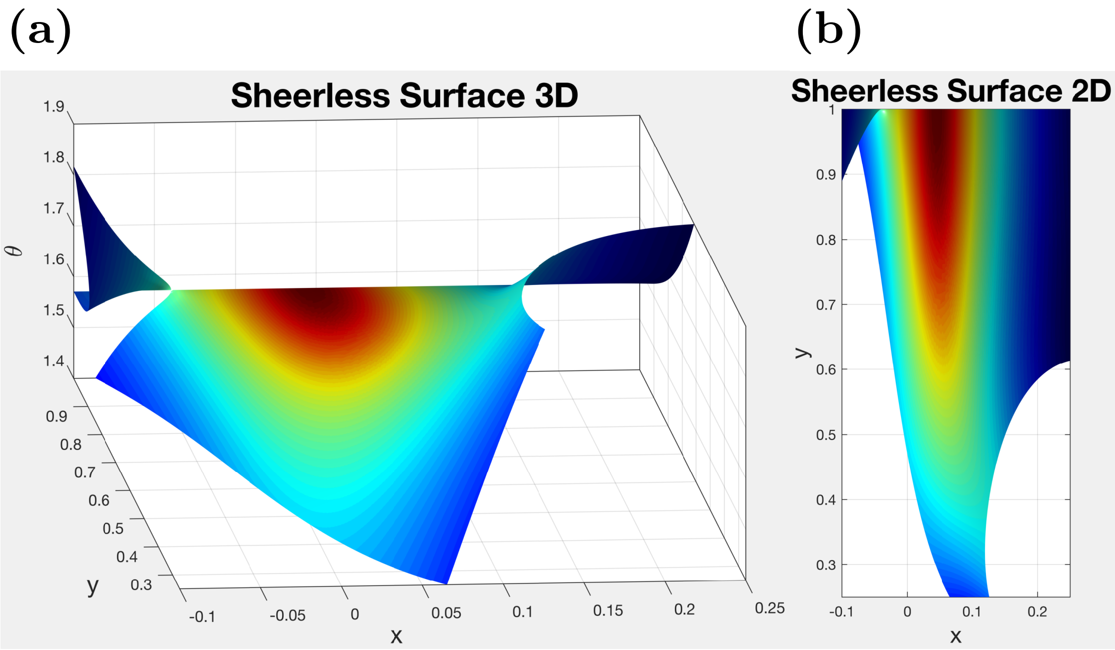

Figure 1.9. (a) Sheerless surface in $xy\theta$-space. (b) Two dimensional projection of the sheerless surface in xy-space. The coloring corresponds to the value of the normal repulsion, red being a positive value and blue denoting a negative value.

Figure 1.9 shows an example of a shearless surface in the full $xy\theta$-space (a), and a two dimensional projection in (b). A perfect shearless front once lifted by Eq. 1.9 must lie within the shearless surface. Thus a perfect shearless front is the integral curve of a vector field tangent to Eq. 1.15. The normalized tangent vector field is given by

$$\frac{d\mathbf{r}}{d\lambda} = \frac{a}{\sqrt{a^2+b^2}}\hat{g}, \tag{1.16a}$$

$$\frac{d\theta}{d\lambda} = \frac{b}{\sqrt{a^2+b^2}}, \tag{1.16b}$$

where

$$a = -\frac{d}{d\theta}p, \tag{1.17a}$$

$$b = \hat{g}\cdot\nabla p. \tag{1.17b}$$

We will also need the vector field that is everywhere orthogonal but still tangent to the shearless surface. This field is obtained by replacing $\hat{g}$ with $\hat{n}$ in Eqs. 1.16 and 1.17, i.e.,

$$\frac{d\mathbf{r}}{d\kappa} = \frac{a}{\sqrt{a^2+c^2}}\hat{n}, \tag{1.18a}$$

$$\frac{d\theta}{d\kappa} = \frac{c}{\sqrt{a^2+c^2}}, \tag{1.18b}$$

where

$$c = \hat{n}\cdot\nabla p. \tag{1.19}$$

Once we have reduced the problem to a 2D surface we select the the best shearless curve as that curve which maximizes the average normal repulsion.

$$R[\gamma] = \frac{1}{L}\int_{\gamma}(\sqrt{\hat{n}\cdot C(\mathbf{r},\theta)}dl, \tag{1.20}$$

where C is the *projected* right Cauchy-Green tensor given by,

$$C(\mathbf{r},\theta) = [\nabla F]_{xy}^{T}[\nabla F]_{xy}. \tag{1.21}$$

In chapter 3 we will apply the bLCS model to a linear time varying wind and a stochastic wind to extract the bLCS(s).

1.3 Summary of Manuscript

This manuscript is organized as follows. In Chapter 2 we apply the *burning invariant manifold* (BIM) model to that of a time-periodic fluid flow in an oscillating chain of vortices. If the vortex chain oscillates periodically in the lateral direction, the reaction front often mode-locks to the oscillations, propagating an integer number of wavelengths of the flow (two vortices) in an integer number of drive periods. We show how this phenomenon can be explained in terms of relative periodic *burning* fixed points or relative periodic orbits (RPOs) and show numerical simulations that justify this theory. We establish concretely the connection to the mode-locked fronts and the BIMs. Finally we discuss the bifurcations in mode-locking type as a function of front propagation speed and how global bifurcations can create or destroy mode-locking. In Chapter 3 we apply the *buring* Lagrangian Coherent structures (bLCSs) model to that of a time-varying wind. First we show numerical simulations of the bLCS applied to a linear time varying wind. Next we move to a more realistic case and show numerical simulations of the bLCS applied to a stochastic wind. We discuss the bounding nature of bLCS(s) and compare that to the BIMs in steady flows. In Chapter 4 we apply the bLCS model to experimental data of a single vortex in a windy channel and compare our results with those found experimentally. Chapter 5 summarizes the finding throughout this manuscript and discusses future work. Chapter 6 discusses how we numerically compute the relative periodic orbits and our method of finding seeds for newtons method. Also we show different techniques for extracting bLCS(s) and where computational difficulties may arise.

Chapter 2

Time Periodic barriers and Mode-locking

2.1 Introduction

Many physical systems can be characterized by the propagation of a front. These systems range from plasmas [9], plankton blooms [54], the spread of disease, and chemical reactions [60]. The case in which no flow exists, the reaction-diffusion limit, is well characterized by the theory of Fisher and Kolmogorov-Petrovskii-Piskunov (FKPP) [31]. The front velocity v_0, predicted by FKPP is given by:

$$v_0 = 2\sqrt{\frac{D_0}{\tau}}, \tag{2.1}$$

where D_0 is the molecular diffusivity and τ the reaction time-scale.

However, analysis of fronts in flowing media have proved more challenging. In order to predict the front speed in a reacting fluid with flow, an attempt was made to modify FKPP theory by introducing an enhanced diffusivity, D^* [45]. This proved to be accurate only in the limit of a very slow reaction. Specifically, the enhanced diffusivity theory does not predict mode-locking in the periodically driven alternating vortex flow. A specific type of mode-locking is specified by two integers N and M. (N, M) *mode-locking* is the recurrence of a pattern which has shifted by N vortex pairs after having evolved under M forcing periods. It is straightforward to see that

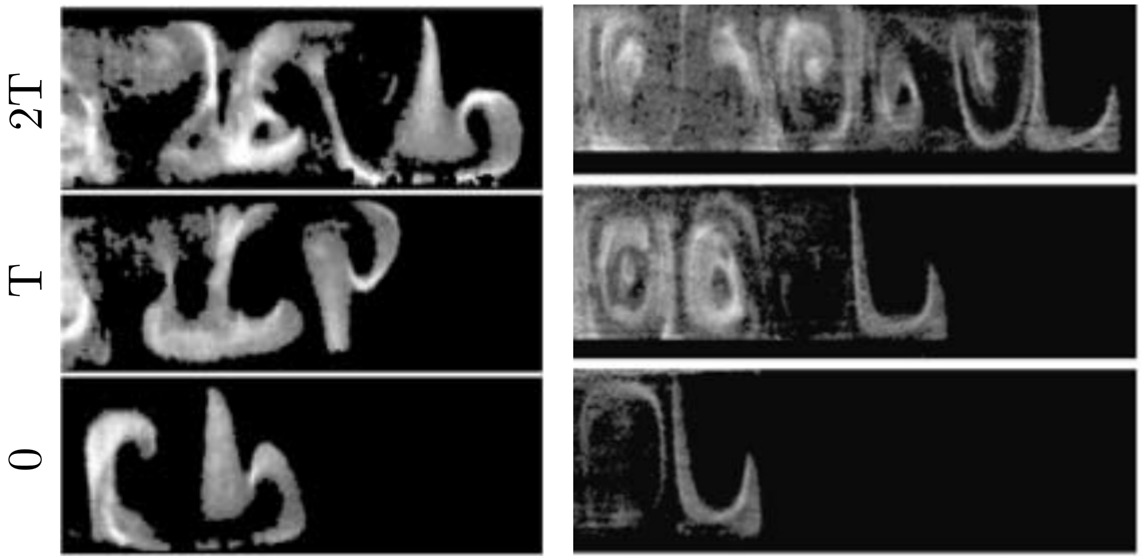

Figure 2.1. Experimental images of the Belousov-Zhabotinsky reaction in a quasi-two-dimensional alternating vortex channel flow. The flow is driven by an electric current passing through the fluid over a row of magnets. Left: Experimental image of mode-locking type (1,2). It takes two driving periods for the “b”-shaped front profile to repeat itself shifted by one pair of vortices. Right: Experimental image of mode-locking type (1,1) [48].

the average front velocity in the lab frame v_f is related to the type of mode-locking through the following relation [14]:

$$v_f = \frac{N\lambda}{MT}, \tag{2.2}$$

where λ is the width of a pair of vortices and T the period of oscillation.

Cencini et. al model ARD systems numerically using the so-called *G*-equation in a grid-based approach [2, 14, 50]. These methods do predict mode-locking, but are computationally costly [14]. Several experiments have also clearly demonstrated the existence (and robustness) of mode-locking in ARD systems [47, 48]. Figure 2.1 shows such an experimental realization using the excitable Belousov-Zhabotinsky reaction in a chain of alternating vortices.

Recently, it has been demonstrated that two-dimensional ARD flows with sharp reaction fronts can be reduced to a three-dimensional ODE for front-element dynamics [34, 42]. This approach reveals that reaction-front propagation is dominated by the presence of *burning invariant manifolds* (BIMs), invariant manifolds of the front-element dynamics. (We use the term “burning” as shorthand for any reaction front propagation differentiating them from their advective counterparts.) Unlike traditional invariant manifolds, these BIMs act as *one-way* barriers to reaction front propagation. In this article, we show how BIMs underly the phenomenon of mode locking. We explain how a BIM attached to a relative periodic orbit (RPO) of the front element dynamics can result in mode-locking and show numerical simulations. Finally we discuss how changes in the type, as well as the loss, of mode locking can be understood in terms of local and global bifurcations of the RPOs and their BIMs.

This paper is organized as follows. Section 3.2.1 introduces the three-dimensional dynamical system for a point along the front. Section 3.2.2 reviews the theory of burning invariant manifolds. Section 3.3.1 justifies the abstract theory with concrete numerical realizations of this connection in a model flow. Section 3.3.2 presents the central result of this paper, establishing the fundamental connection between mode-locking and BIMs. Finally, Section 4.3.1discusses bifurcations in mode-locking type as a function of the front propagation speed and how global bifurcations can create or destroy mode locking of a given type . Our numerical technique for locating RPOs is discussed in the appendix.

2.2 Preliminaries

2.2.1 Front-element dynamics

We model ARD systems by considering only the reaction front. This is more computationally efficient than explicitly modeling the entire fluid state and, we believe, more theoretically insightful. We make use of the following assumptions. First, the reaction time-scale is much smaller than the diffusion time-scale—this is known as the “sharp front” or geometric-optics limit [1, 2]. In this limit, the fluid is divided into reacted and unreacted regions that are separated by a well-defined boundary—the reaction front. Second, we assume that each front element progresses in a manner independent of the local curvature of the front. It is known that this curvature plays an important role in certain systems [44]. Last, we assume that, in the comoving fluid frame, the front propagates with a fixed speed v_0 that is homogenous and isotropic.

More technically, a front is defined as the oriented boundary between reacted and unreacted regions where the local orientation vector $\hat{\mathbf{n}}$ is normal to the reaction front and points *away* from the burned region. The orientation might also be specified by the tangent vector $\hat{\mathbf{g}}$, where $\hat{\mathbf{g}}$ is orthogonal to $\hat{\mathbf{n}}$ and $\hat{\mathbf{n}} \times \hat{\mathbf{g}} = +1$. If $\mathbf{r}$ is used to denote the xy-position of a front element and θ as the angle between the positive x-axis and $\hat{\mathbf{g}}$, a front in three-dimensional $xy\theta$-space is a curve $(\mathbf{r}(\lambda), \theta(\lambda))$ that satisfies the *front-compatibility criterion*

$$\frac{\mathrm{d}\mathbf{r}}{\mathrm{d}\lambda} = \hat{\mathbf{g}}(\theta), \tag{2.3}$$

where λ is the Euclidean length parameter measured in xy-space that increases in the $+\hat{\mathbf{g}}$ direction.

Each front element, specified by $(\mathbf{r}(t), \theta(t))$, evolves via

$$\dot{\mathbf{r}} = \mathbf{u} + v_0\hat{\mathbf{n}}, \tag{2.4a}$$

$$\dot{\theta} = -\sum_{i,j} \hat{n}_i u_{i,j} \hat{g}_j, \tag{2.4b}$$

where $\mathbf{u}$ is the incompressible fluid velocity and $u_{i,j} = \partial u_i/\partial r_j$. Each fluid element is translated by the vector sum of the fluid velocity and the burning velocity, Eq. (2.4a). Furthermore, the change in orientation is determined solely by the local behavior of the fluid flow, Eq. (2.4b). Numerically, a front is composed of a line of discrete fluid elements that propagate independently under this three-dimensional ODE. To maintain a sufficiently smooth front in spite of the stretching of the fluid flow, we dynamically insert new points by interpolation.

As it evolves, portions of the front may come to lie within the burned region. Figure 2.2 shows how an initially circular front (a) grows into a non-circular front (b), develops a swallowtail (c), and encounters the channel boundary (d). The swallowtail portion of the front lies within the burned region and therefore no longer represents a physical boundary. While we refer to the entire evolved curve (either in xy-space or $xy\theta$-space) as the front, we refer to those segments of the front separating the burned from unburned regions as the *bounding front*. The bounding front can exhibit corners where the bounding front is not differentiable in xy-space (i.e., it is disconnected in $xy\theta$-space).

2.2.2 Burning invariant manifolds (BIMs) and frozen fronts

The theory of invariant manifolds in passive advection is well established. In the two-dimensional setting, time-independent flows lead to separatrices—invariant manifolds that

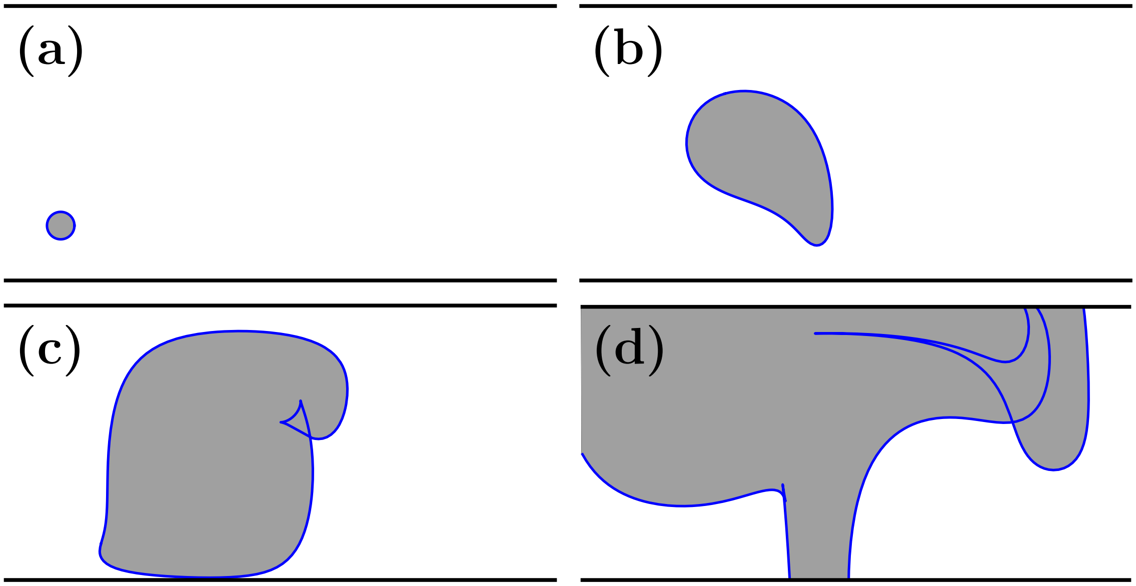

Figure 2.2. (a) An initial circular burned region at $t = 0T$. Panels (b)-(d) show the forward evolution at times $t = 0.3T, 0.6T$, and $1.19T$ respectively. The front is evolved using Eq. (2.4) with v_0= 0.2 and $\mathbf{u}$ given by Eq. (3.3), with $b = 0.25$, and $\omega = 2$.

connect various fixed points and divide the fluid into "cells". Under a time-periodic perturbation, these separatrices split giving rise to distinct stable and unstable manifolds. These more complicated objects describe the mechanism of transport between cells.

The addition of propagation dynamics has several interesting consequences. First, we find fixed points of Eq. (2.4) where the front propagation exactly counters the fluid flow. We refer to these as *burning* fixed points. Of primary interest are the stable-stable-unstable (SSU) burning fixed points. Attached to these are the so-called *burning* invariant manifolds (BIMs). Here we focus on the 1D unstable BIMs attached to SSU burning fixed points. It has been shown that BIMs serve as *one-way* barriers to front propagation [34, 42]. The bounding behavior of BIMs is due to the "no-passing" lemma: no front can overtake another front from behind. Thus, fronts oriented in the same direction as the BIM will be unable to directly pass through. Conversely, fronts oriented opposite the BIM will pass through unobstructed. Also, arbitrary fronts (within some moderate basin of attraction) converge to the BIMs. Because of these facts, SSU BIMs are important for understanding the evolution and long-time behavior of ARD systems.

Another new property of BIMs is a phenomenon more familiar in optics: BIMs can form cusps and self-intersections when projected onto the *xy*-plane as shown in Fig. 2.2(c). (In the full $xy\theta$-phase space, BIMs do not self-intersect due to the uniqueness of solutions to ODEs.) In time-independent flows, a cusp marks the end of the physically relevant bounding behavior of the BIM.

Finally, as first observed experimentally just over a decade ago, reaction fronts in steady ARD flows exhibit the tendency to pin to vortex structures in the presence of an imposed “wind” [35,39]. A front initiated upwind of a pinning site can travel downstream, catch the site, and eventually reach a steady state. This “frozen front” phenomenon has been explained in terms of BIMs. Qualitatively, a *frozen front* occurs when a BIM spans the entire channel without a cusp, or when a set of BIMs do so collectively. These results can be made precise using the concept of a BIM core; the BIM core is defined as the BIM segment that includes the burning fixed point and extends in both directions until reaching either a cusp, a new burning fixed point, or infinity.

Frozen fronts in steady flows are built from BIM cores. More precisely, each frozen front is generated by a set of SSU burning fixed points. The frozen front is obtained by tracing the unstable manifold from each point in the set of fixed points until one of three things occurs: it intersects any other BIM core emanating from this set; it intersects any domain boundary; or it terminates at an SSS burning fixed point [35].

For time-periodic flows, the bounding behavior of BIMs is more subtle. These BIMs can stretch and fold in time (with plenty of cusps and self-intersections) allowing the reaction front to propagate down the channel via a turnstile-like mechanism [33,37] . In spite of the apparent loss of bounding behavior (in the lab frame), time-periodic driving yields a new form of stable structure in a moving frame—mode-locked fronts.

2.3 Mode-Locking

2.3.1 Numerical Simulations

As a concrete example we choose the well-studied alternating vortex chain [14,15,56]. This flow mimics a two-dimensional cross-section of Rayleigh-Benard convection in which roll patterns, i.e. vortices, appear due to an instability driven by heating of the lower boundary. The two-dimensional

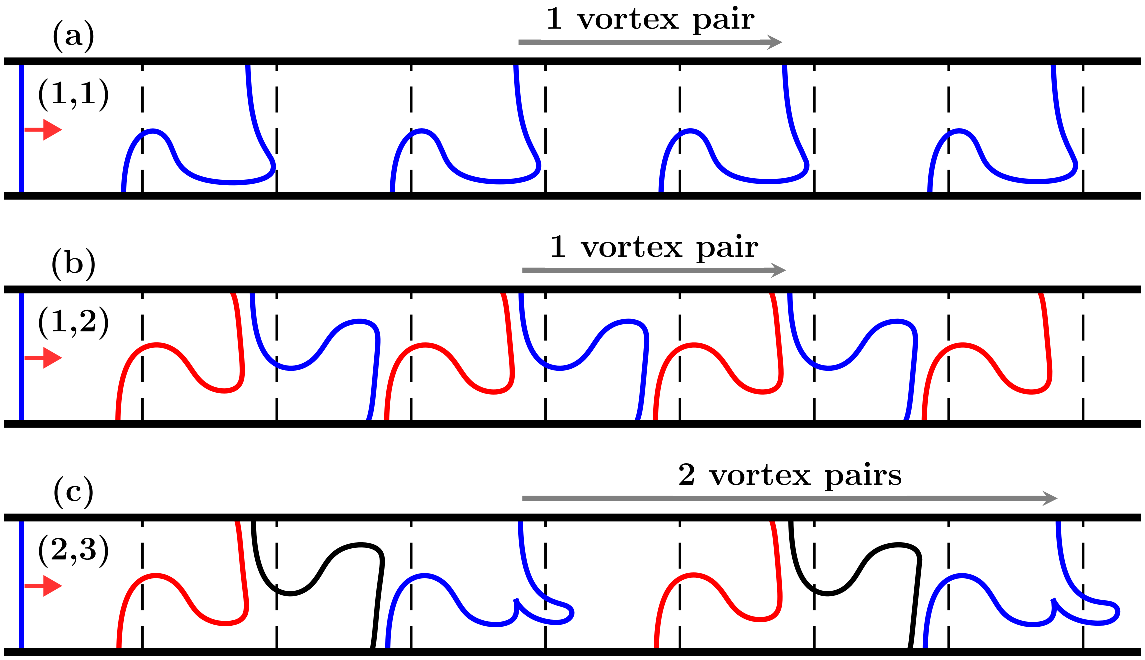

Figure 2.3. Numerically generated reaction front showing evidence of mode-locking. The front propagates down the channel from left to right starting with a vertical front spanning the channel. After one period the front has fully converged. Fig. 2.3 (a)-(c) shows mode-locking of types (1,1), (1,2), and (2,3) with v_0 = 0.18, 0.068, and 0.089 respectively. Dashed vertical lines indicate the vortex cells.

velocity field is given by

$$u_x(x,y,t) = +\sin(\pi[x + b\sin(\omega t)])\cos(\pi y), \tag{2.5a}$$

$$u_y(x,y,t) = -\cos(\pi[x + b\sin(\omega t)])\sin(\pi y), \tag{2.5b}$$

where $0 \leq y \leq 1$ and time-dependence is produced by the lateral oscillation term $x + b\sin(\omega t)$. Note that this model assumes free-slip boundary conditions. The dimentionfull parameters of the system are U,D, Ω, B and V_0 which correspond to the maximum fluid speed, channel width, driving frequency, driving amplitude, and the front propagation speed in the absence of a flow, respectively. The dimensionless parameters of the system are $b = B/D$, $\omega = \Omega D/U$, and $v_0 = V_0/U$. The position vector **r** is scaled such that the maximum fluid vortex speed, U, is one and the width of each vortex is one. For these simulations we fix $b = 0.3$, $\omega = 4.08$ and vary the front velocity v_0. Numerical simulations were performed by propagating individual front elements under Eq. (2.4). By varying parameters, we identified mode-locking of types: (1,1), (1,2), (2,3) and (3,5).

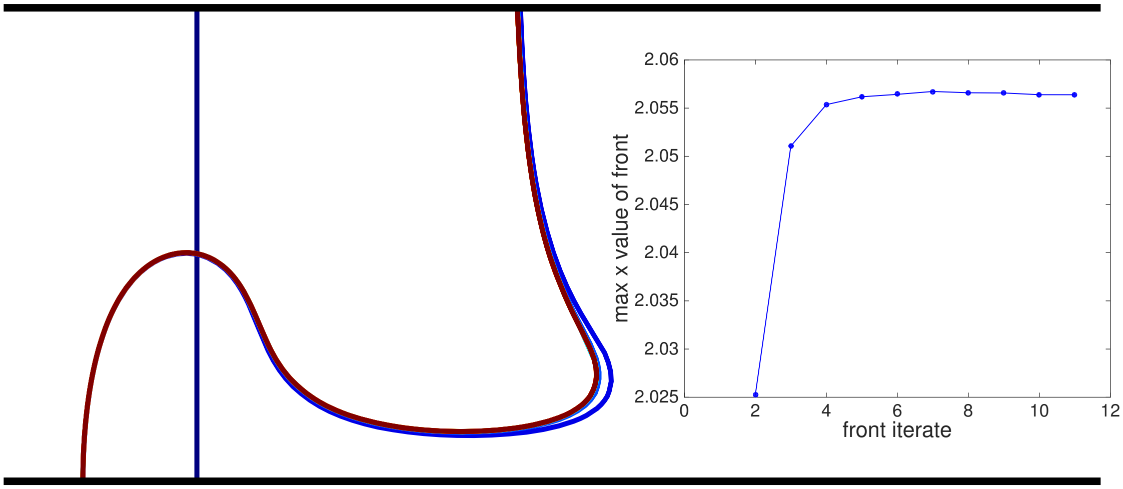

Figure 2.4. Simulation demonstrating convergence of fronts to mode locking. (1,1) mode-locking with fronts shifted backwards showing convergence to be approximately one period. The initial condition is shown as the straight vertical line. The inset shows the rightmost point of the front as a function of the number of iterates. Beginning with the initial front we see it takes no more than two iterates to reach the mode-locked state.

Figure 2.3a shows snapshots of a front propagating down the channel from left to right, beginning with a vertical front that spans the channel. Each snapshot is taken after one driving period. We see that the front converges almost instantaneously (essentially after the first iterate) to a mode-locked front: the front profile repeats after $M = 1$ driving period and is translated to the right by $N = 1$ vortex pair, demonstrating type (1,1) mode-locking. Similarly, in Fig. 2.3b the front profile repeats after $M = 2$ driving periods, translated by $N = 1$ vortex pair for type (1,2) mode-locking. Finally, Fig. 2.3c shows type (2,3) mode-locking.

The convergence of the initial vertical front to the mode-locked profile is very rapid. Figure 2.4 shows the initial condition as the vertical line. Each of the subsequent fronts in Fig. 2.4 is shifted backward by an integer number of vortex pairs, so that the fronts all lie within the original cell. Except for the initial vertical line, these shifted fronts are visually nearly identical, demonstrating that a single iterate is essentially all that is needed to reach the mode-locked state.

After a front has converged to the mode-locked profile, Fig. 2.5 shows several equally spaced intermediate time steps of its evolution over one mode-locked period for the (1,1) mode-locking case. The black curve on the left maps to the black curve on the right one mode locked period later. The intermediate curves are snapshots of how a front evolves over one period. Note that

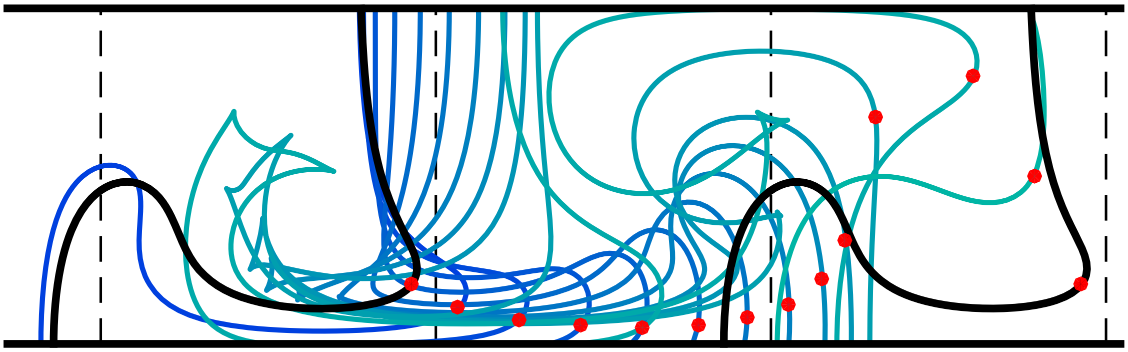

Figure 2.5. Reaction front shows evidence of (1,1) mode locking with $v_0 = 0.18$. The front evolves from left to right down the channel beginning with a fully converged front, black curve on the left, and then evolving forward over one period where the shape of the front repeats itself one period later, black curve on the right.

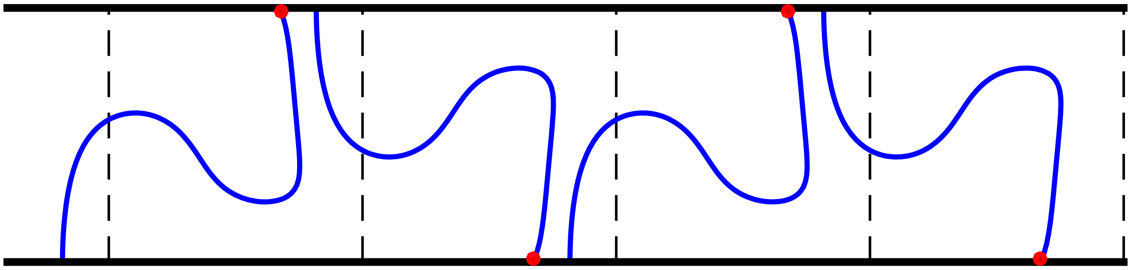

Figure 2.6. Simulation of (1,2) mode-locked front propagating down the channel for two periods.

the propagation of the front down the channel is not strictly monotonic. As Fig. 2.5 shows some intermediate steps are closer together and some farther apart. Also it is interesting to see the formation and loss of swallowtails in between periods as the front evolves. Lastly we could chose any intermediate front and map it forward one period and that shape would repeat, there is nothing special about the shape of the front in respect to mode-locking.

Figure 2.6 and Figure 2.7 show mode-locked fronts of type (1,2) and (3,5) respectively. These images show that the BIM model can also accurately capture higher order, i.e. period, mode-locking similar to the grid based approach used by Cencini et. al. "Finding" higher order mode-locking presents some interesting numerical challenges however, we developed a robust approach that will

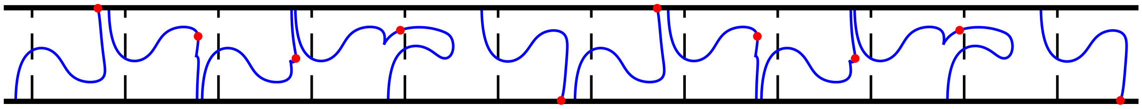

Figure 2.7. Simulation of (3,5) mode-locked front propagating down the channel for nine periods.

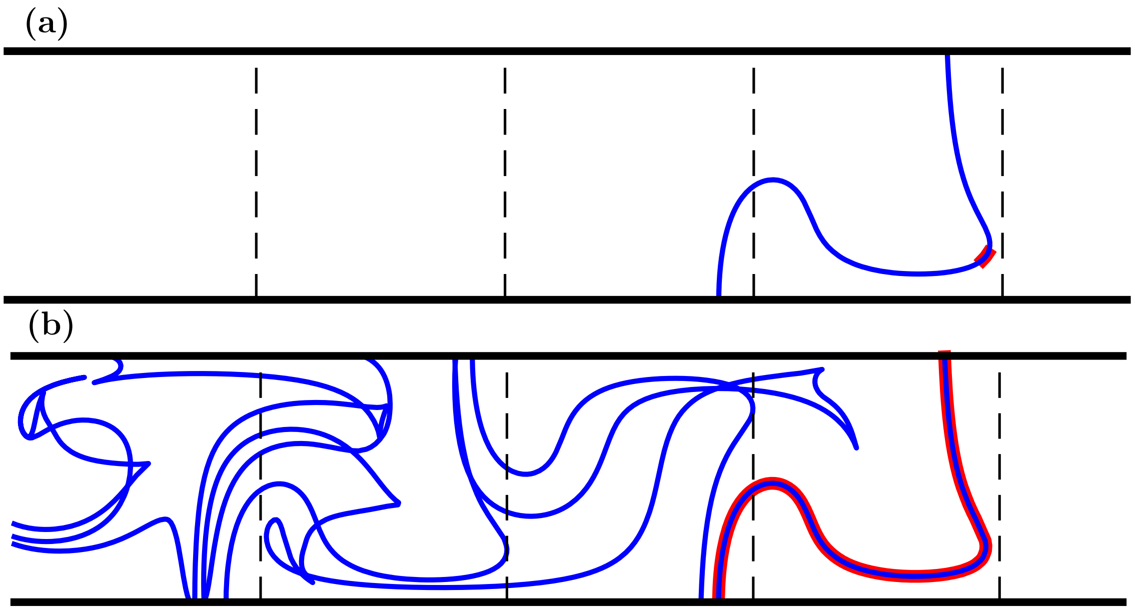

Figure 2.8. Simulation of (1,1) mode-locking demonstrates the extreme stretching experienced by the bounding front under the map $F^{(1,1)}$. Blue bounding front (a) maps to blue front (b). Small red segment (a) maps to red bounding front (b).

be covered in detail in the appendix.

2.3.2 Mode-locked fronts are composed of BIMs

In this section, we derive our main mathematical result, Proposition 2.3.2, a structural characterization of mode-locked fronts. We first introduce some notation. The stroboscopic map F evolves an initial point (x, y, θ) forward via Eq. (2.4) for one forcing period T. The shift map S translates a point forward by a single vortex pair, i.e.

$$S(x, y, \theta) \equiv (x + 2, y, \theta). \tag{2.6}$$

Finally, we define the composite map $F^{(N,M)}$,

$$F^{(N,M)} \equiv S^{-N} \circ F^{M}, \tag{2.7}$$

which simply evolves an initial point forward M forcing cycles and then shifts it backward by N vortex pairs.

By definition, an (N, M) mode-locked front must be invariant under $F^{(N,M)}$ in order to satisfy the original characterization of mode-locking, Definition 2.1. Importantly, the mode-locked front is on the boundary between the burned and unburned regions, i.e. it is the bounding front B of the potentially longer curve that may extend into the burned region. As with frozen fronts in stationary flows, the projection of B into xy-space need not be a single smooth segment, but may have corners where two segments join. Unlike frozen fronts, however, the projection of B may have multiple disconnected pieces. One of these pieces constitutes the *leading front* of the mode-locked front, i.e., the part of the curve that directly contacts the infinite unburned domain. This leading front consists of a finite union of smooth segments connecting the top of the channel to the bottom. The other connected components of the mode-locked front all bound voids that trail the leading front.

Note that in the full phase space, B is a finite union of closed disjoint segments. As B evolves forward in time, these segments will be stretched and folded so that they are ultimately longer than the original B. Thus, B is only invariant in the sense that $F^{(N,M)}(B)$ includes the original B, i.e. $B \subset F^{(N,M)}(B)$. Figure 2.8 shows an example of this behavior, where an initial bounding front B (blue in Fig. 2.8a) evolves forward to the curve $F^{(N,M)}(B)$ (blue in Fig. 2.8b). Because of the extreme stretching, the tiny red segment in Fig. 2.8a grows to cover the entire leading front (red) in Fig. 2.8b.

We next show that for the system to exhibit mode-locking of type (N, M), there must exist a *relative periodic orbit* (RPO) of Eq. (2.4) on the mode-locked front B. A relative periodic orbit is an orbit that is periodic when viewed relative to the comoving reference frame, i.e. the reference frame moving with a uniform velocity equal to the average front velocity v_f [Eq. (2.2)]. More precisely, we define a relative periodic orbit of type (N, M) to be an orbit that is shifted forward N vortex pairs after M driving periods, which can be equivalently stated as follows. An (N, M) relative periodic orbit (RPO) is a fixed point under $F^{(N,M)}$. Much of the structure of the mode-locked front B is revealed by analyzing the inverse map $(F^{(N,M)})^{-1}$, which shrinks B, i.e. $(F^{(N,M)})^{-1}(B) \subset B$. Since B is a collection of segments, $(F^{(N,M)})^{-1}$ restricted to B is topologically equivalent to a differentiable map $f : \cup_i I_i \to \cup_i I_i$ defined over a finite collection of disjoint closed intervals $\{I_i\}$ on the real line. For any such f, there must exist some interval I' that maps into itself after some number of iterates $k \geq 1$, i.e. $f^k(I') \subset I'$. By the Brouwer Fixed Point Theorem [43] (equivalently,

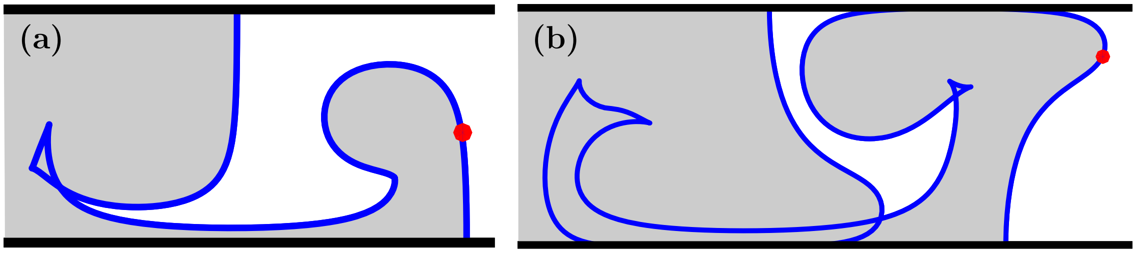

Figure 2.9. (a) Mode-locked front with RPO in red. The front has a swallowtail that extends into the burned region. Here the bounding front is composed of two segments only one of which has the RPO. (b) Mode-locked front with RPO in red, and a void (unburned region) trapped behind the bounding front. If an RPO of another type were present on any segment of the front that encompasses the void it would not persist indefinitely. All the unburned material behind the bounding front will become burned thus it is not possible to have two simultaneous mode-locking types.

the Intermediate Value Theorem in 1D) f^k has a fixed point $x \in I'$. More generally, it is easy to see that f^k will generically have a finite odd number of fixed points in I' that alternate between stable and unstable, i.e. SUSU...US, with at least one stable fixed point. Thus, all points in I' (except the unstable fixed points) will converge to a stable fixed point under f^k. These facts are true for any interval I' that eventually maps into itself under f. For any interval $\tilde{I}$ that doesn't eventually map into itself, $\tilde{I}$ will eventually map into an interval that does, i.e. $f^\ell(\tilde{I}) \subset I'$, and hence all points in $\tilde{I}$ converge to a stable fixed point of f^k. These results for f readily imply the following facts for the mode-locked front B.

(i) A mode-locked front of type (N, M) contains an RPO of type (kN, kM) for some integer $k \geq 1$. This RPO is unstable in the direction tangent to the front. Furthermore, each smooth segment of the mode-locked front either has no RPOs or a finite odd number of RPOs that alternate between unstable and stable in the direction tangent to the front, i.e. USU...SU. Thus, while each smooth segment of a frozen front must contain a BFP (Prop. 2.2.2), it is not necessary for each smooth segment of a mode-locked front to contain an RPO. For example, the mode-locked front in Figure 2.9a has two smooth segments joined at a swallowtail. Only one of these segments contains an RPO.

(ii) Every point on the mode-locked front (except the RPOs that are stable in the tangent direction) is in the unstable manifold of an RPO that is unstable in the tangent direction. Note that the smooth segment in Fig. 2.9a that does not contain an RPO nevertheless lies within the unstable manifold of the RPO.

Result (i) above can be further refined: only the leading front can contain RPOs. This is because each void trailing the leading front can only persist for a finite amount of time, as the void is of finite area and the front consumes unburned fluid at a constant rate per unit length. The unburned fluid inside a void must be repeatedly refreshed by the voids being "pinched off" from the leading front, with the boundaries of the voids thus being on the unstable manifolds of RPOs on the leading front. This is exactly what is seen in Fig. 2.9b. Furthermore, if there are multiple RPOs (of type (kN, kM)) on the leading front, their ordering along the front cannot change under $F^{(N,M)}$; if this were to happen then one RPO would have to pass in front of the other and the trailing RPO would end up in a void or within the burned region. Neither of these is possible. Thus, no RPO can trade places with any other RPO under the map $F^{(N,M)}$, which means that each RPO is a fixed point of $F^{(N,M)}$ so $k = 1$.

We now consider only those mode-locked fronts that are stable to small perturbations, making them physically relevant to the experiments. This stability of the front implies that all RPOs must be stable in the remaining two directions, i.e. the RPOs have stability SSU or SSS in the full phase space.

Thus, the mode-locked front is generated by a finite number of SSU RPOs, where the front continuously grows out of the RPOs as time evolves. Tracking a point on one of these BIMs as a function of time, we find that it ceases to be on the mode-locked front only when it strikes the channel wall or hits another point along the BIM, where it then penetrates the burned region. A point on the mode-locked front can also converge onto an SSS RPO on the front. We summarize with the following proposition analogous to Proposition 2.2.2.

Mode-locked fronts are built from BIMs. More precisely, a physically stable mode-locked front of type (N, M) is generated by a set of SSU RPOs of type (N, M). The mode-locked front is obtained from those points on the BIMs of the RPOs that have never previously struck some other point on the BIMs or struck the channel wall. The BIM segments in the mode-locked front may have endpoints at the wall, at another BIM segment, or at an SSS RPO.

Finally, it is important to note that the RPOs that generate the front must in fact lie on the bounding part of their BIMs. That is, as the BIMs grow out from the RPOs, they must not burn through an RPO. Said another way, each RPO must never pass through its own BIM or that of

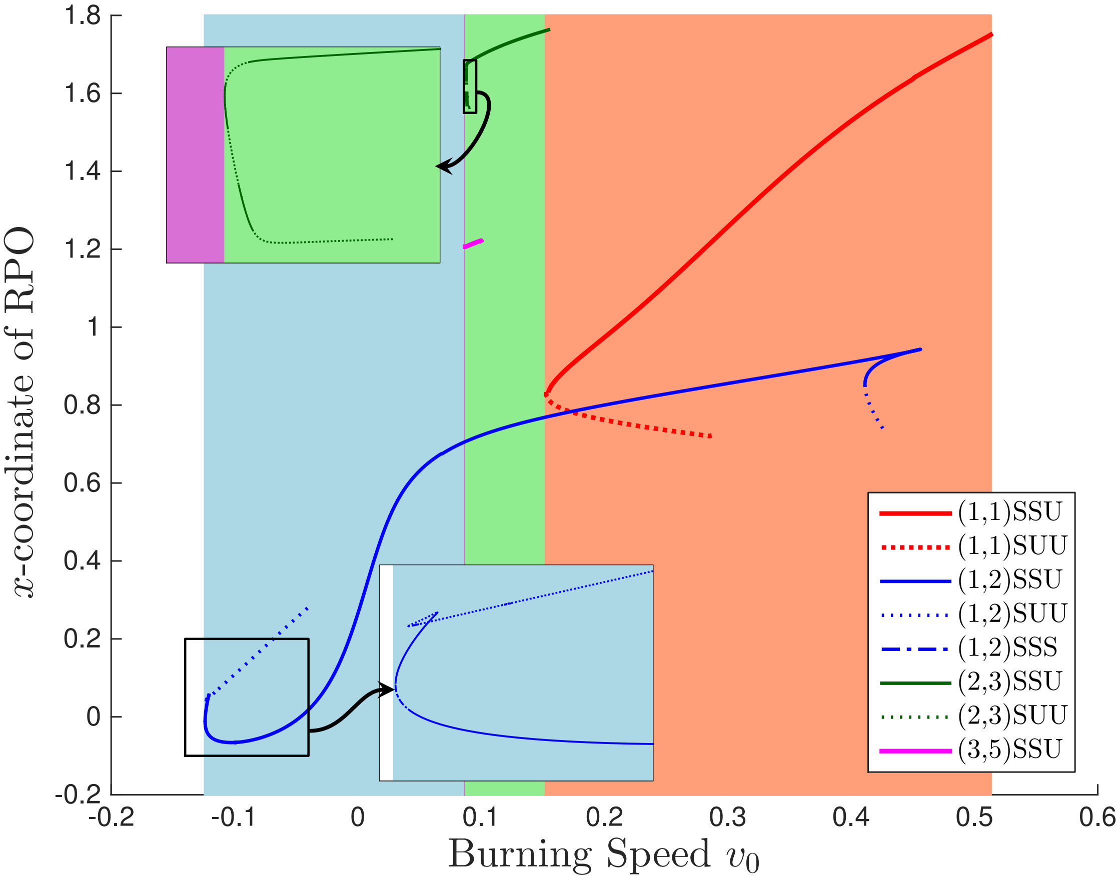

Figure 2.10. Bifurcation diagram of the RPOs as a function of v_0. Multiple RPOs exist for the same parameters. Average front speed of dominant ML front (Eq. 2.2) is monotonic in v_0. Insets shows that each ML RPO is created in a saddle-node bifurcation.

another SSU RPO. This possibility will be discussed in greater detail in Sect. 4.3.1.

2.4 Changes in mode-locking as v_0 is increased.

The dynamical systems approach outlined in Sect. 3.3.2 leads to a greater understanding of the underlying mechanism for mode-locking. Figure 2.10 is a plot of the x-coordinate of one point of an RPO as a function of front speed v_0. Here we show SSU and SUU RPOs for mode-locking types (1,1), (1,2), (2,3), and (3,5). Following the burning speed from left to right we see that mode-locking orbits are born in saddle-node bifurcations.

Figure 2.10 also shows that for a given value of v_0, multiple RPOs can coexist. The mode-locking type that is physically realized will be the type with the fastest RPO. This must be true because the mode-locked front with the fastest burning speed will overtake any other RPOs present engulfing them in the burned region. Note that while the overtaken RPO may temporarily exist within a void, this void will vanish in a finite time as argued previously. Thus it is not possible to have two simultaneous mode-locking types. We refer to the fastest mode-locking RPO (or front) as being *dominant*.

Observe that the mode-locking front speed increases monotonically with v_0 as can be seen from the progression of mode-locked types from (1,2) → (3,5) → (2,3) → (1,1), with speeds in proportion to $1/2 \to 3/5 \to 2/3 \to 1$. To explain this monotonicity consider the evolution of a mode-locked front with parameter v_0. Now consider the evolution of the same initial front with parameter $v_0 + \epsilon$. The region burned by the second front will be a superset of the region burned by the original mode-locked front. Therefore the front with the larger v_0 cannot travel more slowly.

Notice that the loss of a particular mode locking type (N, M) is not due to the disappearance of the (N, M) RPO. For example, in Fig. 2.10, the (1,2) SSU RPO disappears in a saddle-node bifurcation at $v_0 \approx 0.45$. However, by this value of v_0, the (1,1) RPO has already taken over the dominant mode-locking role. In fact, the mode-locking role is lost even earlier, by $v_0 \approx 0.09$ when the (3,5) RPO is created. The question remains: what has changed about the structure of the (1,2) SSU RPO and its unstable manifold that causes it to lose its dominance? Clearly, it will lose dominance as soon as a faster RPO is created. But, can we determine when dominance is lost by looking at the RPO and its unstable manifold alone? We shall see below that loss of dominance coincides with a global bifurcation in the structure of the unstable manifold.

Figure 2.11a shows a $(1, 2)$ RPO and a piece of its BIM at time $t = 0$, with burning speed $v_0 = 0.0873$. Using the data from Fig. 2.10, it can be shown that there is also a mode-locked front of type $(3, 5)$ at this value of v_0. Because the $(3, 5)$ RPO is faster, we can conclude that the $(1, 2)$ RPO cannot be dominant. What about the structure of the $(1, 2)$ front causes it to lose its dominance? To appreciate the mechanism at work, we evolve the $(1, 2)$ front forward one period in Figure 2.11. Over that time, the RPO moves upward from the bottom boundary to the top boundary. At the same time, the BIM develops a long “finger" along the top boundary, Figs. 2.11b and 2.11c. As the RPO continues upward it collides with the finger; importantly, it may then pass into the finger because the colliding fronts have opposite burning directions, Fig. 2.11d. Finally, at the end of one period, the

RPO is no longer on the bounding front. As discussed in Sect. 3.3.2, a physical mode-locked front must be the boundary between the burned and unburned regions, and thus this RPO fails to generate a dominant mode-locked front. In other words, an RPO fails to be dominant if it passes through its own BIM or the BIM of another mode-locked RPO. This is already implied in Proposition 2.3.2 by the statement: “The mode-locked front is obtained from those points on the BIMs of the RPOs that have never previously struck some other point on the BIMs.” The reason Fig. 2.11a is deceptive is because we have not plotted a sufficiently long piece of the BIM. A necessary condition, and a nice check, for whether an RPO is dominant is that the evolution of the front over one period does not produce any new segments on the bounding front, which is clearly violated in Fig. 2.11. Finally, when varying v_0, a dominant mode-locked front loses its dominance at that value of v_0 where the RPO first lies on (the xy-projection of) the BIM itself.

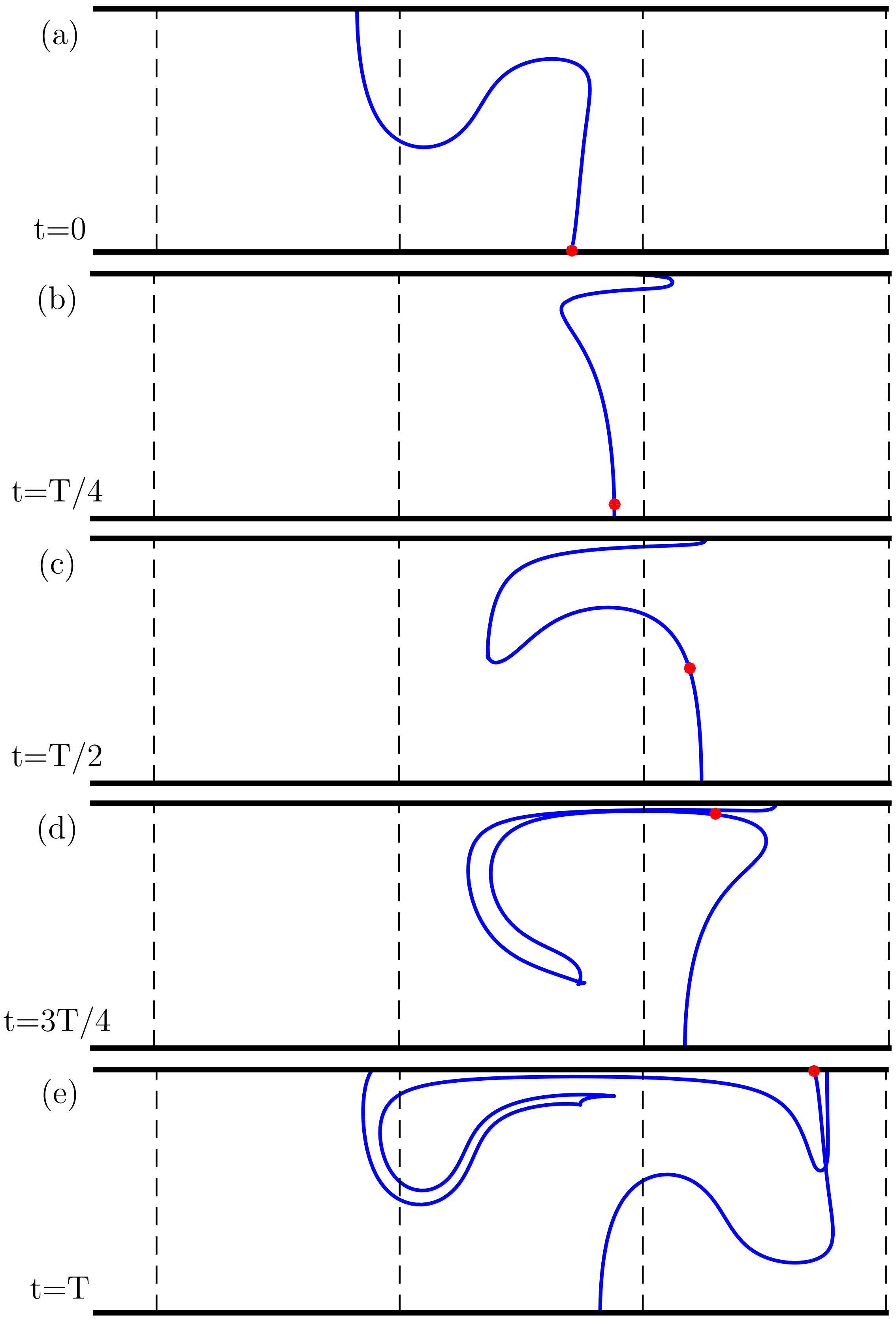

Figure 2.11. The mechanism by which the (1,2) mode-locked front loses its domanince with $v_0 = 0.0873$. (a) At $t = 0$ the RPO sits near the channel boundary. (b,c) The RPO moves upward while the front develops a long "finger" along the top boundary. (d) The RPO moves up, colliding with the "finger". Oppositely oriented fronts can interpenetrate. (e) Final frame shows a bounding front with multiple components. This RPO is no longer on the bounding front, and therefore not the RPO associated with the dominant mode-locking type.

Chapter 3

Time Aperiodic

3.1 Introduction

Combining chaotic advection with that of front propagation has received much attention over the last few decades. One reason is because of new technological applications like chemical reactions in microfluidic devices [17], one example in particular being microreactors [64]. Other examples range from the ozone in the atmosphere [19, 55], population dynamics [28, 52, 53] and combustion [22, 30, 63].

Previous theoretical work in this area has concentrated on flows that are either time-independent or time-periodic. Previous work by Mitchell et. al has demonstrated that analogous manifolds termed *burning* invariant manifolds (BIMs), to those found in advection-diffusion systems exits for time-independent [34, 35, 42] and time-periodic [32, 37] reacting flows. This analysis breaks down when the underlying fluid has an aperiodic time dependence. To address this, Mitchell et. al developed a theory of prominent one-way barriers, *burning* Lagrangian coherent structures (bLCSs), that exists over a finite time interval [36]. Similar to the variational approach in time-aperiodic advection-diffusion systems by Haller et. al, Mitchell seeks to find curves that maximize the average normal repulsion. In this paper he outlines the theory and shows for a time-independent flows, as the integration time of the associated Cauchy-Green strain tensor increases, the bLCS converges to the BIM. In this chapter we show the utility of the theory of bLCSs applied to a time-aperiodic fluid flows and extract the most repelling (attracting) curves.

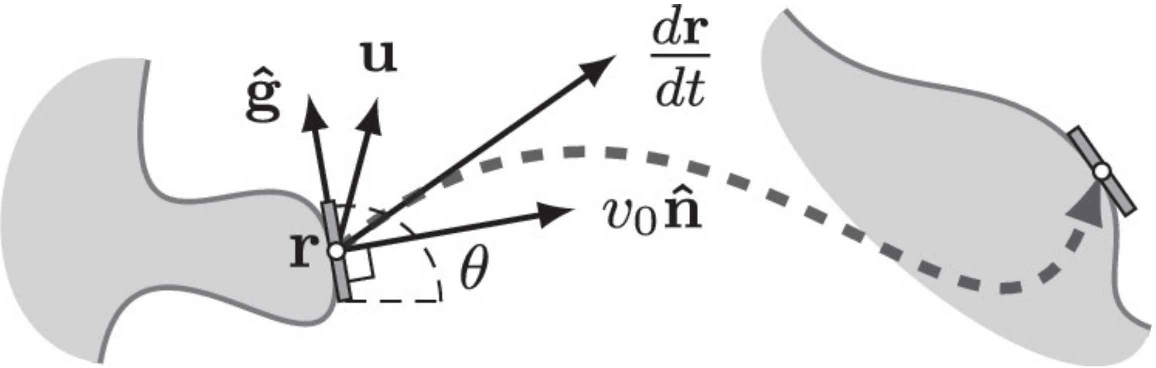

Figure 3.1. A front is defined as the oriented boundary between reacted and unreacted regions where the local orientation vector $\hat{\mathbf{n}}$ is normal to the reaction front and points *away* from the burned region. If $\mathbf{r}$ is used to denote the xy-position of a front element and θ as the angle between the positive x-axis and $\hat{\mathbf{g}}$, each front element, specified by $(\mathbf{r}(t), \theta(t))$, evolves via eq. (2.4)

The structure of this chapter is outlined as follows. Section 3.2.1 introduces the three-dimensional dynamical system for a point along the front. Section 3.2.2 reviews the theory of burning Lagrangian Coherent Structures. Section 3.3.1 shows numerical simulations of the BLCS applied to a linear time varying wind. Section 3.3.2 shows numerical simulations of the BLCS applied to a stochastic wind. Section 3.4.1 discusses the bounding nature of BLCS. Section 3.3.3 discusses the basin of attraction associated with a BLCS. Section 4.3.2 provides concluding remarks and possible future work. Our numerical technique for best locating BLCSs is discussed in the appendix.

3.2 Preliminaries

3.2.1 Front-element dynamics

We model ARD systems by considering only the reaction (burning) front. It is more computationally efficient than explicitly modeling the entire fluid state and, we believe, more theoretically insightful. We make use of the following assumptions. First, the reaction time-scale is much faster than the diffusion time-scale, providing a sharp front in relation to the scale of the fluid flow. This is known as the “sharp front” or geometric optics limit. Each fluid element is either reacted or unreacted and these two regions are separated by a well-defined boundary—the reaction front. Secondly, we assume that each front element progresses in a way independent of the local curvature of the front. It is known that this curvature can play an important role in certain systems [44]. Lastly, we assume that the front propagates with a speed v_0 that is homogenous and isotropic in the comoving fluid frame.

A front is defined as the oriented boundary between reacted and unreacted regions where the local orientation vector $\hat{\mathbf{n}}$ is normal to the reaction front and points *away* from the burned region. The orientation might also be specified by the tangent vector $\hat{\mathbf{g}}$, where $\hat{\mathbf{g}}$ is orthogonal to $\hat{\mathbf{n}}$ and $\hat{\mathbf{n}} \times \hat{\mathbf{g}} = +1$. If $\mathbf{r}$ is used to denote the *xy*-position of a front element and θ as the angle between the positive *x*-axis and $\hat{\mathbf{g}}$, a front in three-dimensional *xy*θ-space is a curve that satisfies the *front-compatibility criterion*

$$\frac{\mathrm{d}\mathbf{r}}{\mathrm{d}\lambda} \propto \hat{\mathbf{g}}(\theta), \tag{3.1}$$

where λ is the Euclidean length parameter measured in *xy*-space that increases in the + $\hat{\mathbf{n}}$ direction.

Each front element, specified by $(\mathbf{r}(t), \theta(t))$, evolves via

$$\dot{\mathbf{r}} = \mathbf{u} + v_0 \hat{\mathbf{n}}, \tag{3.2a}$$

$$\dot{\theta} = -\hat{n}_i u_{i,j} \hat{g}_j, \tag{3.2b}$$

where $\mathbf{u}$ is the incompressible fluid velocity. Numerically, a front is comprised of a collection of fluid elements that propagate independently of one another. New points are added by interpolation to maintain a smooth curve. The unit vectors $\hat{\mathbf{n}} = (\sin\theta, \cos\theta)$ and $\hat{\mathbf{g}} = (\cos\theta, \sin\theta)$ represent the normal and tangent directions of a front element respectively. We use the notation $u_{i,j} = \partial u_i / \partial r_j$, and repeated indices indicate summation. Thus, Eq. (3.2a) shows that each fluid element is translated by the vector sum of the fluid velocity and the burning velocity. Furthermore, the change in angular orientation is determined solely by the local behavior of the fluid flow.

3.2.2 Burning Lagrangian Coherent Structures (bLCSs)

In seeking to model more realistic flows with arbitrary time-dependence, we base our approach on the work of Hallar et. al. which uses a variational approach to define LCSs. [26]. One advantage in adapting this approach to the case of front propagation is that it is based from the start on a search for curves in xy-space. This solves the challenge of dimensions one might incur in trying

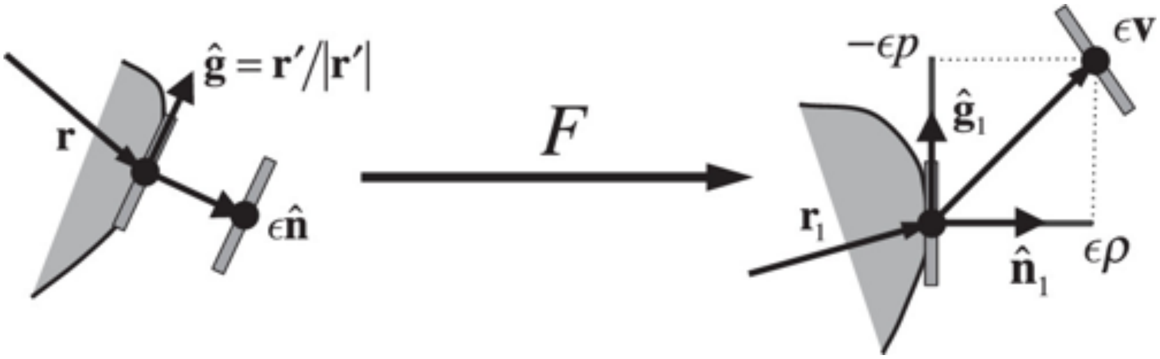

Figure 3.2. Given an initial front, a small normal displacement of a front element, $\epsilon\hat{n}$, evolves under F to a vector $\epsilon\mathbf{v}$. This new evolved front element will in general have a nonzero tangential component. We define the Lagrangian shear p over time interval t to be the projection of $\epsilon\mathbf{v}$ in the tangent direction divided by ϵ. Similarly we define the normal repulsion ρ to be the projection of $\epsilon\mathbf{v}$ in the normal direction divided by ϵ.

to adopt the FTLE-ridge approach to that of front propagation. The dynamics of a front element in two spatial dimensions is naturally represented as a three-dimensional dynamical system, with x and y the two spatial coordinates and θ the orientation of the front element (Sec. 3.2.1). Note that the objects of current interest, the bLCSs, are still one-dimensional curves; just like the BIMs they seek to generalize; that is, a bLCS is not a codimension-one object in our study. Thus a possible implementation of the FTLE-ridge approach to that of front element dynamics would not seek to follow 1D ridges in a 2D space, or even 2D ridges in a 3D space, but rather to follow 1D ridges in a 3D space. There is no obvious reason why curves in the 3D phase space would correspond to fronts in the xy-position space, since a curve in the 3D space must satisfy the front-compatibility criterion (Sec. 3.2.1) for it to be the lift of a front in xy-space.

To find the bLCSs, first we assume that the fluid velocity $\mathbf{u}(\mathbf{r}, t)$ is defined between an initial time, t_0, and a later time $t_1 = t_0 + T$. There is no requirement that the flow be either time-independent or time-periodic over interval $[t_0, t_1]$. The trajectory of a front element over $[t_0, t_1]$ is obtained by solving Eq. 2.4. The flow map that takes an initial point in (r, θ)-space to a final point after solving Eq. 3.2 is defined to be $F = F_{t_0}^{t}$. Lagrangian shear and normal repulsion are defined as follows (see Fig. 3.2) Given an initial front, a small normal displacement of a front element, $\epsilon\hat{n}$, evolves to a vector $\epsilon\mathbf{v}$. This new evolved vector will in general have a nonzero tangential component. We define the Lagrangian shear p over time interval t to be the projection of $\epsilon\mathbf{v}$ in the tangent direction divided by ϵ. Similarly we define the normal repulsion ρ to be the projection of $\epsilon\mathbf{v}$

in the normal direction divided by ϵ. Thus we can write,

$$p(\mathbf{r},\theta) = \langle -\hat{g}_1, \mathbf{v}\rangle = -\langle \hat{g}(F(\mathbf{r},\theta), [\nabla F]_{xy}\hat{n}\rangle \tag{3.3a}$$

$$\rho(\mathbf{r},\theta) = \langle \hat{n}_1, \mathbf{v}\rangle = \langle \hat{n}(F(\mathbf{r},\theta), [\nabla F]_{xy}\hat{n}\rangle \tag{3.3b}$$

where $[\nabla F]_{xy}$ is the 2x2 projection of the flow map gradient given by,

$$[\nabla F]_{xy} = \Pi_{xy}\nabla F \Pi_{xy}^T, \tag{3.4}$$

with

$$\Pi_{xy} = \begin{pmatrix} 1 & 0 & 0 \\ 0 & 1 & 0 \end{pmatrix}. \tag{3.5}$$

With the definitions of Lagrangian shear and normal repulsion we can look to the variational problem. Following Hallar et al. we seek to find a curve parameterized by γ, the Euclidean distance, that makes the average Lagrangian shear stationary under infinitesimal variations. (Eq. 3.6)

$$\overline{P}_0[\gamma] = \frac{1}{T}\int_0^T p(\mathbf{r},\theta)d\tau, \tag{3.6}$$

We define these curves as perfect shearless fronts or shearless fronts for short. We find shearless fronts utilizing a constraint surface or shearless surface (Eq. 3.7)

$$p(\mathbf{r},\theta) = 0. \tag{3.7}$$

Figure shows a shearless surface A perfect shearless front once lifted by Eq. 3.2 must lie within the shearless surface. Thus a perfect shearless front is the integral curve of a vector field tangent to Eq. 3.7. The normalized tangent vector field is given by

$$\frac{d\mathbf{r}}{d\lambda} = \frac{a}{\sqrt{a^2+b^2}}\hat{g}, \tag{3.8a}$$

$$\frac{d\theta}{d\lambda} = \frac{b}{\sqrt{a^2+b^2}}, \tag{3.8b}$$

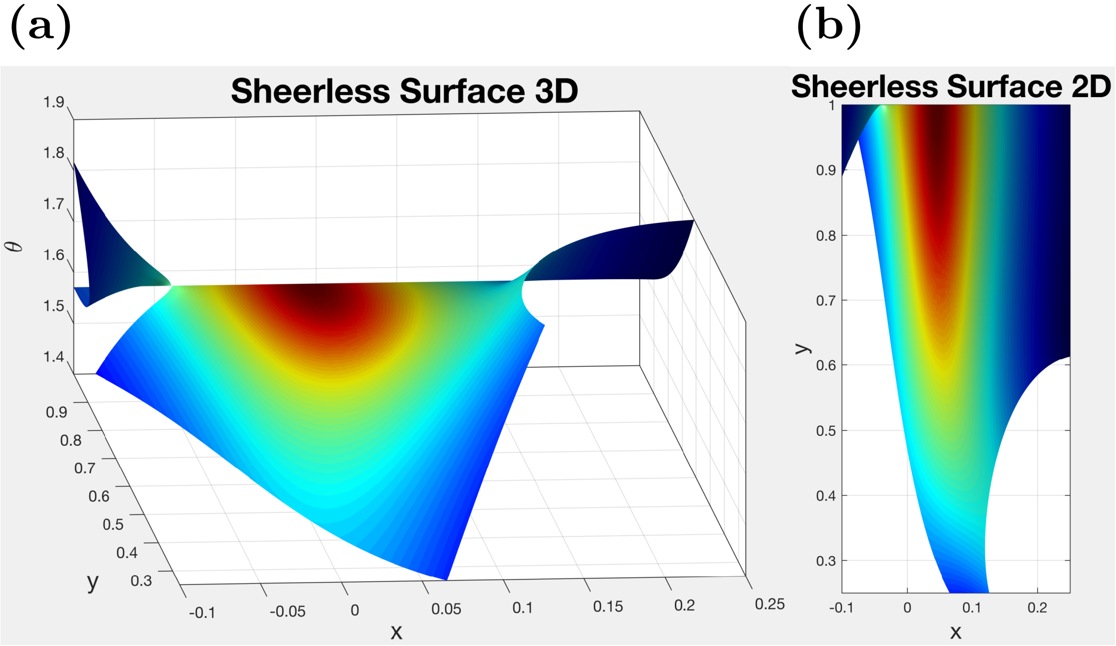

Figure 3.3. (a) Shearless surface in $xy\theta$-space. (b) Two dimensional projection of the shearless surface in xy-space. The coloring corresponds to the value of the normal repulsion, red being a positive value and blue denoting a negative value.

where

$$a = -\frac{d}{d\theta}p, \tag{3.9a}$$

$$b = \hat{g} \cdot \nabla p. \tag{3.9b}$$

We will also need the vector field that is everywhere orthogonal but still tangent to the shearless surface. This field is obtained by replacing $\hat{g}$ with $\hat{n}$ in Eqs. 3.8 and 3.9, i.e.,

$$\frac{d\mathbf{r}}{d\kappa} = \frac{a}{\sqrt{a^2+c^2}}\hat{n}, \tag{3.10a}$$

$$\frac{d\theta}{d\kappa} = \frac{c}{\sqrt{a^2+c^2}}, \tag{3.10b}$$

where

$$c = \hat{n} \cdot \nabla p. \tag{3.11}$$

Once we have reduced the problem to a 2D surface we select the the best shearless curve as that

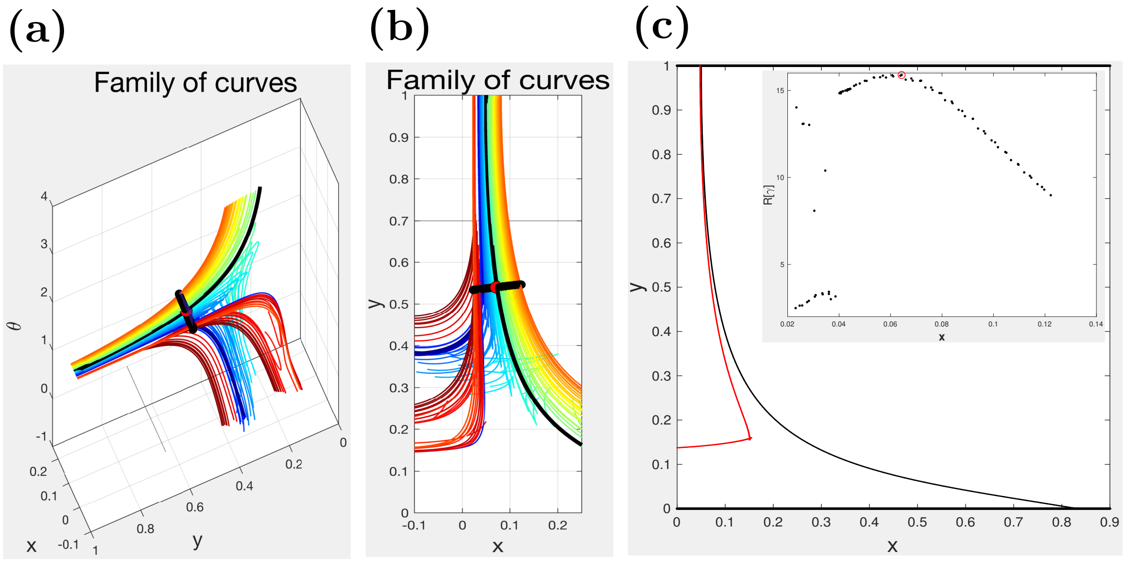

Figure 3.4. (a) Family of shearless curves in $xy\theta$-space. Black line shows a line of initial conditions and black curve shows the BIM. (b) Two dimensional projection of the family of shearless curves in xy-space. (c) Comparison of the BIM (black) and the shearless curve chosen as the bLCS (red), (inset) shows the average normal repulsion curve as a function of the initial condition's x coordinate with the bLCS circled in red.

curve which maximizes the average normal repulsion.

$$R[\gamma] = \frac{1}{L}\int_{\gamma}(\sqrt{\hat{n}\cdot C(\mathbf{r},\theta)}dl, \tag{3.12}$$

where C is the *projected* right Cauch-Green tensor given by,

$$C(\mathbf{r},\theta) = [\nabla F]^{T}_{xy}[\nabla F]_{xy}. \tag{3.13}$$

Figure 3.4(a) shows an example of a family of shearless curves extracted by integrating a line of initial conditions (red) along the tangent vector field Eq. 6.1. Figure 3.4(b) shows the two dimensional projection of the family of curves in xy-space. Figure 3.4(c) shows the average normal repulsion along each of the shearless curves Eq. 3.12. We choose the one with the maximum value, red point, as our bLCS, shown as the black curve in Fig. 3.10(a).

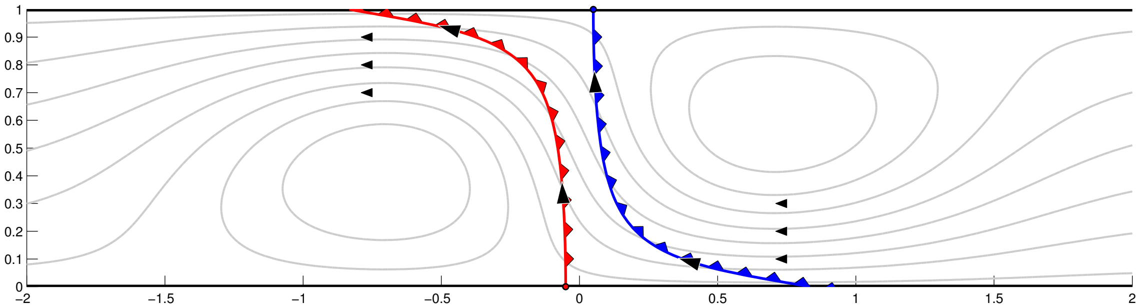

Figure 3.5. Fluid flow derived from the stream function eq. 3.14. The flow takes place in an infinitely long channel with two counter rotating vortices centered at $x = 0$. The channel height is $y = 1$, thus the vortex height and width are unit 1. The black arrows show the direction of rotation of the vortices. The red and blue curves are the unstable and stable burning invariant manifolds respectively. The arrows along the BIMs show their burning direction. This particular image corresponds to a γ value of 1, and $v_w = 0.15$.

3.3 Numerical Simulations

3.3.1 Linear time varying wind

The fluid velocity derives from an infinitely long channel flow with two side-by-side counter rotating vortices Fig. 3.5. Time-dependence is produced by a spatially uniform “wind". If the magnitude of the wind is positive, the direction of the wind is from left to right and if the value is negative the direction is from right to left. The two-dimensional stream function is given by:

$$\Psi(x, y) = (\frac{\gamma}{\pi})x \exp(-x^2) \sin(\pi y) + v_w y, \tag{3.14}$$

where γ is the vortex strength and v_w is the wind speed. The channel width ranges from $y = 0$ to $y = 1$. Previously we were able to show that the bLCS model recaptures the BIM for a constant wind speed, time-independent, flow for longer integration times of the CG tensor [36]. The wind speed was chosen to be $v_w = -0.15$ and the burning speed $v_0 = 0.1$. Here for the unsteady flow we first chose a wind speed that began at $v_w = -0.15$ and linearly decreased to $v_w = -0.1$. Fig. 3.6 shows the wind profile as a function of time. Fig. 3.7 shows the location of the BIMs for constant wind speeds corresponding to the beginning and ending wind speed magnitudes. This wind profile was chosen as a first step in applying this model to a time varying flow in which we know aprior where the BLCS structure should lie, i.e. in between the two BIMs. The suspected bLCS will began in the vicinity of the $v_w = -0.15$ BIM profile, and propagate to the right, to the straight line

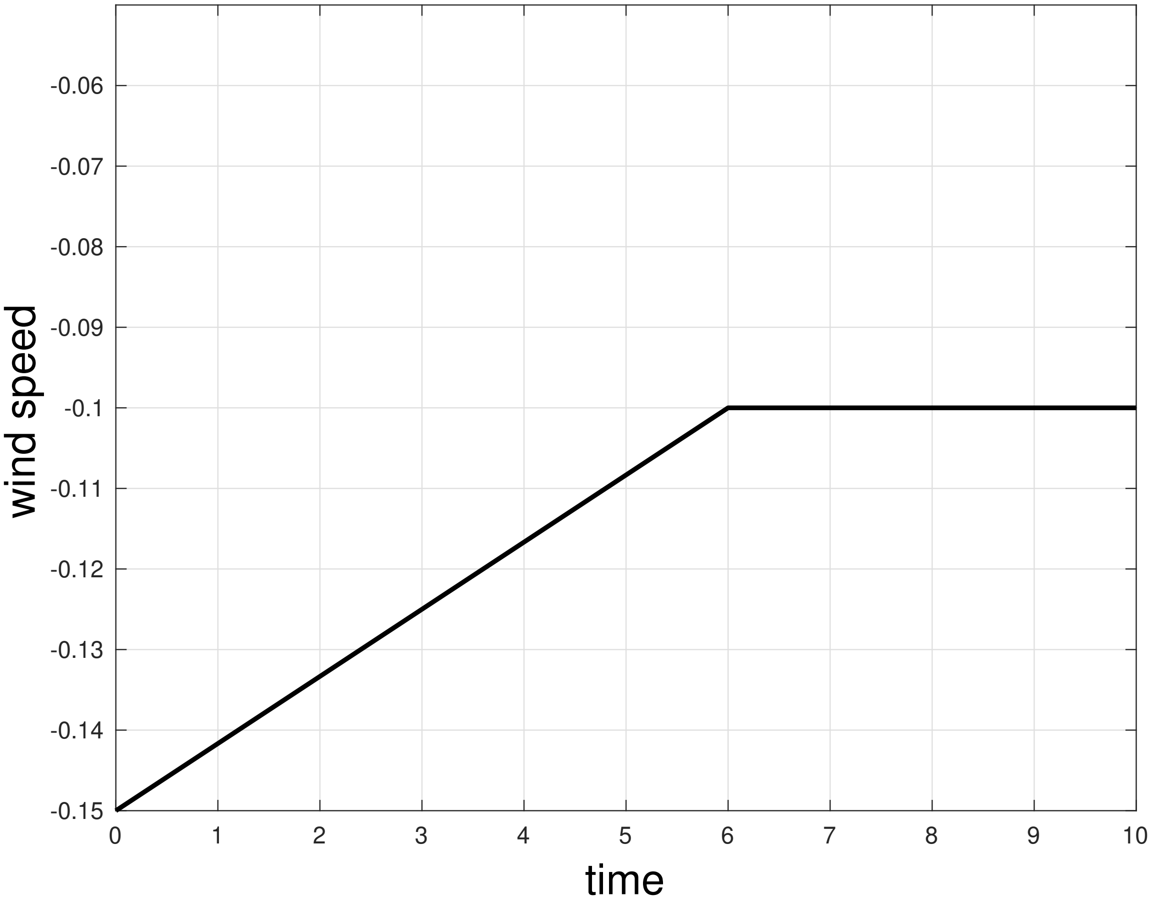

Figure 3.6. Wind speed profile for linearly decreasing wind speed. The wind speed begins with a value of $v_w = -0.15$ and decreases linearly over a time interval $[0, 6]$ to a value of $v_w = -0.1$. It is then held constant at $v_w = -0.1$ from $[6, 10]$. Physically, this corresponds to a wind blowing across the channel from right to left decreasing in magnitude.

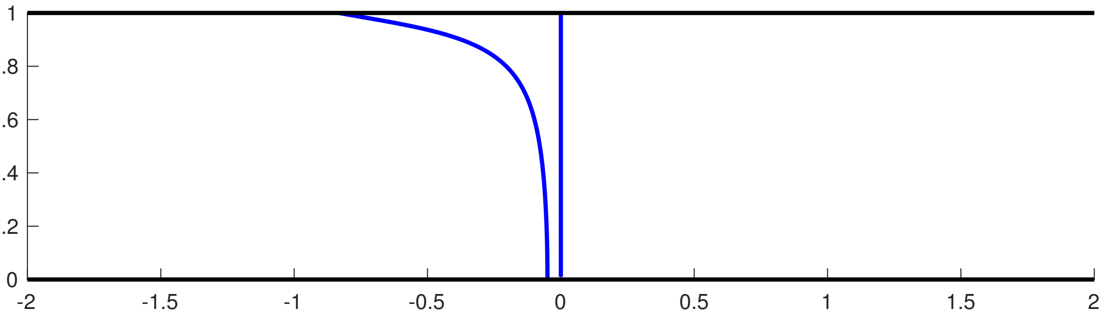

Figure 3.7. Time-independent burning invariant manifolds for constant wind speeds of $v_w = -0.15$ (left) and $v_w = -0.1$ (right). BIMs are generated using eq. 3.2 and take place in a long channel with two side-by-side counter rotating vortices, fig. 3.5.

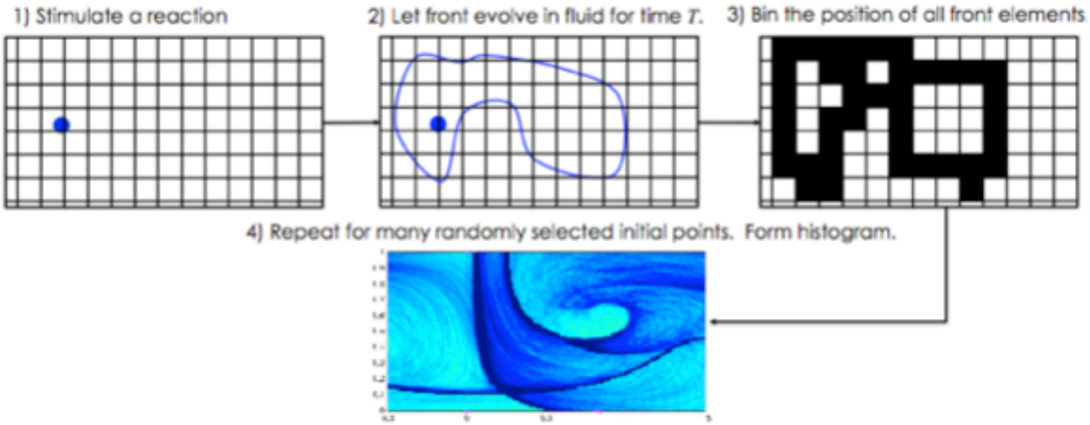
1) Stimulate a reaction
2) Let front evolve in fluid for time T.
3) Bin the position of all front elements
4) Repeat for many randomly selected initial points. Form histogram.

Figure 3.8. Histogram of how data is generated. First the domain is discretized into a uniform grid. Within this domain a reaction is stimulated and evolved forward over some time interval. Next which grids the front propagates to is recorded. This process is repeated for many randomly selected reaction stimulations. Finally a histogram is formed which show areas of highest attraction or front accumulation.

separating the vortices. As the wind speed is held constant at $v_w = -0.1$ the bLCS should look more and more like the seperatrix and lose all remnants of the $v_w = -0.15$ BIM profile.

In leu of experimental data, simulations were run in which a small circular front was stimulated in the fluid domain and allowed to evolve under the flow dynamics for a period of time. We then discretize the fluid domain into a uniform grid and record where the front elements propagated over the prescribed period. This process is repeated for many, approx.1000, randomly selected initial point stimulations. Finally we form a histogram which shows the areas of highest attraction. Fig. 3.8 shows graphically how this process is carried out.

Figure 3.9 shows a histogram in which the flow was evolved forward for an integration time interval of $[0, 8]$. There are three main regions of highest attraction, and thus three candidates for bLCSs. We begin with the middle curve. This curve lies between the BIMs in Fig. 3.7 as expected. From fig. 3.6 we see that at $t_0 = 0$ the wind speed was $v_w = -0.15$ and over the time interval $[0, 6]$ decreases to $v_w = -0.1$ then held constant from $[6, 8]$. Thus our bLCS candidate began near the $v_w = -0.15$ BIM, left curve of Fig. 3.7, and moved to the right as the magnitude of v_w decreased. Since the integration time stops at $t_1 = 8$ we see that the middle curve in Figure 3.9 more closely resembles the BIM on the right of Fig. 3.7. This gives some initial insight into the memory of the system, i.e. how much do earlier wind speeds effect the end profile of the bLCS curves. Fig. 3.10(a)

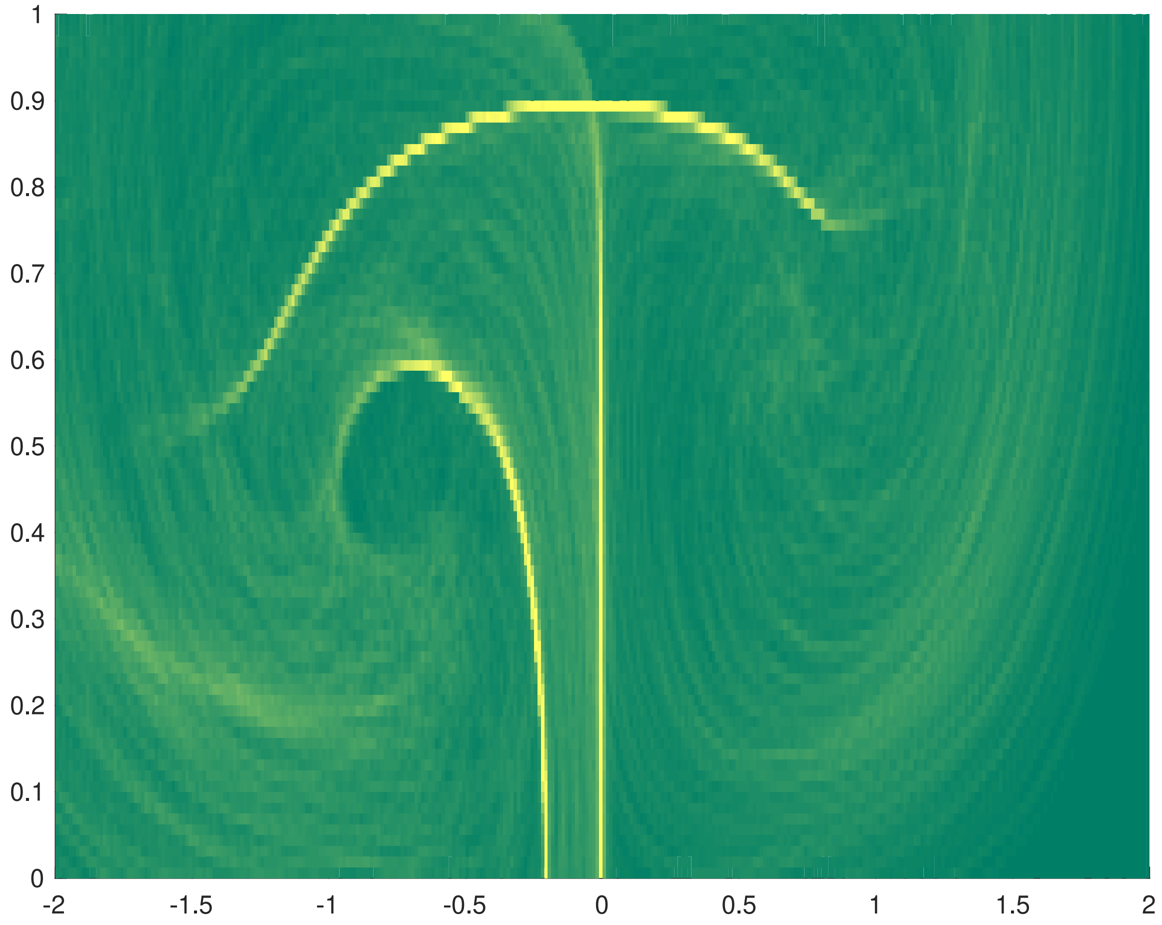

Figure 3.9. Histogram of evolved front stimulations over a time interval $[0, 8]$. There are three regions of highest attraction shown as the yellow curves. The middle curve lies between the BIMs in Fig. 3.7 as expected.

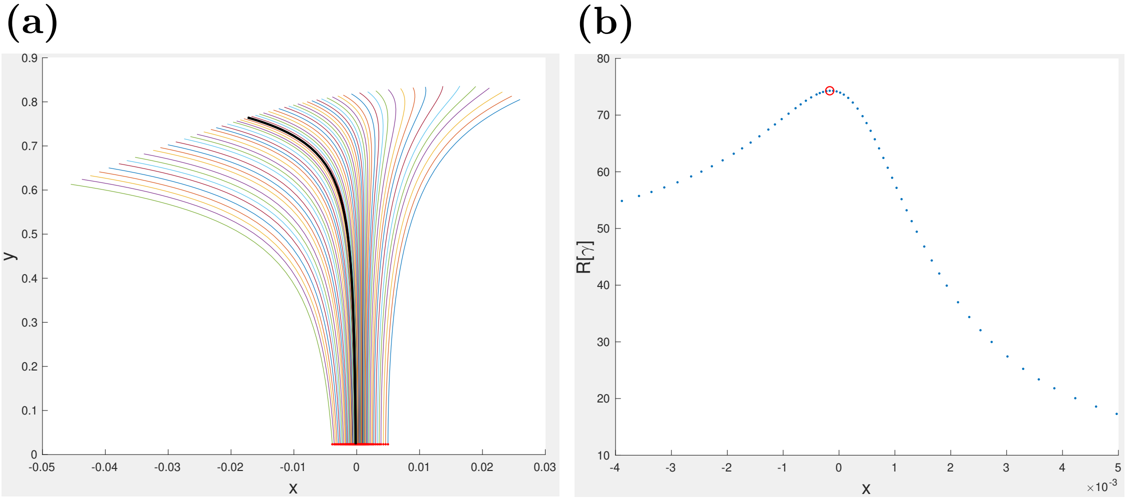

Figure 3.10. (a) Beginning with a single initial condition, the red line is generated by integrating Eq. 3.8 producing a line of initial conditions. With these, the shearless curves are obtained by integrating Eq. 3.10 for some distance. (b) A plot of the average normal repulsion along each of the shearless curves. We choose as our bLCS the one that maximizes the average normal repulsion, (red point), which corresponds to the black curve in the family of shearless curves.

shows a line of initial conditions in red at $y = 0.01$. These were found integrating the normal vector field given by Eq. 3.8. For each of the initial conditions, we then integrate Eq. 3.10 to produce our family of shearless curves. Finally we seek to find the shearless curve with the maximum average normal repulsion Eq. 3.12. Fig. 3.10(b) shows the average normal repulsion calculated along each of the shearless curves. The one with the maximum value is chosen, red point, as our candidate for the bLCS, i.e. black curve in Fig. 3.10(a). Following our method for bLCS extraction laid out in Sec. 3.2.2, we find excellent agreement with the extracted bLCS curve overlaid on our statistical plot Figure 3.11. The end of the bLCS segment, at around $y = 0.85$, terminates here and ceases to follow the underlying yellow curve due to no longer finding a maximum in the normal repulsion. There are remnants of a tail which looks to extend to the top of the channel curving upwards however, it is easy to see that this line is not as dense, thus less attracting. This can also be seen in a plot of the shearless surface for the prescribed integration time. Fig. 3.12(a) shows the shearless surface from $x = [-0.25, 0.25]$, $y = [0, 1]$ and $\theta = [1.45, 2]$. We know that the burning fixed point of the BIMs in fig. 3.7 have a value of $\theta = \pi/2$, and the domain and range for the shearless surface can be determined from figure 3.9. In general, if the theta value is unknown, it is easy to chose a fixed value of x and y that corresponds to a region of interest, then calculate the value of p for each

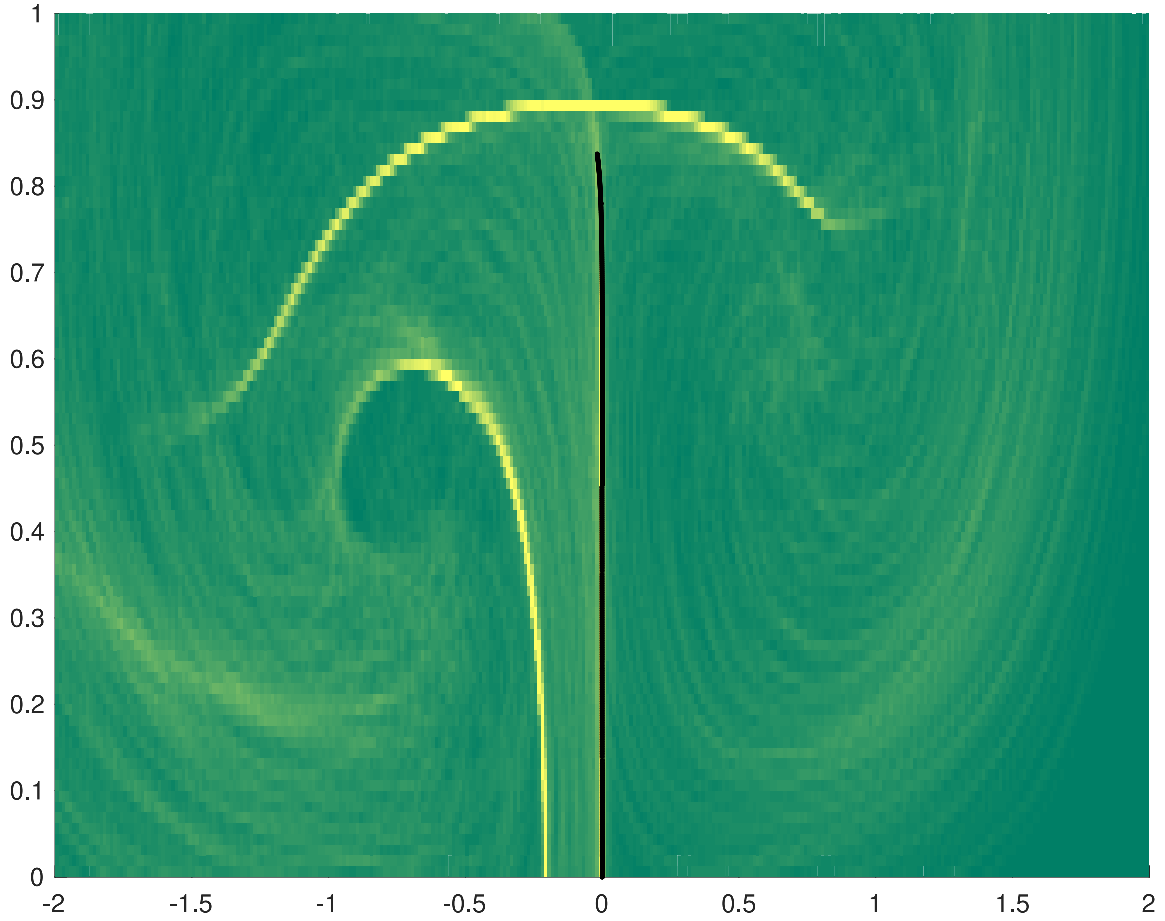

Figure 3.11. Histogram of evolved front stimulations over a time interval $[0, 8]$ with our chosen candidate for the bLCS in black. This was found following the method in laid out in Sec. 3.2.2. The black curve shows good agreement with the underlying region of highest attraction.

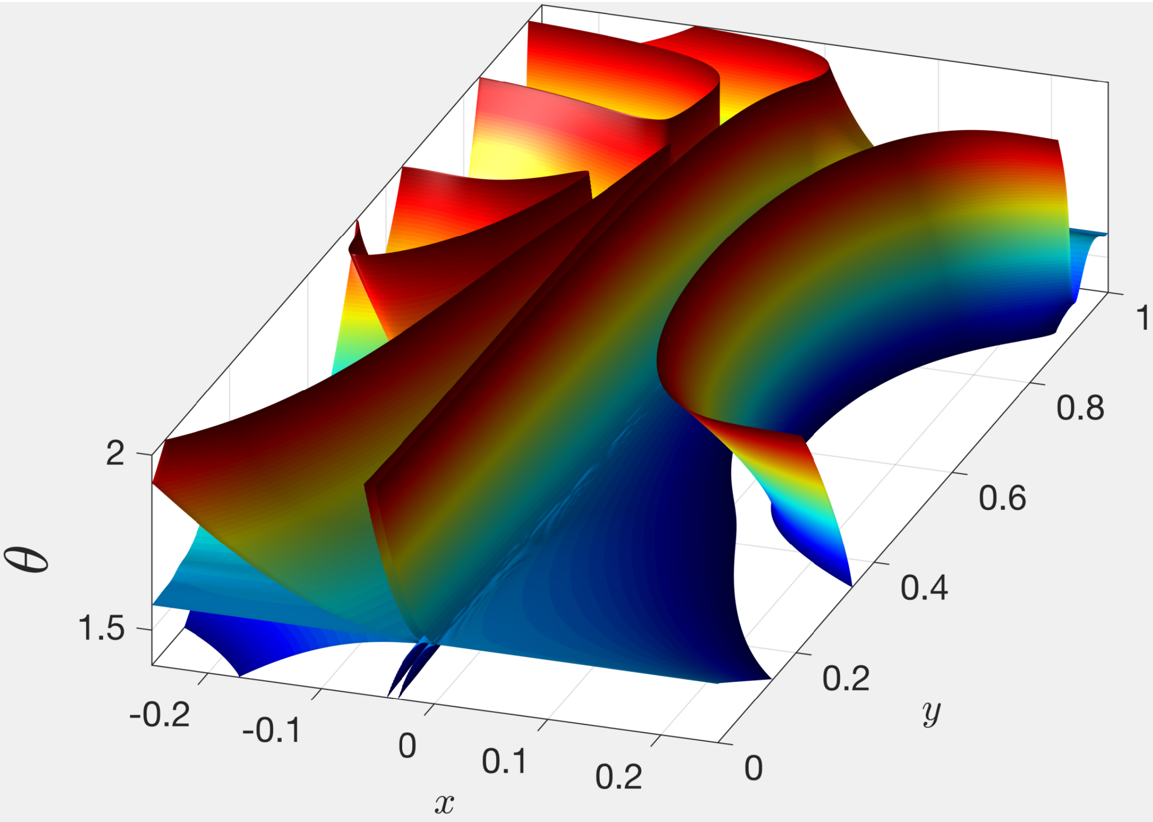

Figure 3.12. The shearless surface from $x = [-0.25, 0.25]$, $y = [0, 1]$ and $\theta = [1.45, 2]$ over time interval $CGT = [0, 8]$. The burning fixed point of the BIM in fig. 3.7 has a value of $\theta = \pi/2$, therefore we know apriori the corresponding branch of the shearless surface the bLCS should lie within. The colormap is scaled with the value of θ.

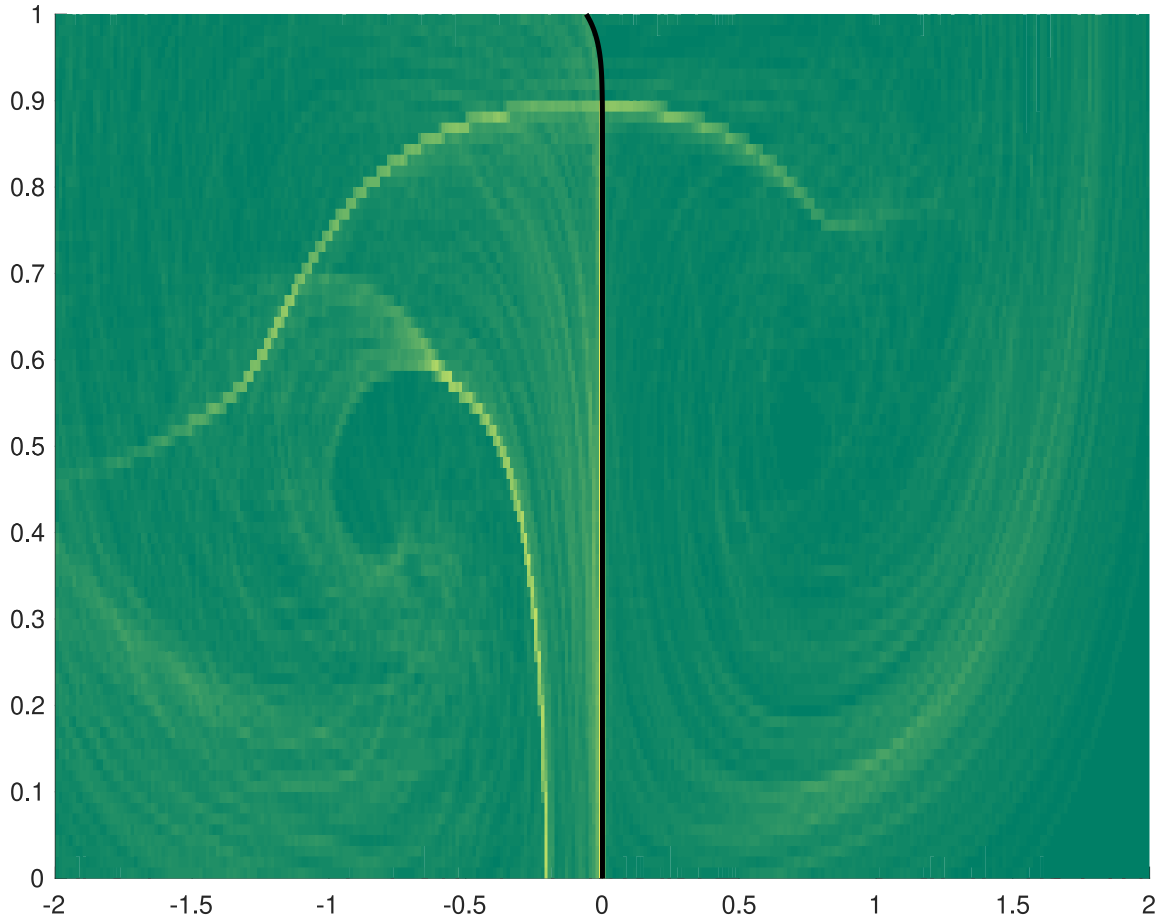

Figure 3.13. Histogram of evolved front stimulations over a time interval $[0, 10]$ with our chosen candidate for the bLCS in black. This was found following the method in laid out in Sec. 3.2.2. The black curve shows good agreement with the underlying region of highest attraction.

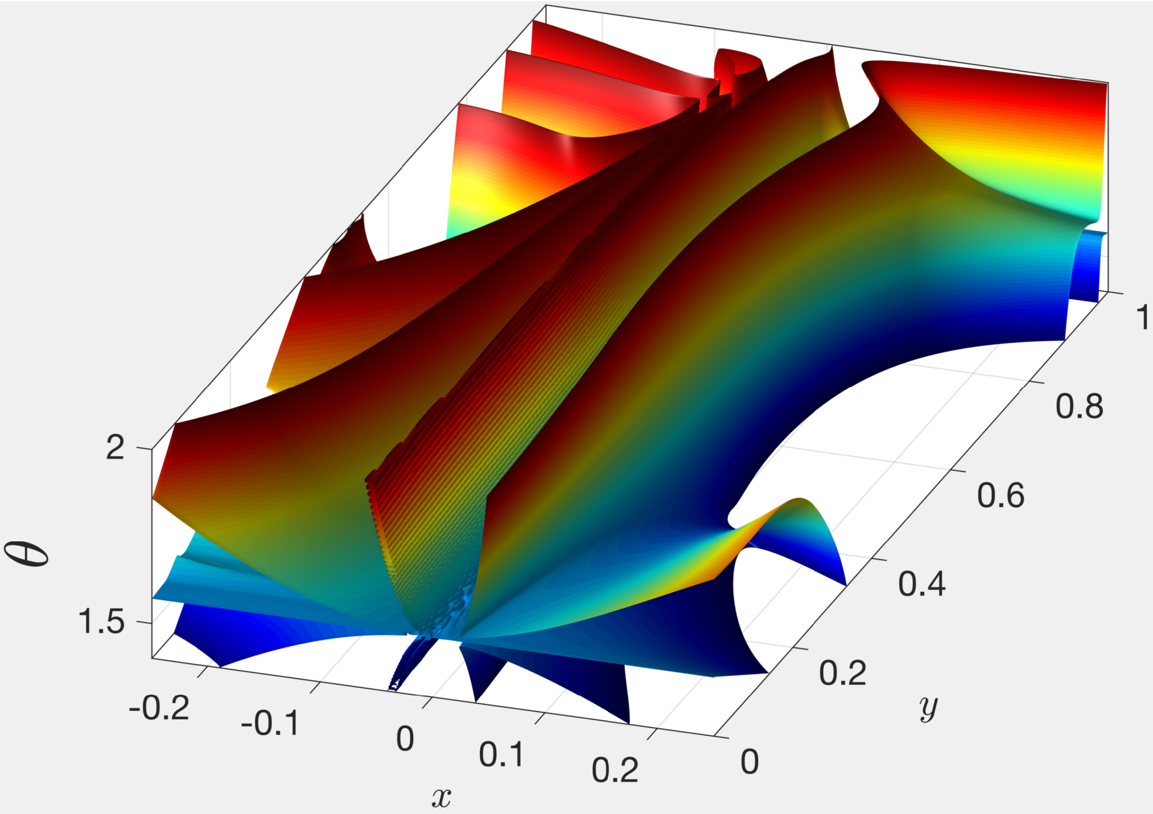

Figure 3.14. The shearless surface from $x = [-0.25, 0.25]$, $y = [0, 1]$ and $\theta = [1.45, 2]$ over time interval $CGT = [0, 10]$. The colormap is scaled with the value of θ

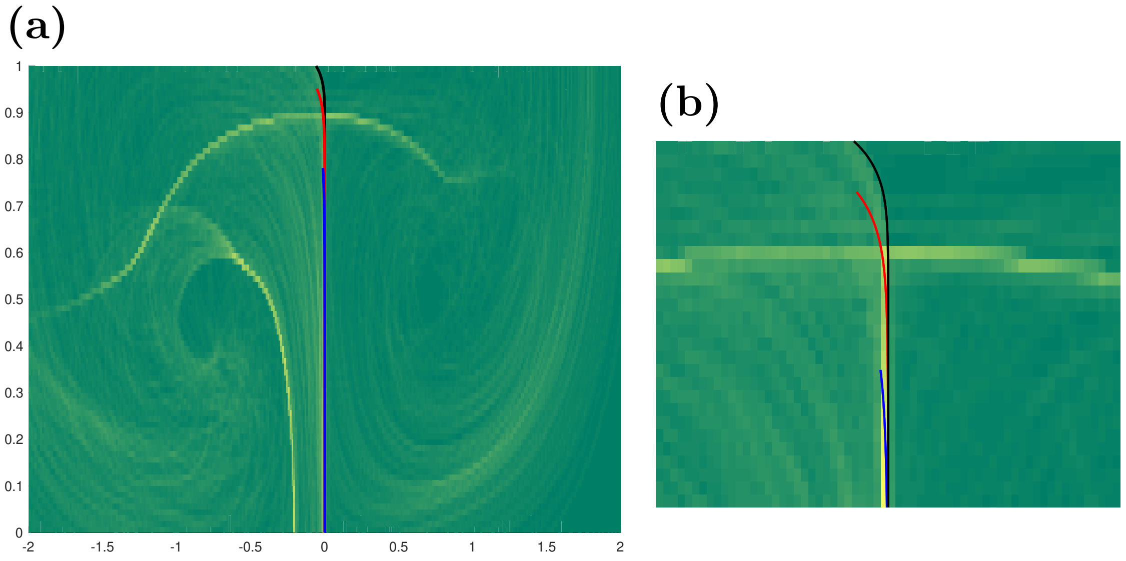

Figure 3.15. Evolution of bLCS under F. Statistical plot for an integration time of $t_1 = 10$. The blue curve, the bLCS extracted for $t_1 = 8$, was evolved forward one time unit to $t_1 = 9$ resulting in the red curve. Evolving the blue curve two time units, or red curve one time unit, forward results in the black curve and ultimately the same result from Fig. 3.13.

value of θ from $[0, 2\pi]$. This allows you to find the $p = 0$ branches of the shearless surface, to then integrate eqs. 3.8 and 3.10 to generate a family of shearless curves.

If instead we wanted to find coherent structures over the entire time interval from $[0, 10]$, we follow the same steps outlined above. Evolving the flow forward in time to $t1 = 10$, Fig. 3.13 shows similarity to Figure 3.9 in overall structure but with some key differences. In particular note that the center curve is more prominant towards the top of the channel, $y = 1$, but also that the "tail" has shifted right, further aligning with the right BIM in fig. 3.7. Figure 3.14 shows the constraint surface over $[0, 10]$, with the central branch, the branch of interest for the current bLCS candidate, also extending further towards the top of the channel with the tail shifting to the right. Figure 3.13 shows the bLCS candidate, black curve, once again follows the underlying yellow region of highest attraction in underlying statistical plot.

In running simulations for bLCS extraction it was found that difficulties can arise when the flow is allowed to evolve for longer periods of time. The difficulties are due to the constraint surface growing in complexity as different branches compress and fold onto one another. Numerical integration techniques fail to distinguish between neighboring branches and can subsequently jump

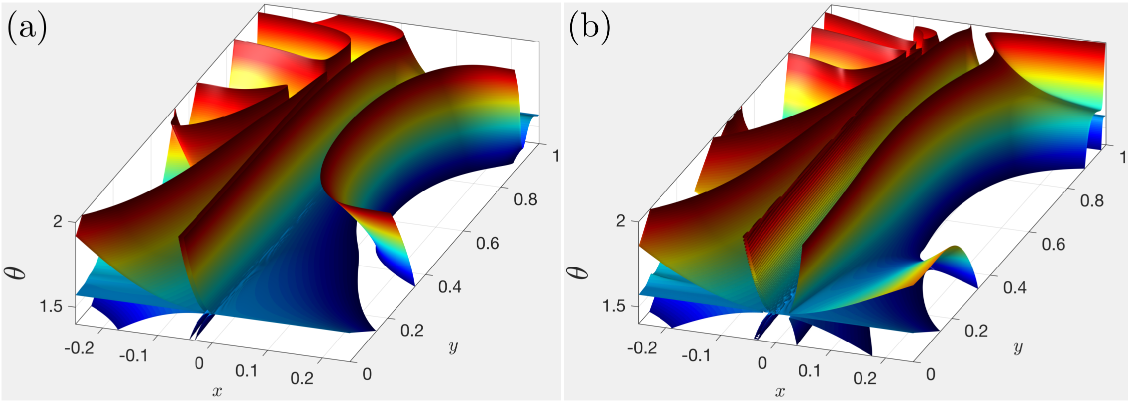

Figure 3.16. Comparison of shearless surfaces for (a) $CGT = [0, 8]$ and (b) $CGT = [0, 10]$

from branch to branch, Fig. 3.16. One simple technique to combat this difficulty is to extract the bLCS for a shorter CG integration time, then evolve the extracted bLCS forward under the map F. Figure 3.15 shows the statistical plot for an integration time of $t_1 = 10$. The blue curve, the bLCS extracted for $CGT = 8$, was evolved forward one time unit to $t_1 = 9$ resulting in the red curve. Evolving the blue curve two time units, or red curve one time unit, forward results in the black curve and ultimately the same result from Fig. 3.13.

3.3.2 Stochastic Time Varying Wind

In this section we move towards a more realistic case of a time-varying wind. The wind profile is generated using a Gaussian (Normal) distribution centered around v_0 with a variance of 0.09. This generates a piecewise linear wind speed profile as can be seen in Fig. 3.17 over a timespan $[0, 8]$. The wind speed begins with a positive value, $v_w = 0.24$, increases slightly before dropping to a negative value at $t = 5$. For the next 3 time steps the wind speed magnitude oscillates from increasing to decreasing. This profile should simulate a light swirling wind that will impact the reaction front but not cause any turbulence. Also note here the average wind direction will be from left to right since the average value of the wind speed is positive.

Figure 3.18 shows the histogram corresponding to the wind speed profile in Fig. 3.17. The regions of highest attraction are noticeably different. The center curve in Fig. 3.9 has shifted to the right, and the left curve now extends further towards the top of the channel. This result makes sense with the average wind speed being positive and thus from left to right. Figure 3.19 shows

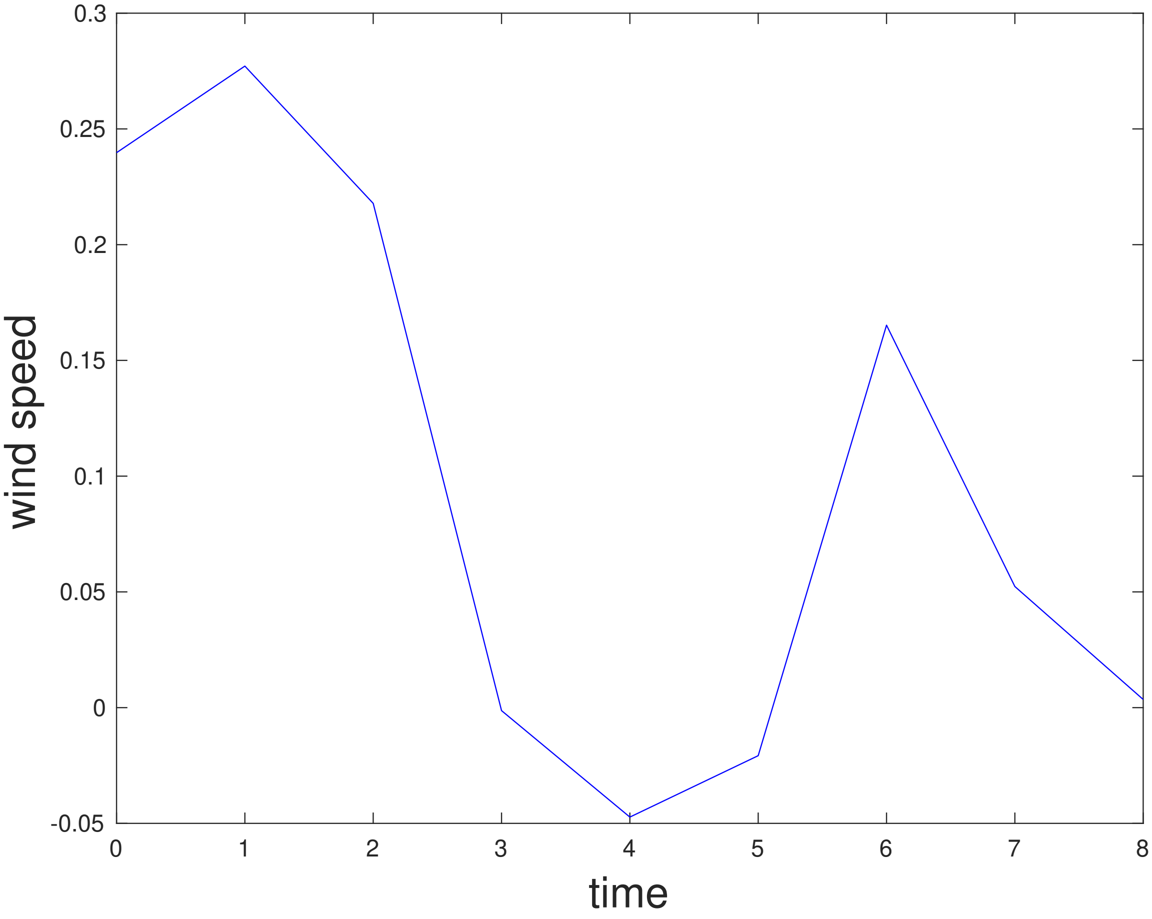

Figure 3.17. Wind profile for a stochastic wind over a time interval $[0, 8]$. This profile is piecewise linear with speeds above and below the burning speed $v_0 = 0.1$. This resembles a swirling wind that changes direction blowing initially from left to right up until $t = 4$, then right to left from $t = 4$ to approximately $t = 6$, and finally back from left to right.

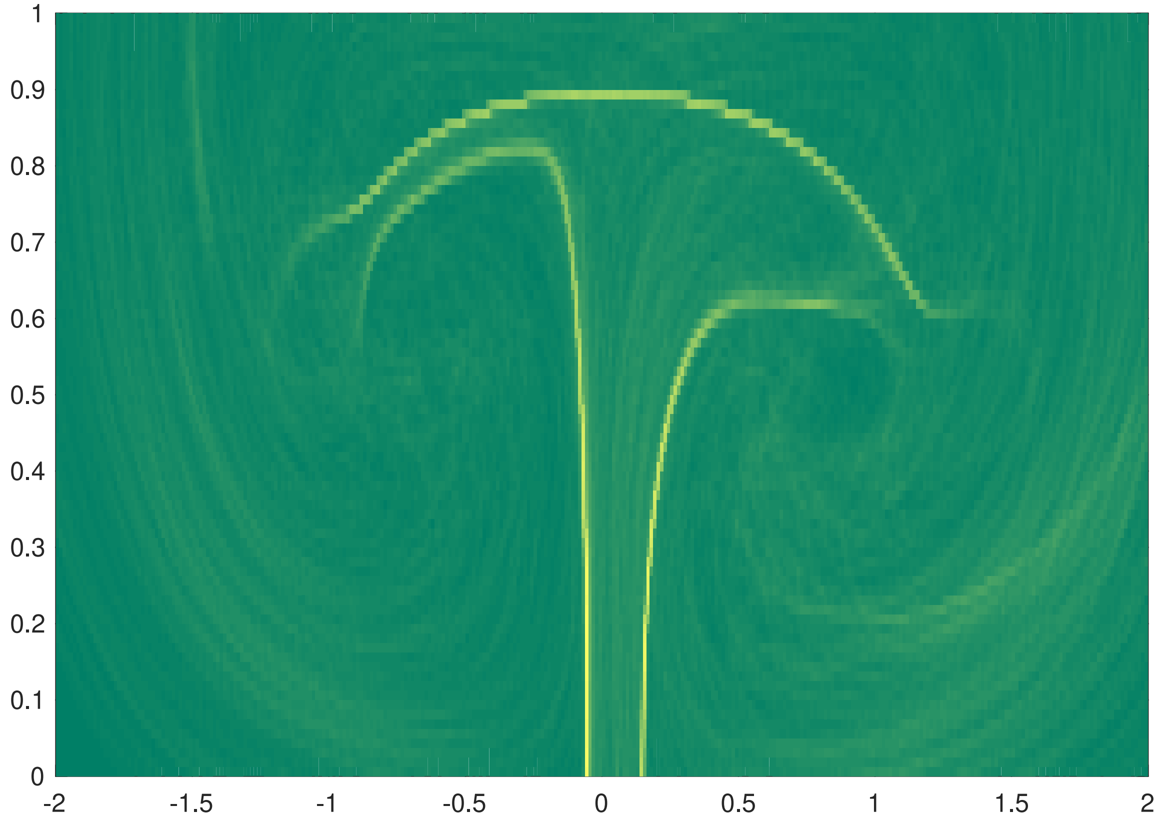

Figure 3.18. Histogram of front stimulations over a time interval $[0, 8]$ with the stochastic wind profile in fig. 3.17. There are three region of highest attraction like in the linearly decreasing wind in 3.3.1, but with noticeable differences. The structure on the left extends further up the channel as expected from a wind profile that on average blows from left to right. The structure on the right has also shifted right.

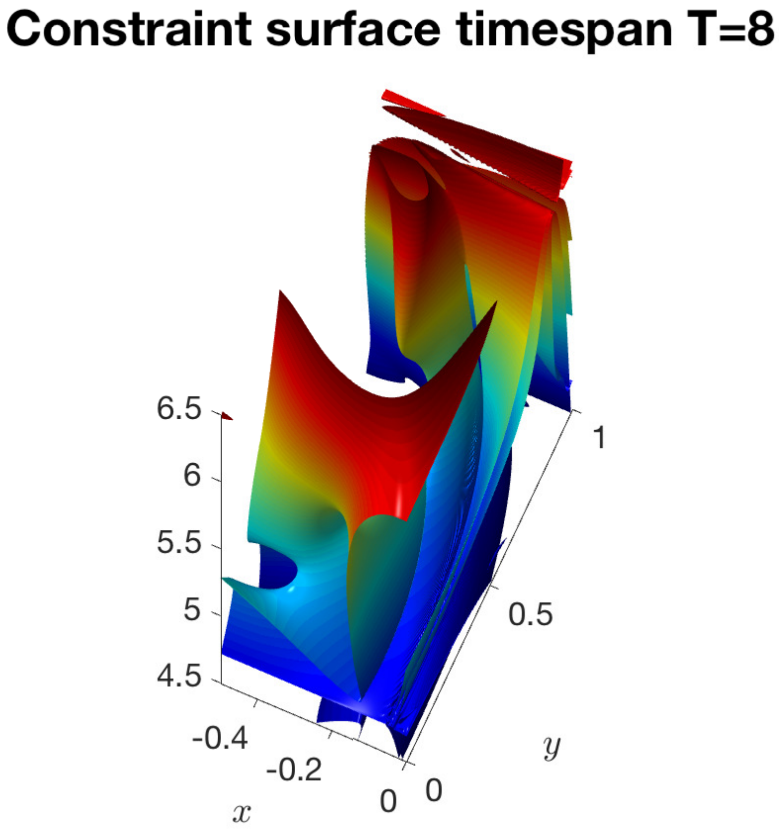

Figure 3.19. Constraint surface $t_1 = 8$. Here the shearless surface is growing quickly in complexity thus a shorter CGT was chosen to extract the bLCS.The colormap is scaled with the value of θ

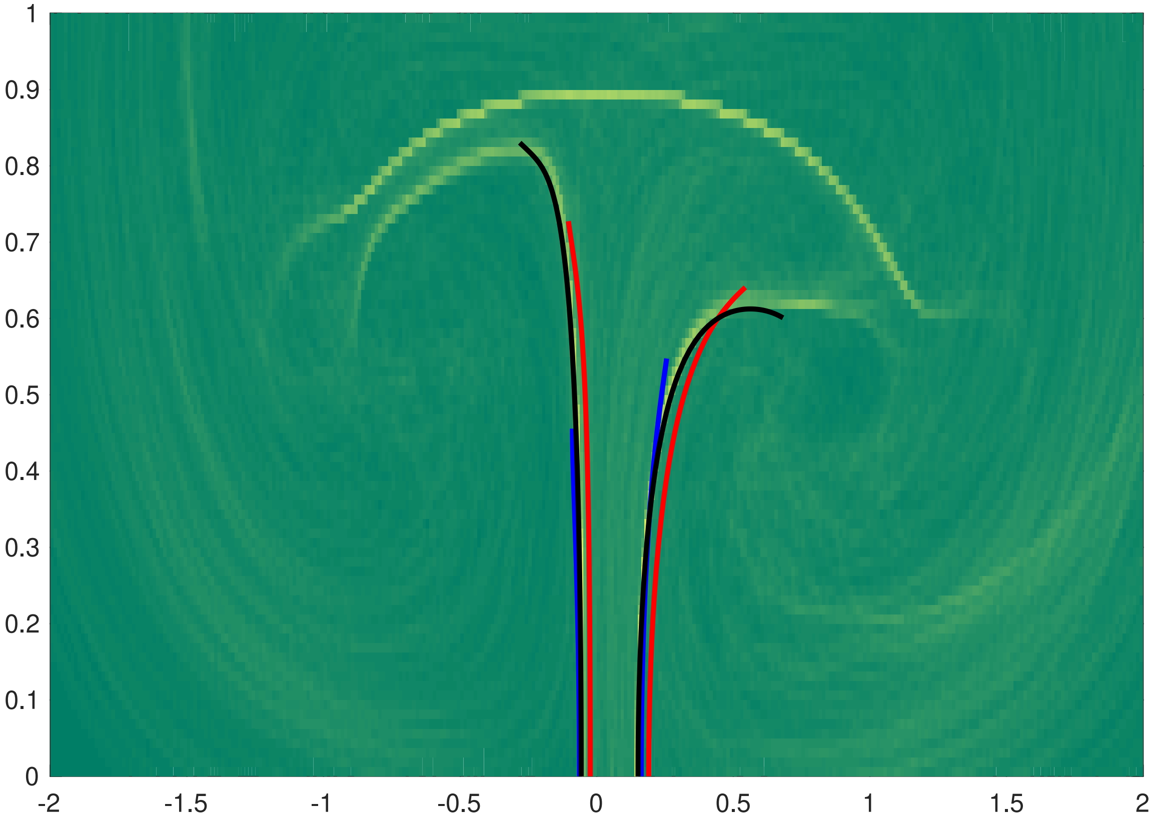

Figure 3.20. The bLCS(s) extracted for $CGT = [0, 6]$ in blue. Evolving the blue bLCS forward one time step results in the red curves, i.e. $CGT = [0, 7]$. Finally evolving forward one more time step results in the black curves, $CGT = [0, 8]$

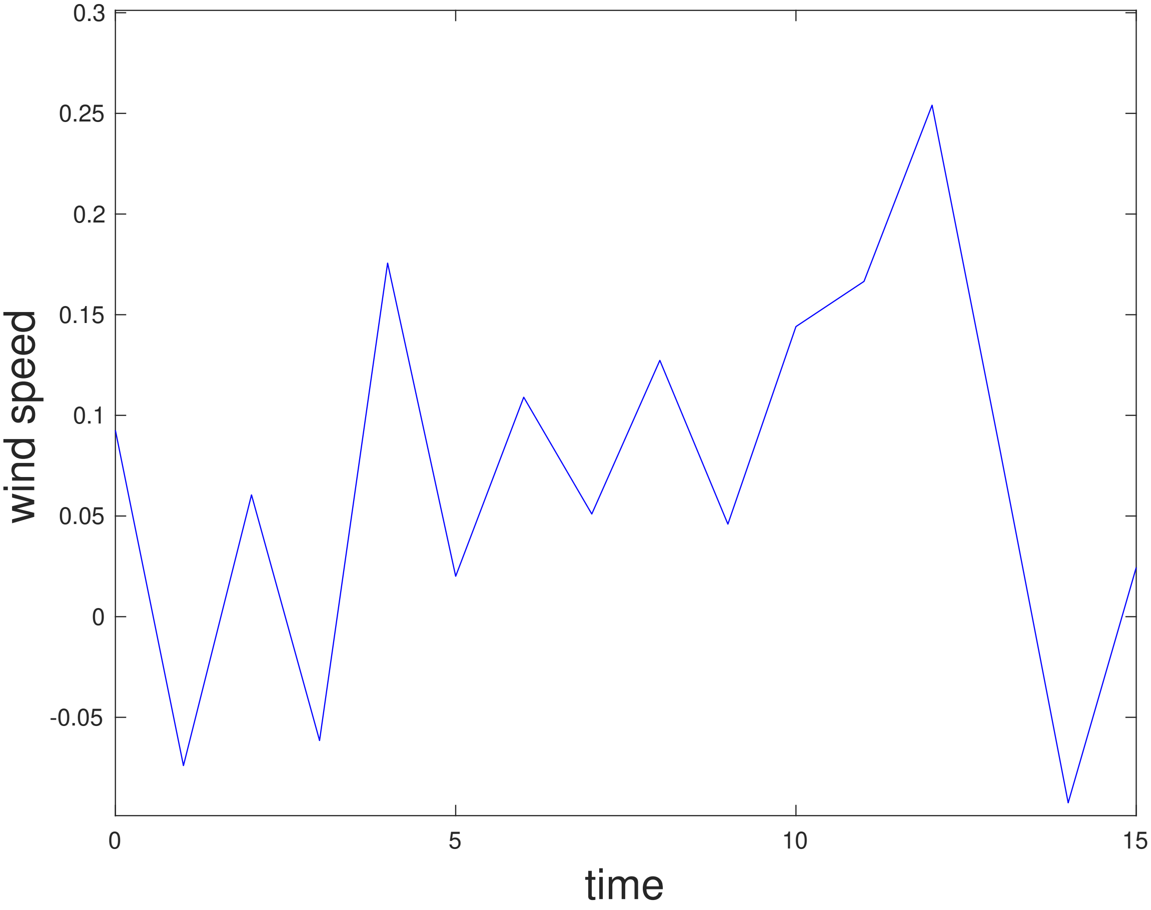

Figure 3.21. Wind profile for a stochastic wind over a time interval $[0, 15]$. This profile is piecewise linear with speeds above and below the burning speed $v_0 = 0.1$. This resembles a swirling wind that blows on average from left to right.

the constraint surface for left bLCS. Notice the shearless surface for $CGT = [0, 8]$ is already quite complex and difficulties may arise in extracting the bLCS over this time interval.

In finding the bLCS(s) we employed the method of using a shorter Cauchy-Green integration time to extract the bLCS and evolve it forward under the map F. Figure 3.20 shows the bLCS(s) extracted for $CGT = [0, 6]$ in blue. Evolving the blue bLCS forward one time step results in the red curves, i.e. $CGT = [0, 7]$. Finally evolving forward one more time step results in the black curves, $CGT = [0, 8]$. Notice that the ends of the black curve, bLCS for $CGT = [0, 8]$, do not follow along exactly with the underlying front accumulation plot. This is once again due to losing a maximum in the normal repulsion as demonstrated earlier for the linear time varying wind case in Sec. 3.3.1.

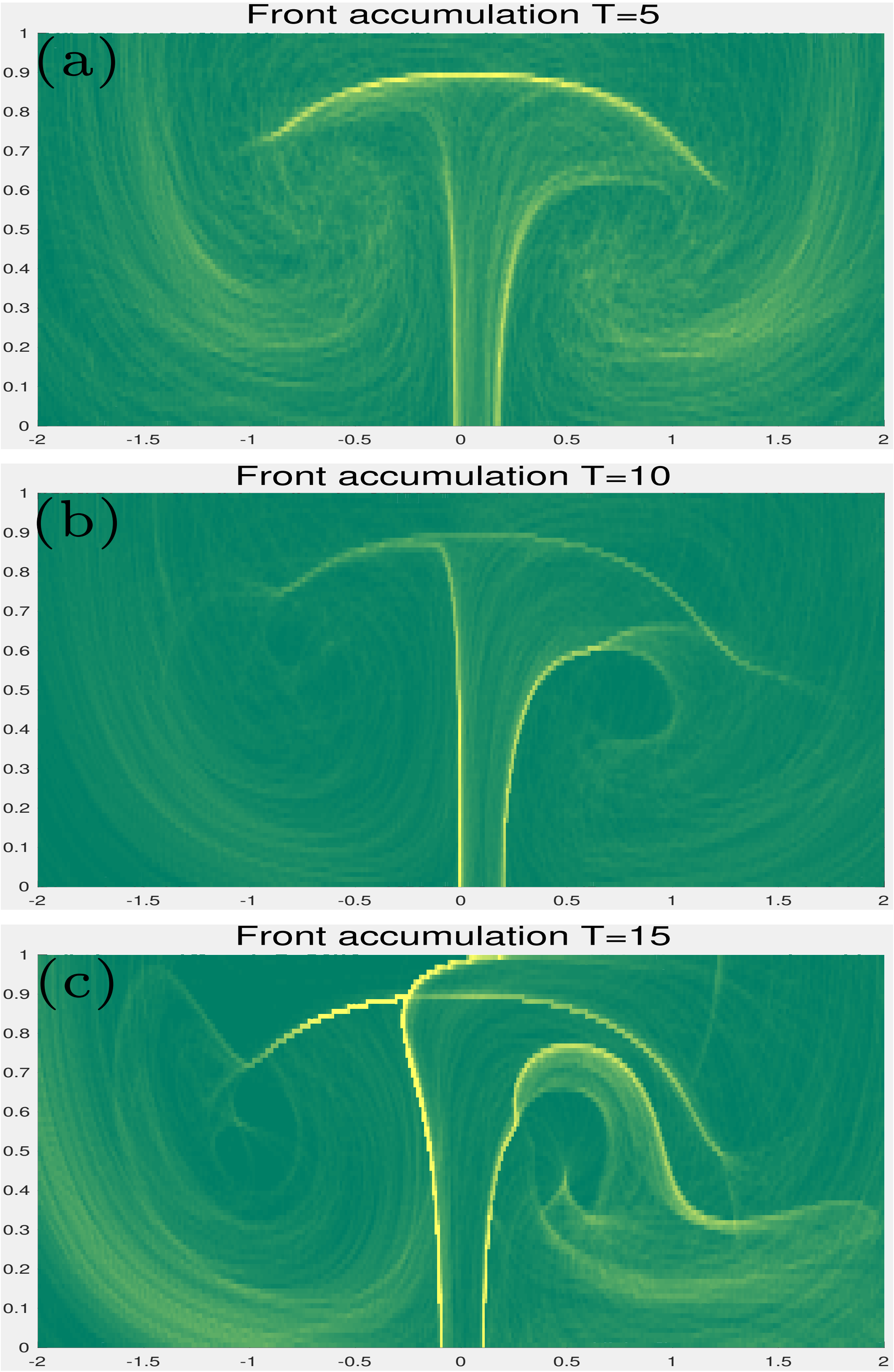

Figure 3.22. Histograms for stochastic wind (a) $[0, 5]$, (b) $[0, 10]$, and (c) $[0, 15]$.

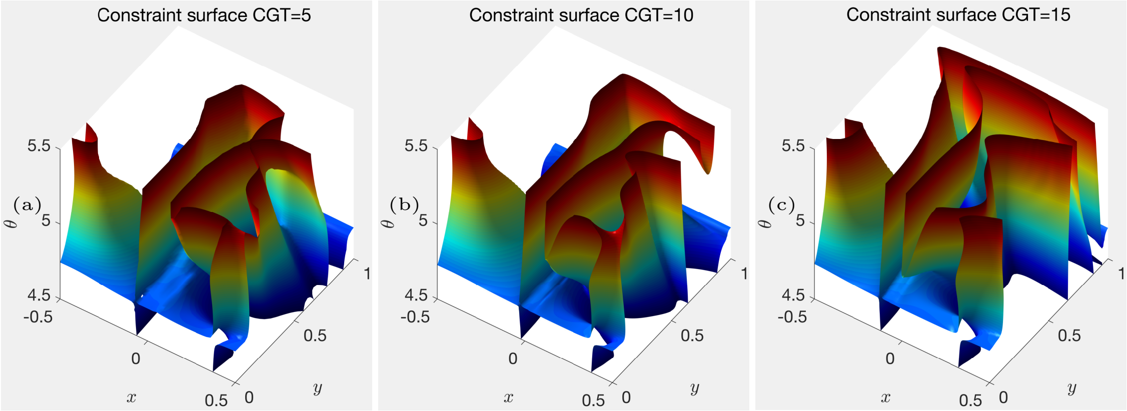

Figure 3.23. Stochastic wind shearless surface (a) $CGT = [0, 5]$, (b) $CGT = [0, 10]$, and (c) $CGT = [0, 15]$.

3.3.3 Stochastic Time Varying Wind-sliding window

Here we show in practice how one might extract a bLCS for a longer time using a sliding time window approach. We now evolve the flow forward over time interval $[0, 15]$ with the stochastic wind profile shown in fig. 3.21. This wind profile is piecewise linear with speeds above and below the burning speed $v_0 = 0.1$ resembling a swirling wind that blows on average from left to right. Fig. 3.22(a-c) shows the underlying front accumulation plots for timespans $[0, 5]$, $[0, 10]$, $[0, 15]$ respectively. Fig. 3.23(a-c) shows the shearless surface for each of the corresponding front accumulation plots in fig. 3.22. We begin by running the standard bLCS algorithm to extract, within a family of curves, the one that maximizes the normal repulsion. In this example we begin by evolving the flow from $t_0 = 0$ to $t = 5$ and extract the bLCS. The bLCS segments for the left and right curves are shown in fig. 3.24(a). Evolving the bLCS segments forward over $[5, 10]$ then over $[10, 15]$ we see good agreement with the underlying front accumulation plots fig. 3.24(b-c).

If instead you had a fluid flow that evolved for a long period of time and you wished to extract the bLCS, you could use a sliding window approach. Here you would either numerically evolve your front dynamics, or reference experimental images, for the timespan of interest, for example $[0, 100]$. Then you could use run the bLCS algorithm for a much shorter period of time, i.e. $CGT = [90, 95]$ and extract the bLCS. You could then map this curve forward under the front dynamics and find the bLCS at later time $t = 100$. This approach does have limits however. If the curve of interest is long and fills a good portion of the domain, extracting the bLCS for a shorter CGT span will result in

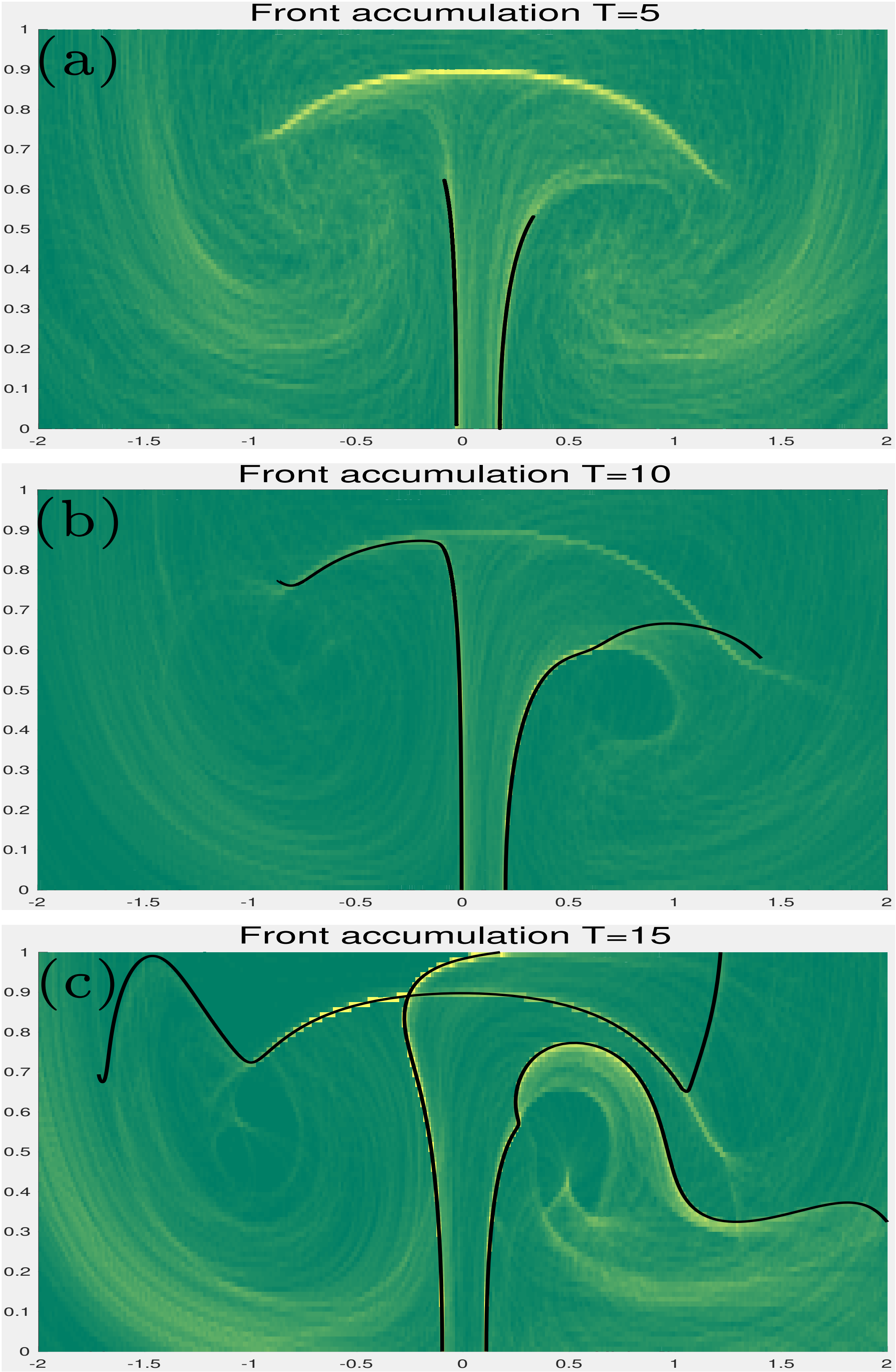

Front accumulation T=5

Front accumulation T=10

Front accumulation T=15

Figure 3.24. Histograms for stochastic wind (a) $[0, 5]$, (b) $[0, 10]$, and (c) $[0, 15]$ with bLCSs in black.

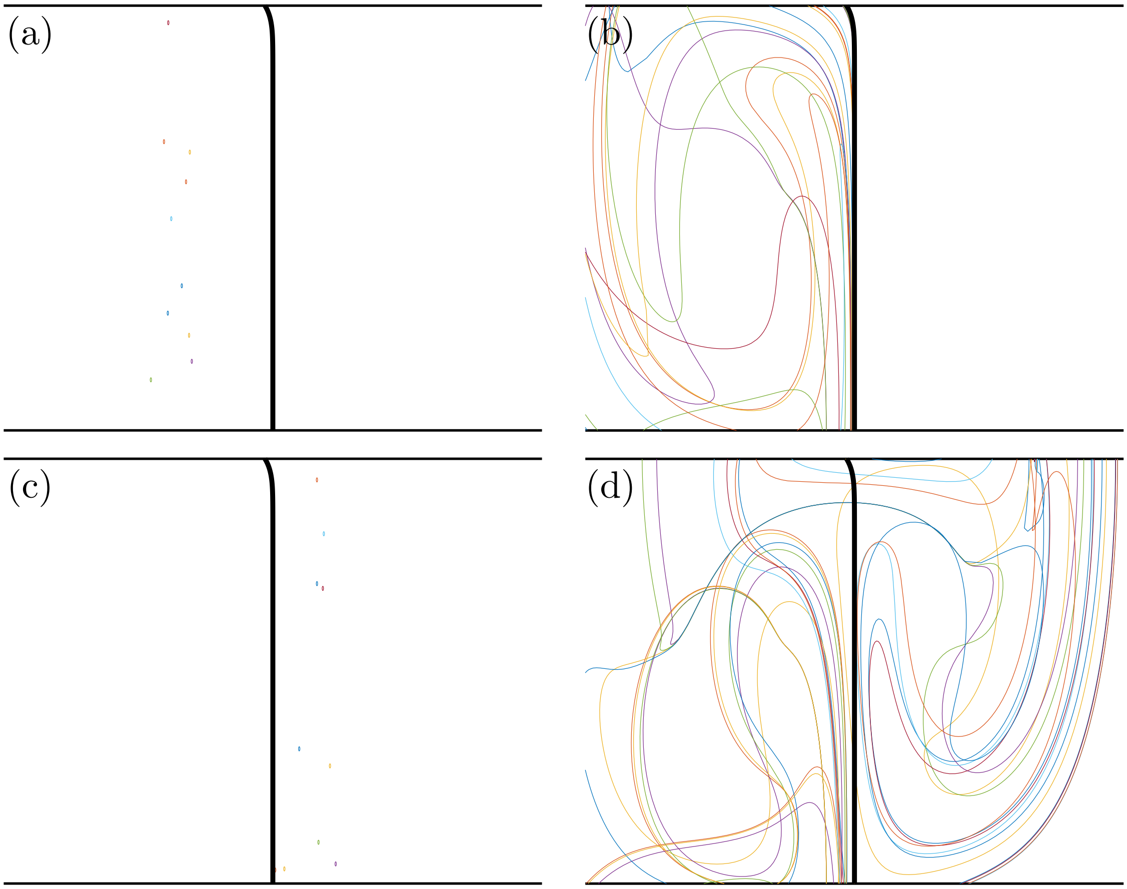

Figure 3.25. Bounding nature of bLCS for linear TV wind time interval $[0, 10]$. (a) shows point stimulations on the left side of the bLCS. (b) shows the evolution of the stimulations is (a). As expected the bLCS bounds the reactions stimulated on the left and serves as a one-sided barrier. (c-d) show the initial stimulations and their evolution. Here the reaction is stimulated to the right of the bLCS and as expected the evolution of those stimulations pass through the bLCS and fill the fluid domain. Therefore, the bLCS serves as a one-sided barrier to reaction fronts in unsteady flows in the same way that BIMs are one-sided barriers in steady flows.

a shorter curve segment and mapping this forward will also result in a longer, but shorter segment than the curve evolved for the full T span. Thus some experimentation is necessary to determine the optimal CGT span for extracting the full curve of interest.

3.4 BLCS(s) as finite time barriers to ARD systems.

3.4.1 Bounding Nature of BLCSs

In this section we want to investigate the bounding nature of a bLCSs. Do they display the same one-sided bounding behavior as the steady BIMs? We begin with the linear time-varying wind case

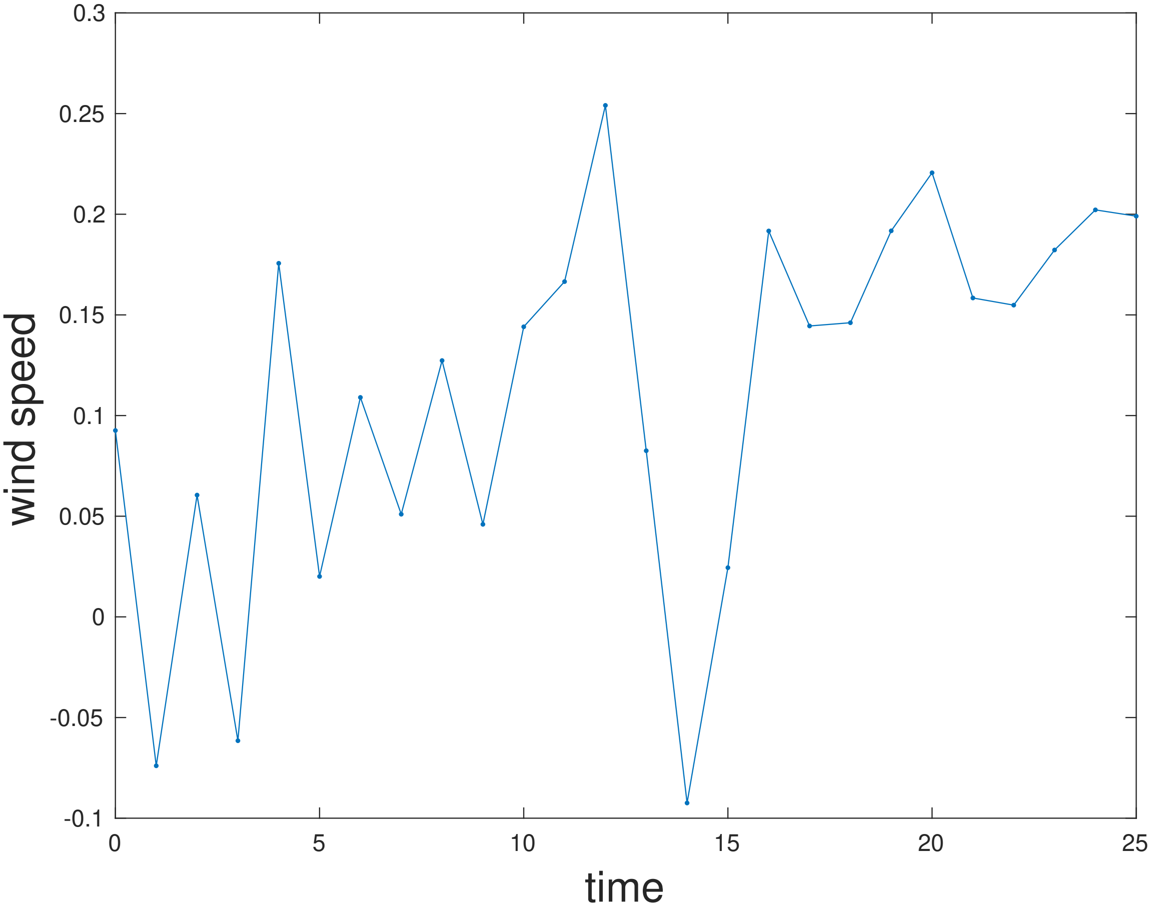

Figure 3.26. Wind profile to $t = 25$. The same profile used in Fig. 3.21 extended by 10 more time units where the magnitude was held above v_0

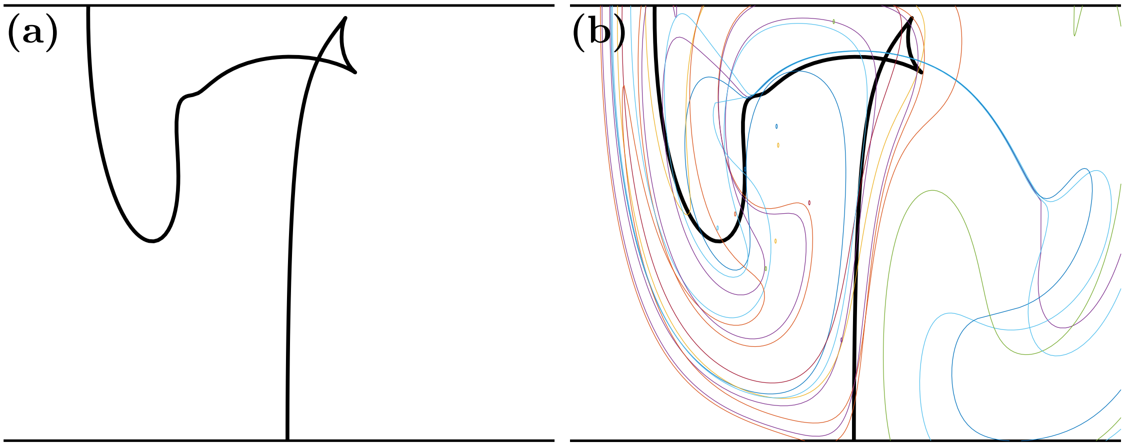

Figure 3.27. Cusp in bLCS for stochastic wind CG $t = 20$.

with a CG integration time $[0, 10$ investigated earlier in section 3.3.1. As mentioned before, this bLCS spans the channel and thus provides a means of exploring the bounding nature of a bLCS. Recall that each bLCS has a burning direction from the splitting of the advective fixed point. For this case the left bLCS has a burning direction to the left, and the bLCS has a burning direction to the right. If a reaction is stimulated to the left of the bLCS spanning the channel, this reaction should not be allowed to propagate past the bLCS if it demonstrates the same bounding nature as the BIM. Likewise if a reaction is stimulated to the right of the spanning bLCS, the reaction would eventually fill the entire domain. Figure 3.25 shows the results of simulations exploring the bounding nature of the bLCS. Fig. 3.25(a) shows point stimulations on the left side of the bLCS. Fig. 3.25(b) shows the evolution of the stimulations is (a). As expected the bLCS bounds the reactions stimulated on the left and serves as a one-sided barrier. Figs. 3.25(c-d) show the initial stimulations and evolution of those stimulations. Here the reaction is stimulated to the right of the bLCS and as expected the evolution of those stimulations pass through the bLCS and fill the fluid domain. Therefore, the bLCS serves as a one-sided barrier to reaction fronts in unsteady flows in the same way that BIMs are one-sided barriers in steady flows. Another question to be addressed, do bLCS's develop cusps similar to BIMs and if so, what happens to the bounding nature of a bLCS at a cusp? A BIM loses its bounding nature around a cusp due to its change in burning direction. To investigate this, a simulation was ran in which the stochastic wind profile over $[0, 15]$ was extended to $[0, 25]$ and the magnitude was held greater than v_0 fig. 3.26. If the wind speed was held below v_0, but still positive, no cusps developed in the bLCS. As you can see the cusps also marks the end of the bounding behavior of the bLCS.

Chapter 4

Experimental Application to Unsteady Active flow

4.1 Introduction

In chapter 3 we proposed a model for predicting reaction front propagation for unsteady fluid flows. The bLCSs are one-sided barriers to reactions fronts over a finite-time interval. We also showed that by running many simulations of reactions, stimulated randomly within the fluid domain, a histogram could be constructed showing the areas of highest attraction, i.e. front accumulation. Our results agreed nicely with the numerical simulations, but in practice we want to be able to apply this model to real world phenomena. Here we apply our model to an experimental example of an unsteady reactive flow carried out by Solomon et al. [23]. This work studied reaction front propagation in a single vortex flow with an imposed external wind.

The experimental setup consists of a rectangular box and a thin fluid layer. A round magnet, 15cm in diameter, which sits below is mounted on two perpendicular translation stages. One stage moves with a constant speed translating the vortex in space. This motion creates the same effect a stationary vortex would experience with a constant wind blowing across. On the second stage the vorticity is generated by an electrical current passing from an electrode into the fluid layer just above the magnet and another electrode surrounding the inner edge of the rectangle. Velocity field measurements were gathered using polystyrene particles and an overhead CCD camera. The contrast between the black particles and white background enabled easy particle tracking.

It was found that the radial component of the velocity field was zero. The azimuthal component followed a $1/r$ relationship up to a crossover magnet radius, r_c = 7.20 cm. The azimuthal velocity followed a third-order polynomial from r_c out to a radius of 11.47cm, denoted r_0, and was zero beyond. There were no velocity measurements taken within a centimeter of the electrode. Thus we may write

$$U_r = 0, \tag{4.1a}$$

$$U_\theta = \begin{cases} A/r & r < r_c \\ a_0 + a_1 r + a_2 r^2 + a_3 r^3 & r_c < r < r_0 \\ 0 & r > r_0 \end{cases} \tag{4.1b}$$

with $A = 0.52 cm^2, a_0 = 3.28, a_1 = -0.913, a_2 = 0.0822,$and $a_3 = -0.0024$ in units of cm/s. The velocity field is scaled by the maximum advection velocity U. The wind speeds w and burning speed v_0 are then nondimensionalized by the maximum fluid velocity, i.e.

$$v_0 = \frac{V_0}{U}, \tag{4.2a}$$

$$w = \frac{W}{U}; \tag{4.2b}$$

4.2 Reproducing Velocity Fields

It is first necessary to ensure we can numerically reproduce the underlying velocity field observed experimentally. Figure 4.1 shows the constant streamlines of the fluid flow with parameters $U = 0.14$ cm/s and $w = 0.69$. Figure 4.2(a) shows the vector field of eq. 4.1 along with streamlines. Figure 4.2(b) shows the passive invariant manifold in red. These figures show good agreement with

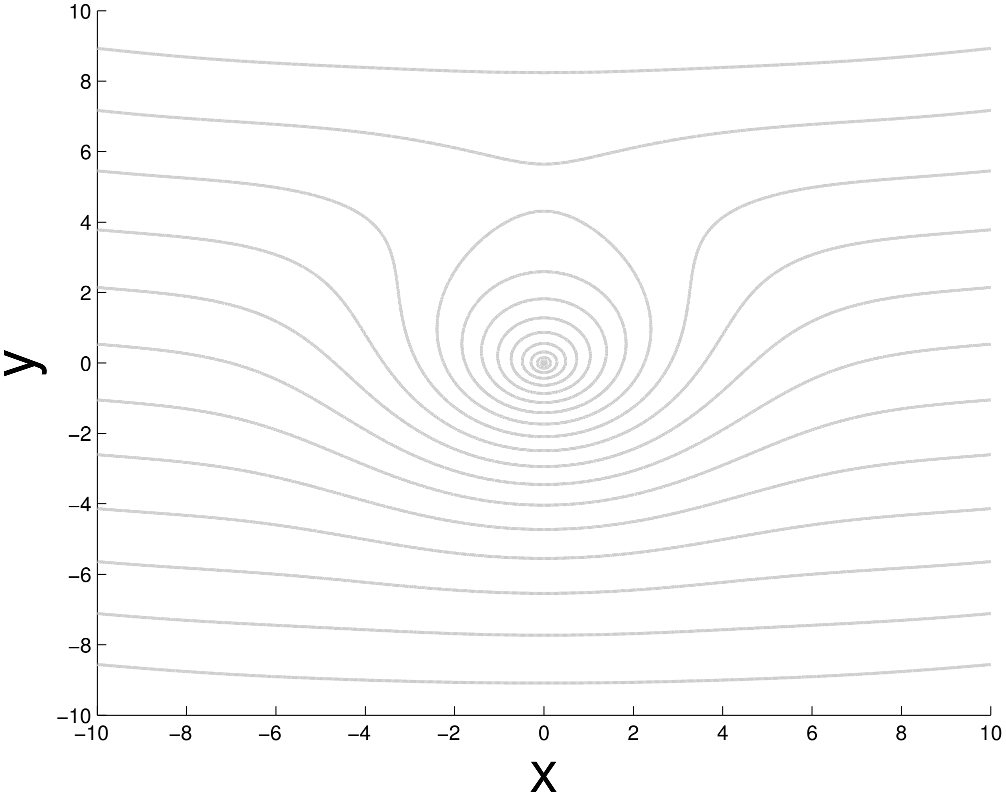

Figure 4.1. Streamlines for the velocity field with $v_w = 0.69$.

Solomon's velocity field in [23]. With the appropriate velocity field we are now able to add active enhancement to the fluid flow.

4.3 Numerical Simulations

Beginning with the steady case in which a constant wind is blowing from left to right numerical simulations were run to ensure good agreement with Solomon's experiments. Figure 4.3 shows a numerical simulations with active enhancement. In each the passive invariant manifold is shown in red and the BIM shown in black. As the burning speed v_0 increases, notice that the distance between the BIMS increases. This can be understood because as the burning speed increases, the burning fixed points move out farther along the passive invariant manifold to find a balance between the outward front propagation and the inward fluid velocity. The increase in the BIM separation

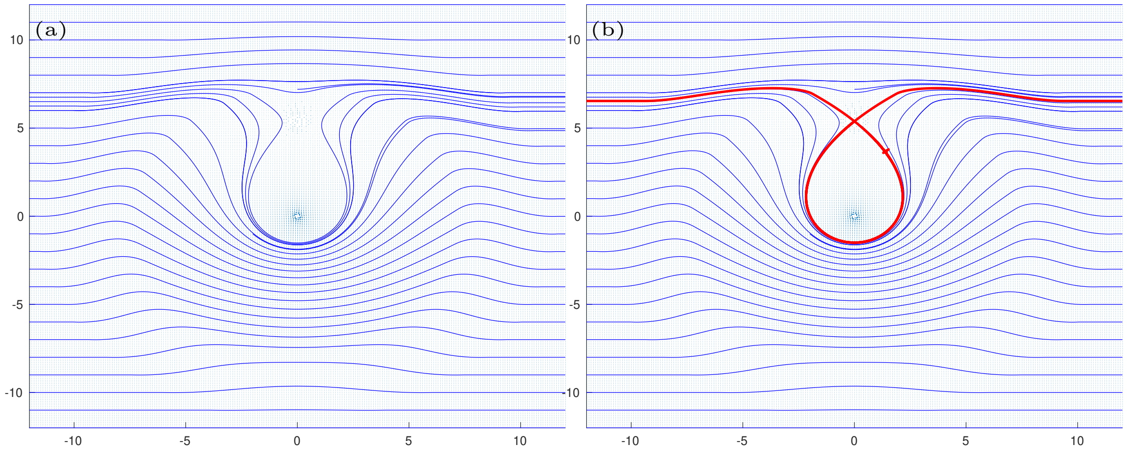

Figure 4.2. Velocity field for eq. 4.1. (a) shows the velocity field with constant streamlines. (b) shows the same velocity field with the passive invariant manifold in red.

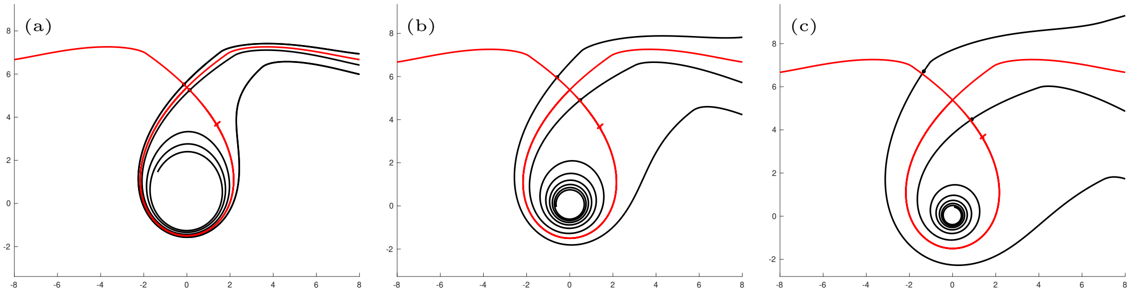

Figure 4.3. Numerical simulation using eq. 4.1 with active enhancement. BIMS shown with burning speeds (a) $v_0 = 0.024$, $(b)0.095$, and (c) 0.19 respectively.

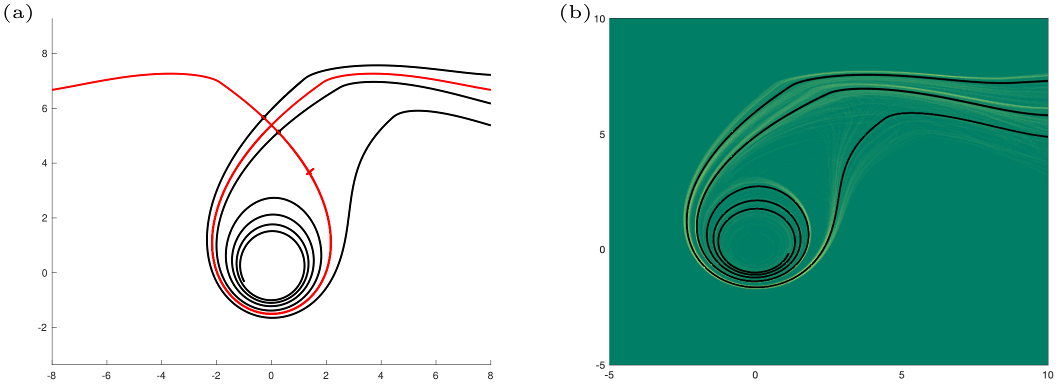

Figure 4.4. Numerical simulations of steady flow with (a) BIM along with passive invariant manifold for a burning speed of $v_0 = 0.048$, and (b) front accumulation plot for $v_0 = 0.048$ with the BIMs shown in black. This simulation was run from $t_0 = 0$ to $T = 200$.

leads to a broadening of the pinned reaction front. Again fig. 4.3 shows good agreement with Figure 7 in [23]. Figure 4.4 shows numerical simulations of steady flow with (a) BIM along with passive invariant manifold for a burning speed of $v_0 = 0.048$, and (b) front accumulation plot for $v_0 = 0.048$ with the BIMs shown in black. This simulation was run from $t_0 = 0$ to $T = 200$. Due to the nature of the BIMs being one-way barriers to reaction front propagation, the outer BIM blocks fronts from propagating outward while the inner BIM blocks only inward-propagating fronts. Thus fronts stimulated farther up wind of the front will be allowed to pass through the outer BIM, but will be blocked by the inner BIM. Conversely, a front triggered near the electrode with propagate outward through the inner BIM, but will be blocked by the outer BIM.

4.3.1 Convergence

For this system convergence to the BIMs was relatively slow. We know we should see fronts attracted to the *burning* fixed points. Here though, convergence to the bfp is slow due to the structure of the flow. Figure 4.5 shows a point stimulation at the advective fixed point for the steady case of $U = 0.14$ cm/s, $w = 0.69$ and $v_0 = 0.048$. Figure 4.5(a) shows the point stimulation evolved forward from $t_0 = 0$ to $T = 100$. Interestingly we see that the front propagates downwards towards the center of the vortex farther than out and away from the vortex. Figure 4.5 (b) shows the point stimulation evolved forward from $t_0 = 0$ to $T = 200$, here the front swiftly moves around the vortex center in the region bounded by the BIMs until either propagating outwards or further propagating towards the center. Therefore the result from the front accumulation plot in fig. 4.4(b) and the agreement with the BIM is not surprising. We notice good agreement between the two as the fronts are swept along and group towards the bottom of the vortex and agreement is not as good along the BIMs moving up and to the right. Allowing the fronts to evolved under the flow to $T = 500$ would undoubtedly show better results.

4.3.2 Aperiodic Forcing

For this experiment time-dependence was achieved by oscillating the vortex in the lateral direction in an aperiodic fashion. Though the forcing was random, data was gathered to be able to reproduce runs and have an accurate record for theoretical modeling. Figure 4.6(a) shows the

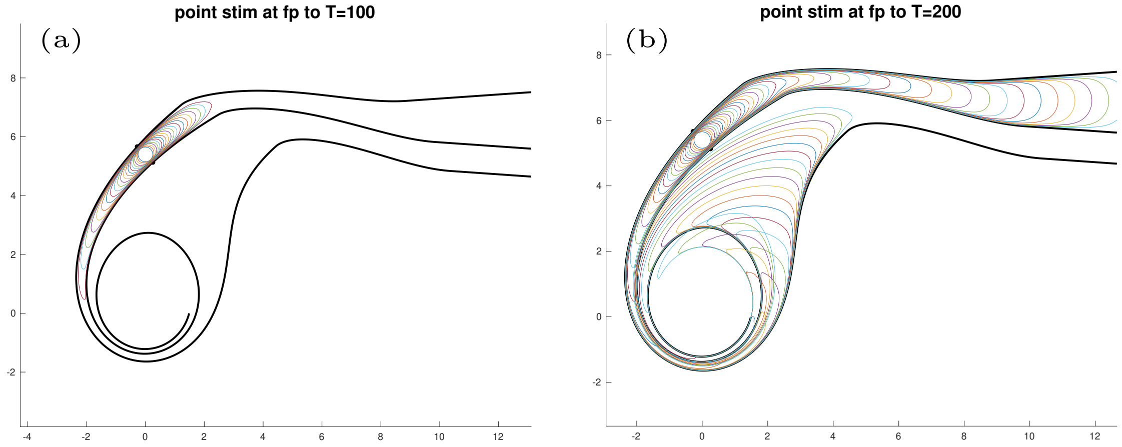

Figure 4.5. Numerical simulations of a point stimulation at the advective fixed point for the steady case of $U = 0.14$ cm/s, $w = 0.69$ and $v_0 = 0.048$. (a) Shows the point stimulation evolved forward from $t_0 = 0$ to $T = 100$. Interestingly we see that the front propagates downwards towards the center of the vortex farther than out and away from the vortex. (b) Shows the point stimulation evolved forward from $t_0 = 0$ to $T = 200$, here the front swiftly moves around the vortex center in the region bounded by the BIMs until either propagating outwards or further propagating towards the center.

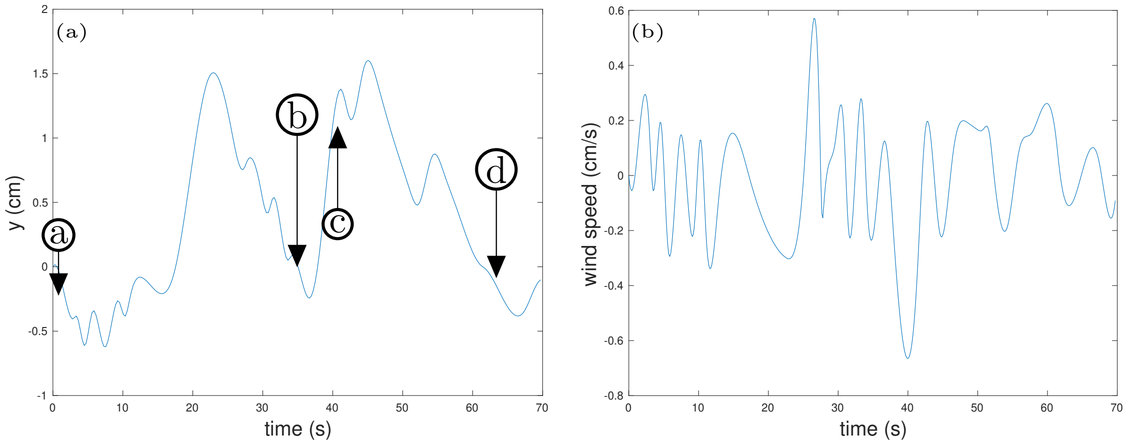

Figure 4.6. (a) The lateral (up and down) aperiodic oscillations of the vortex over time. (b) The corresponding wind speed profile in lateral direction. Note that a negative velocity of the vortex corresponds to a wind blowing in the positive direction in the reference frame of the vortex. The labels in (a) correspond to the snapshots in time taken in fig. 4.7.

position versus time data from Solomon's experiment. Figure 4.6(b) shows the velocity versus time data calculated from (a) but inverted about the time axis. This is because a negative velocity of the vortex corresponds to a wind blowing in the positive direction in the reference frame of the stationary vortex.

In this paper Solomon states that fronts were stimulated then allowed to evolve for some transient time. It was believed that Solomon stimulated a reaction then allowed the front to evolve in a steady manner that would resemble the BIM in fig. 4.4. Physically this would mean stimulating a reaction and translating the vortex in a constant manner for some transient time before enacting the lateral forcing. However, looking at fig. 4.7(a) the front has much more structure than the steady BIM and thus is it unclear what type of motion was occurring before $t = 0$. The beginning structure more closely resembles that of the periodic forcing shown by Solomon but that is only an assumption. Without knowing the exact time dependence before $t = 0$, it will be difficult to do an accurate analysis of the system in question. However, this does provide an opportunity to investigate further to what extinct is the evolution of the BIM under the aperiodic forcing a good approximation to front accumulation.

In chapter 3 we showed that extracting the bLCS for a shorter time interval, then propagating the bLCS under the flow showed good results with the front accumulation. What then can we say about taking the infinite time BIM and allowing it to propagate under an aperiodic flow? Figure 4.9 shows the evolution of the BIMs at certain time intervals with the corresponding front accumulation plot underneath. Figure 4.9(a) was run for five seconds into the aperiodic forcing, (b)-(d) for 215s, 225s, and 235s respectively. Here we find good agreement with the underlying front accumulation plots and the time evolved BIMs. Notice that for regions in which we began with good agreement with the BIMs, i.e. in fig. 4.4, that we also have good agreement with the evolved BIMs and its accompanying front accumulation plot. I believe better results could be achieved beginning with fronts evolved for a longer time during the steady case, resulting in better agreement with the BIM at $t = 0$. These results raises some interesting questions. When is it appropriate to use an evolving BIM analysis instead of the bLCS? Certainly if no steady case closely approximates the fluid flow under investigation the bLCS analysis should be used from the beginning. However if it is possible to model a flow as initially steady, calculating the BIM(s) and evolving forward under an unsteady

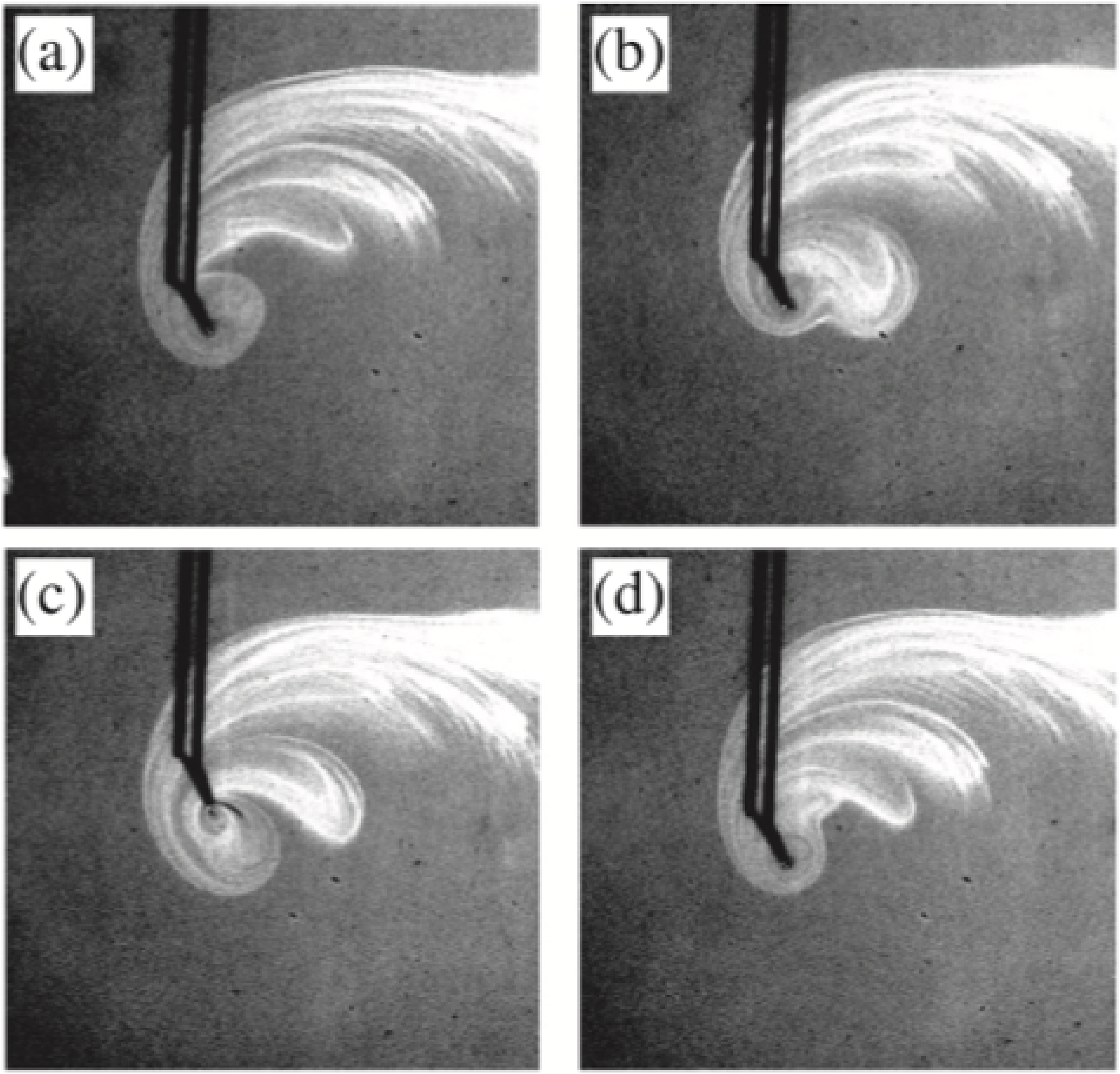

Figure 4.7. Reaction fronts in a vortex flow with aperiodic time dependence. Here the parameters are $U = 0.14$ cm/s, $w = 0.69$, $v_0 = 0.048$. The lateral oscillations have a range of 2.2cm and a standard deviation of 0.68 cm. A graph of the displacement versus time is shown in fig 4.6(a) with the corresponding snapshots labeled. This image take from Solomon et. al. [23].

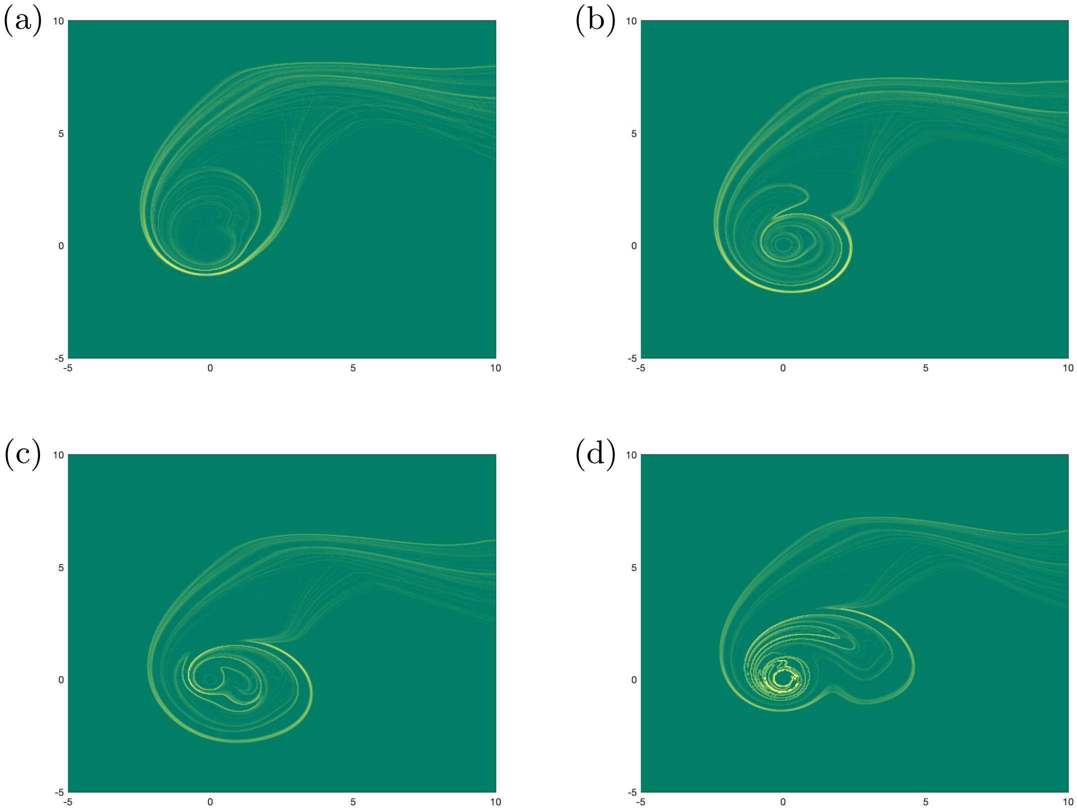

Figure 4.8. Front accumulation plots for an unsteady flow. The flow was produced by the aperiodic forcing shown in fig. 4.6. (a) shows the front accumulation at $T = 5$s. (b)-(d) show front accumulations for $T = 15$s, 25s and 35s respectively.

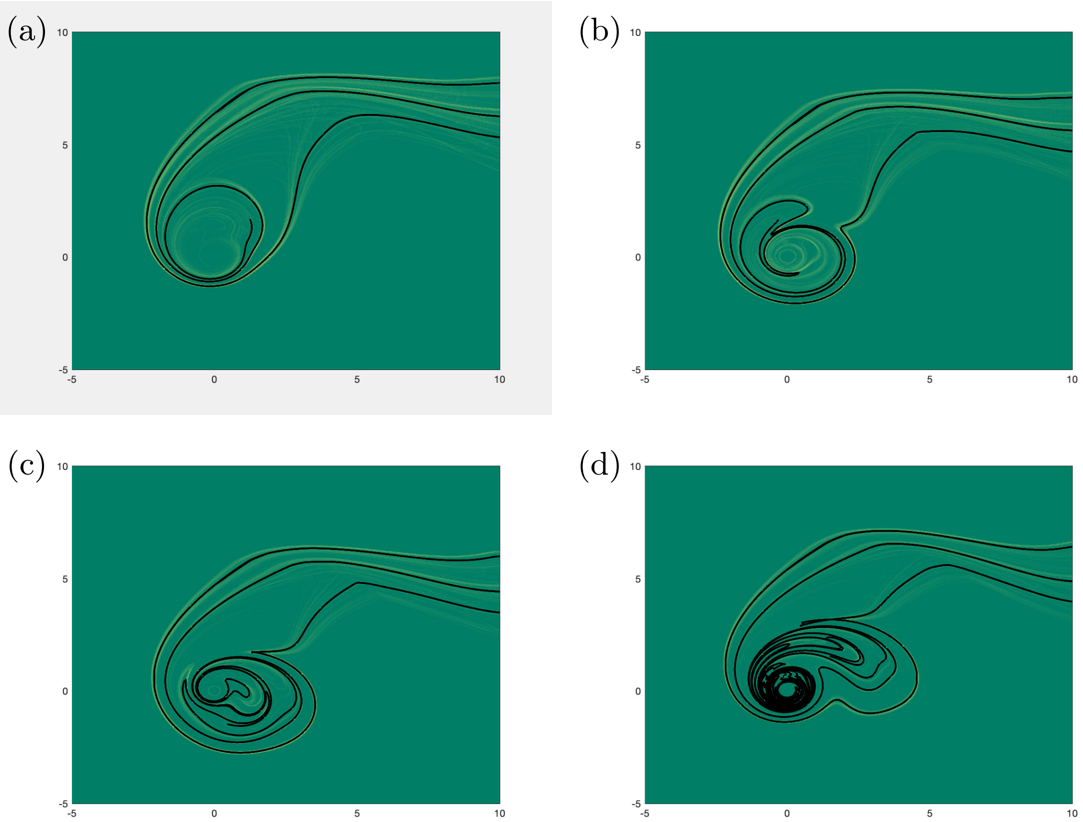

Figure 4.9. Front accumulation plots for an unsteady flow and evolved BIMs. (a) shows the front accumulation at $T = 5$s. (b)-(d) show front accumulations for $T = 15$s, 25s and 35s respectively.

flow can yield favorable results albeit under certain situations. If the aperiodic nature causes the flow to vary drastically in a short period of time, it is reasonable to assume the evolved BIM would deviate quickly from the true regions of highest attraction. If however the flow evolves slowly, as in the present case, evolving the BIM could be sufficient to capture the most attracting structures. This analysis needs further investigation to quantify when an evolved BIM versus bLCS analysis is warranted. Lastly it would be possible for Solomon et al. to run the experiment with the same forcing but beginning with a true steady case and compare with these results to see if the evolved BIMs match his experiment.

Chapter 5

Summary and Future Work

5.1 Summary

In this manuscript I have demonstrated both the *burning* invariant manifolds and *burning* Lagrangian coherent structures models for advection-reaction-diffusion systems. The BIM model is robust and provides a means of locating barriers to front elements evolving throughout a fluid. These barriers are one way due to the three-dimensional nature of the front element dynamics in a two dimensional fluid flow. Using this model we can explain a phenomenon called mode locking through the realization that each mode locked front possesses a relative periodic orbit of which the BIM is the unstable manifold attached to this RPO. The observed type of mode locking will be the one with the fastest RPO. Lastly changes in mode locking type are not due to local bifurcations of the RPO but of global bifurcations in the structure of the unstable manifold. The BIM model is only valid when the underlying fluid flow is time-periodic, as in the case of mode locking, or time-independent. Thus to move into more realistic fluid flows found in nature, another approach must be used. To solve this issue a new approach at modeling reacting fluid flows over a finite time interval with aperiodic time dependence was also presented. Here we applied the newly developed bLCS model to a few different time-dependent fluid flows. First a simple flow that linearly changed its velocity through the use of an applied "wind" and then to a stochastically changing flow represented by a swirling wind. In both cases we were able to extract the most repelling(attracting) curves within the fluid over a prescribed time interval. Also we showed that over a finite time interval the bLCSs also act as one way barriers to front propagation just like the BIMs they generalize. Lastly we sought to determine if an evolved BIM would deviate from the underlying regions of highest attraction under an aperiodic forcing. We showed that for the investigated system evolving the BIM forward in time showed good agreement with the regions of highest attraction.

5.2 Future Work

Though we have shown good results applying the bLCS model to different time aperiodic flows, much work still remains. Open questions such as the optimal time over which to integrate the shearless surface to extract the bLCS segment needs to be addressed. The shearless surface is computationally costly to calculate and visualize, and as shown in the appendix, can lead to complicated geometry as the CG integration time increases. Also a question still remains about resolution of the bLCS. If the shearless surface has three folds closely compacted to one another, do we wish to extract a bLCS for each or is it sufficient to extract one to represent that overall area as the most attracting (repelling) over that particular time interval? Another question to be addressed is how long do we need to know the velocity data to extract the bLCS at the end of time interval? For example, it was shown in chapter 3 for the linear time-varying case that the memory of the system was not long. Initial wind speeds were quickly forgotten and the bLCS more closely resembled traces of the ending wind profiles. Therefore determining an optimal time for which velocity data is needed requires further investigation. The sliding window approach of bLCS extraction can assist with this as you can extract the bLCS for a short time window and then evolve it forward under the flow. However, development of effective numerical approaches to the advection of strongly unstable bLCSs need to be addressed. The sliding window approach is also vastly more efficient in a channel flow than an open flow. In a channel flow a bLCS can be extracted for much longer than what spans the channel and once mapped forward there is no need to add points to the ends of the bLCS, infilling is sufficient to keep a smooth bLCS. In an open flow however, extracting a bLCS for a shorter time segment and mapping forward requires integrating the shearless surface at then endpoints of the bLCS and checking when there is a loss in the maximum normal repulsion. More efficient algorithms need to be developed to decrease run time. With the results in chapter 4, there are many questions that still needed answered. When is it appropriate to use an evolving BIM versus a bLCS? A few cases were commented on in the chapter but a quantitative analysis is needed. Also questions such as what if a BIM were extracted for one frozen instance in time, in the middle of an aperiodic forcing for example, then evolved forward? Would that provide good agreement with experimental observations? Finally, a solid comparison of the evolved BIM and the bLCS over the same time interval could show which method is preferred.

Chapter 6

Appendix

6.1 Mode Locking - Numerical computation of RPOs

We employ the following method for finding RPOs. For a given value of v_0, a reaction is stimulated and evolved forward until there appears to be a consistent pattern in the reaction front of some mode-locking type. We have shown in Fig. 2.4 that the convergence to the mode-locked front is fast, thus after running a simulation we can infer the mode-locking type by plotting the results similar to those shown in Fig. 2.3. To confirm our intuition we can take a front(s) and the suspected mode-locking type (N, M), and apply Eq. (2.7) to ensure the front(s) is invariant. Finally, we employ a "multishooting" approach, with M initial guesses, and Newton's method to find the RPOs for the given value of parameters. The multishooting approach and the way in which we choose the initial points are outlined below.

6.1.1 Multishooting approach

For an assumed mode-locking type (N, M), we define a map $G^{N,M} :^{3M}\rightarrow^{3M}$ which operates on a set of M points. This composite map first applies F to each of the M points. It then shifts only the Mth point backward by $2N$ vortices. Finally, the indices of the M points are cyclically permuted ($1 \rightarrow 2, \ldots, M \rightarrow 1$). We demonstrate this graphically for type (2,3) mode locking in Fig. 6.1. Each initial point (diamond) is mapped forward for one period (circle). The last point is then shifted back by $2N = 6$ vortices and the ordering of the points is cyclically permuted.

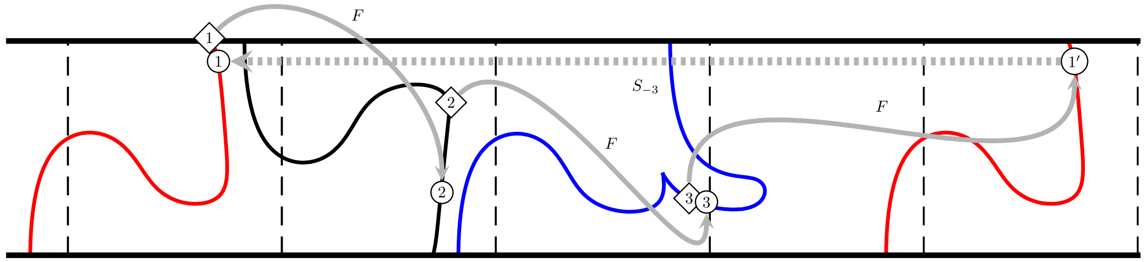

Figure 6.1. Multishooting: The diamonds represent the seeds. These points are mapped forward under F with the assumed mode-locking type, $(2, 3)$ in this example, resulting in the circles. The last point is then shifted back by $2N$ vortices. Finally to find the RPOs we take the difference between the initial and mapped forward points and use Newton's method to find the roots of this difference map.

While each point of an RPO is a fixed point of $F^{N,M}$ in ^{3}, the entire RPO is a fixed point of $G^{N,M}$ in ^{3M}. Thus in Fig. 6.1, the RPO would be a fixed point of $G^{2,3}$. To find an RPO, we use Newton's method to solve

$$G^{N,M}(\mathbf{x}) - \mathbf{x} = 0, \tag{6.1}$$

where $\mathbf{x} \in^{3M}$. The choice of the initial value, or seed, $\mathbf{x}_0$ for Newton's method must be made carefully in order to converge to the desired solution. This is outlined in Section 6.2.1.

6.1.2 Choosing initial seeds

The chaotic behavior of Newton's method dictates that we take care in choosing our seeds for solving Eq. (6.1). For example, it was found that for $(3, 5)$ mode-locking, the above method only correctly converged when the seeds were already within $1{-}4$ of the exact solution in each of the $3M$ dimensions. We employ the following algorithm to identify good seeds. First, we evolve an arbitrary front until it has converged to a mode-locked front (e.g., the blue spanning front in Fig. 6.2a). This front is then parameterized using its 2D Euclidean distance and resampled at a high density (using about 10,000 points). Maintaining this same parameterization, it is evolved forward for several more periods. (In Fig. 6.2, two is sufficient.) Due to the extreme stretching, all points on the last front (black front in Fig. 6.2a) have the same parameter value, i.e. the Euclidean distance along the original (red) curve, to within $1{-}5$ of each other. We then use any parameter value on the

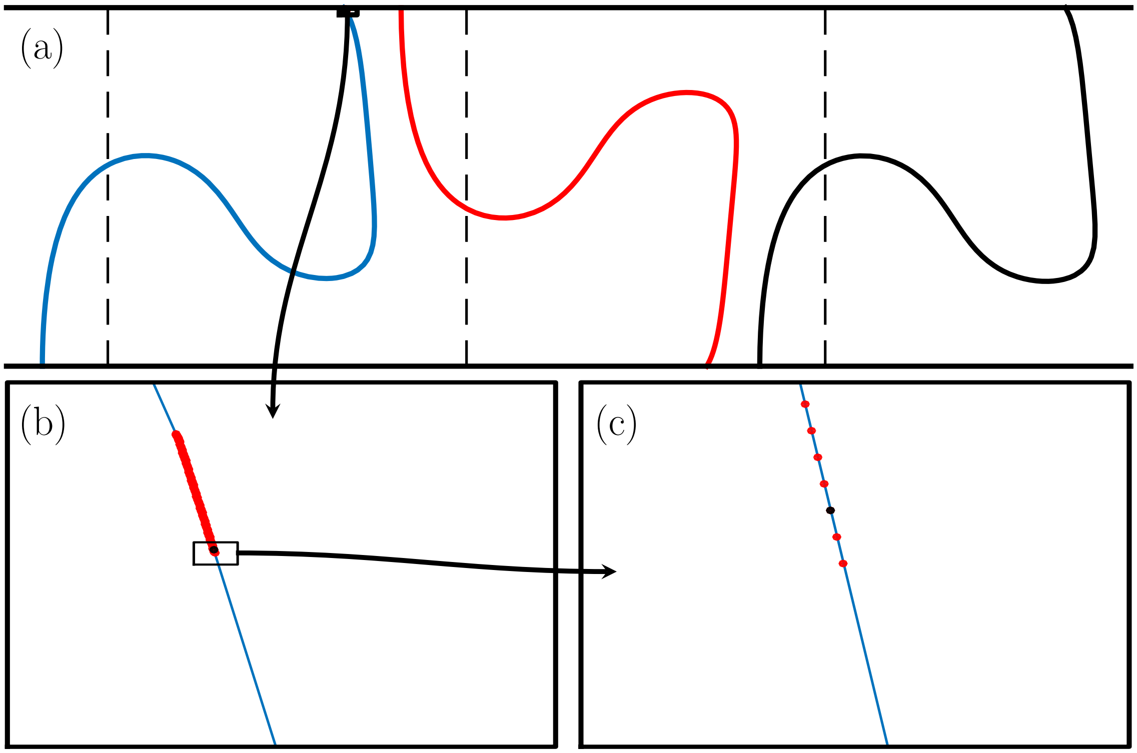

Figure 6.2. Seed Finding. Panel (a) shows mode-locking of type (1,2). The blue front is mapped forward for two periods resulting in the red and black fronts, respectively. The tiny rectangle on the blue front in (a) encompasses the points that, once mapped forward, comprise the red and black fronts. Panel (b) shows the zoomed in region in (a). Here a new rectangle encompasses the region where the black front originates. Panel (c) shows the zoomed in region in (b). The black point remaining in (c) is a good starting seed for one of the two points of the RPO.

last front (black front in Fig. 6.2a) to determine a seed point on the first parameterized front (blue front in Fig. 6.2a). For the $(2,3)$ mode-locking type, we simply used the point on the first (blue) front whose parameter value was closest to the chosen point on the last (black) front. For the higher order $(3,5)$ type, it was necessary to interpolate a point on the first parameterized front with the chosen parameter value from the last front.

This process is repeated for each successive point of the RPO for the assumed mode locking type. With this seed we then utilize the multishooting method described above to find the RPO. This method of choosing seeds provided a high chance of convergence to the correct orbit.

6.2 bLCS - Numerical Techniques for bLCS extraction.

6.2.1 Boostrapping

One method we employ in extracting bLCSs is a bootstrapping algorithm. The method is performed as follows. First once a region of interest in the fluid domain is identified, integrate the orthogonal vector field eq. 3.8, to generate a line of initial conditions. Next, integrate the tangent vector field eq. 3.10, to produce a family of curves. Here we chose a shorter integration length. Within this shorter segment of sheerless fronts, calculate the average normal repulsion along each sheerless front. Chose the bLCS as front with maximum normal repulsion. Use the end point of the BLCS segment as the new initial condition then repeat until you extract the curve of interest.

This method helps in determining clearly the end of the bLCS through the loss of a maximum in normal repulsion. Looking back at the linear time varying wind case over time interval $T = [0, 8]$ in section 3.3.1 we demonstrate our bootstrapping algorithm. Here the simulation was run in reverse time of what was previously done in section 3.3.1 , thus we are choosing to extract the attracting structure in reverse time, i.e. the most repelling structure in forward time. Figure 6.4(a) shows the statistical plot for $T = [8, 0]$ along with the bLCS segment in black, and the lines of initial conditions in red for each bootstrapping segment Figure 6.4(b) shows an inset to the statistical plot in (a) zoomed into the lower portion of the bLCS segment. Figure 6.4(c-d) shows the average normal repulsion for segments 18 and 19 respectively. Figure 6.4(c) has a clear maximum in the normal repulsion and thus a clear candidate for a bLCS segment. Going one iteration further in the boostrapping algorithm, a family of sheerless curves is found however, no clear candidate sheerless curve is identified as having a maximum normal repulsion as seen in Fig. 6.4(d). Thus we can clearly state the bLCS has terminated.

6.2.2 Artificial Dissipation

A numerical issue that can arise in extracting the bLCS is deviating from the sheerless surface. While integrating the normal and tangent vector fields for longer segments it was found that even while specifying a small integration tolerance that lifting occurred. Figure 6.5 shows an example of lifting from the sheerless surface using bootstrapping algorithm. The initial condition at top

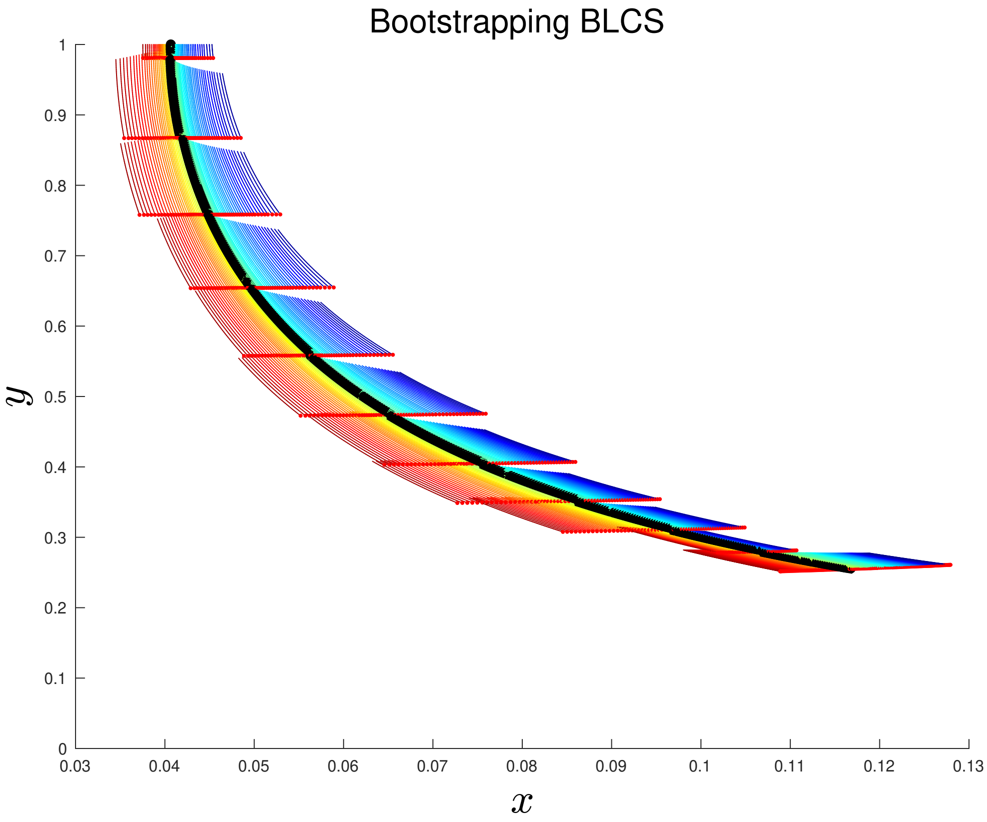

Figure 6.3. Numerical simulation demonstrating the bootstrapping algorithm. Initial segment was chosen at the bottom and integrated upwards with respect to the channel. For each line of initial conditions, shown are red points, the tangent vector field along the sheerless surface was integrated for a short segment. The curve which maximized the normal repulsion was chosen as the bLCS segment for that family of curves. The last point of the bLCS segment was then used to integrate the normal vector field in both directions for a line of initial conditions. From those initial conditions a new family of curves was found integrating the tangent vector field and the process was repeated for multiple segments until the bLCS of interest was extracted.

of the channel near $y = 0.75$ was found using newton's method. An increasing deviation from the sheerless surface was found after each subsequent segment was integrated towards the bottom. Integrating from $y = 0.75$ to $y = 0.2$, it was clear from the value of Psi the segments were no longer on the sheerless surface. One approach to ensure each segment remained on the sheerless surface was to use newton's method on the new initial condition for each bootstrapped segment. This approach will work if the sheerless surface is not complicated in the region of the new initial condition. However, if there are many neighboring branches of the sheerless surface, using newtons method may result in jumping branches, or folds, of the sheerless surface, this can be seen in fig. 6.6.

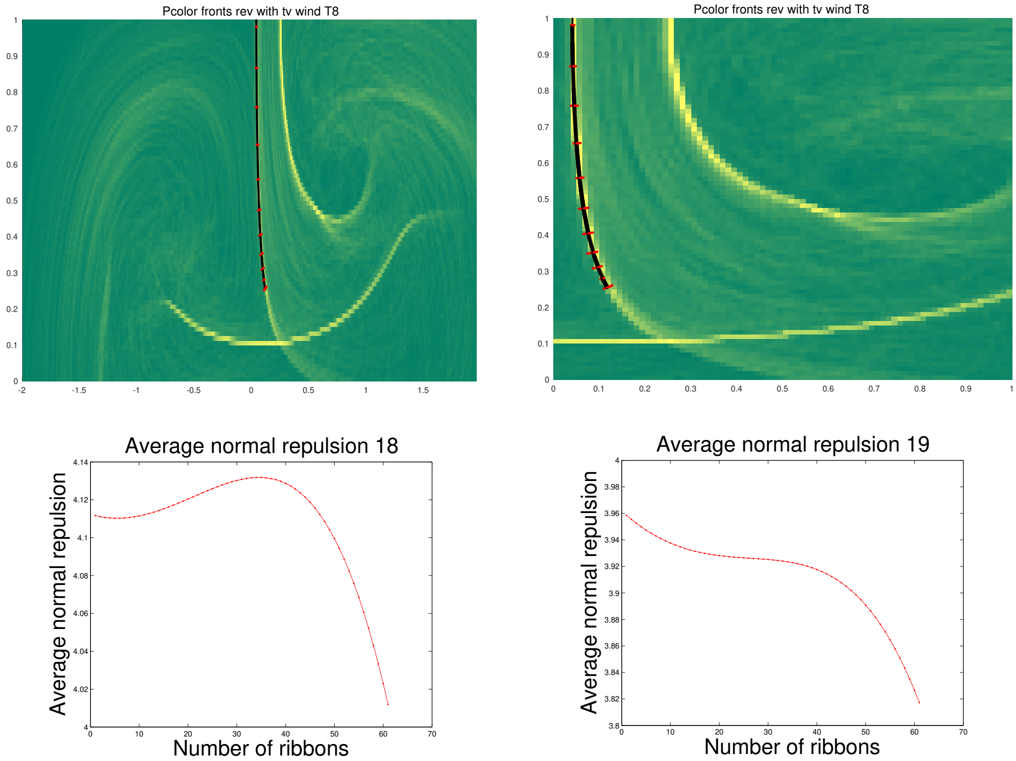

Figure 6.4. (a) shows the statistical plot for $T = [8, 0]$ along with the bLCS segment in black, and the lines of initial conditions in red for each bootstrapping segment. (b) shows an inset to the statistical plot in (a) zoomed into the lower portion of the bLCS segment. Figure 6.4(c-d) shows the average normal repulsion for segments 18 and 19 respectively. (c) has a clear maximum in the normal repulsion and thus a clear candidate for a bLCS segment. (d)Going one iteration further in the boostrapping algorithm, a family of sheerless curves is found however, no clear candidate sheerless curve is identified as having a maximum normal repulsion.

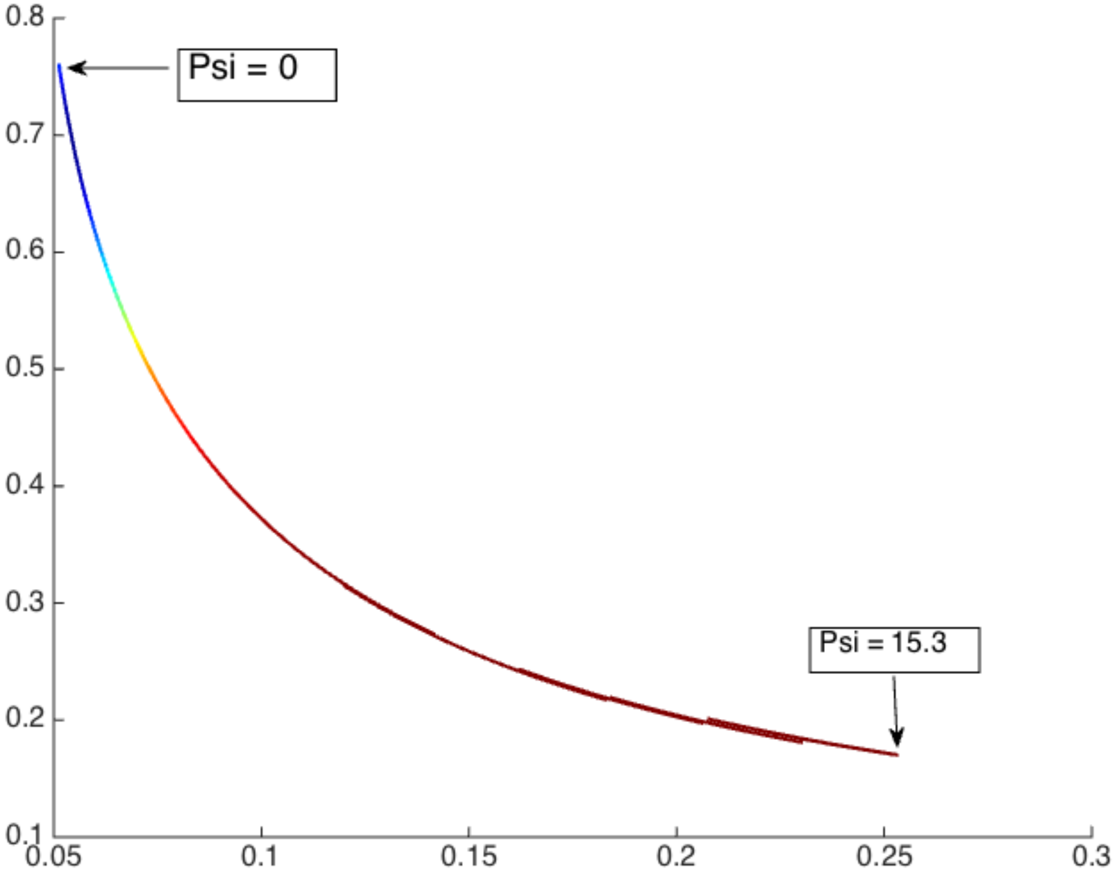

Figure 6.5. Lifting from the sheerless surface using bootstrapping algorithm. Initial condition at top of the channel near $y = 0.75$ was found using newton's method. An increasing deviation from the sheerless surface was found after each subsequent segment was integrated towards the bottom. Integrating from $y = 0.75$ to $y = 0.2$, it was clear from the value of Psi the segments were no longer on the sheerless surface.

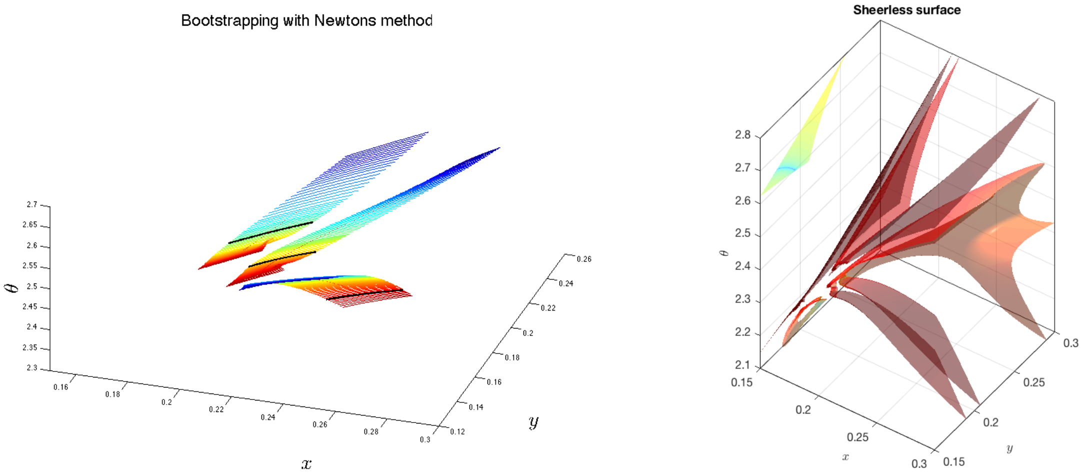

Figure 6.6. Using Newton's method on new initial condition for each bootstrapped segment. If there are many neighboring branches of the sheerless surface, using newtons method may result in jumping branches, or folds, of the sheerless surface and thus not extract the single bLCS of interest.

Bibliography

[1] M. Abel, M. Cencini, D. Vergni, and A. Vulpiani. Front propagation in laminar flows. *Phys. Rev. E*, 64(4):046307, Oct. 2001.

[2] M. Abel, M. Cencini, D. Vergni, and A. Vulpiani. Front speed enhancement in cellular flows. *Chaos*, 12(2):481–488, June 2002.

[3] E. R. Abraham. The generation of plankton patchiness by turbulent stirring. *Nature*, 391:577 EP –, 02 1998.

[4] E. R. Abraham, C. S. Law, P. W. Boyd, S. J. Lavender, M. T. Maldonado, and A. R. Bowie. Importance of stirring in the development of an iron-fertilized phytoplankton bloom. *Nature*, 407:727 EP –, 10 2000.

[5] M. R. Allshouse and T. Peacock. Lagrangian based methods for coherent structure detection. *Chaos: An Interdisciplinary Journal of Nonlinear Science*, 25(9):097617, 2018/11/01 2015.

[6] H. Aref. Stirring by chaotic advection. *Journal of Fluid Mechanics*, 143:1–21, 1984.

[7] D. J. Beebe, G. A. Mensing, and G. M. Walker. Physics and applications of microfluidics in biology. *Annual Review of Biomedical Engineering*, 4(1):261–286, 2002. PMID: 12117759.

[8] D. Beigie, A. Leonard, and S. Wiggins. Invariant manifold templates for chaotic advection. *Chaos, Solitons & Fractals*, 4(6):749–868, 1994.

[9] D. Beule, A. Forster, and T. Fricke. Simulation of ionization-front propagation in dense plasma by markoff automata. *Z. Phys. Chem*, 204(1), 1998.

[10] J. R. Blake and S. R. Otto. Ciliary propulsion, chaotic filtration and a 'blinking' stokeslet. *Journal of Engineering Mathematics*, 30(1):151–168, Mar 1996.

[11] P. W. Boyd, A. J. Watson, C. S. Law, E. R. Abraham, T. Trull, R. Murdoch, D. C. Bakker, A. R. Bowie, K. O. Buesseler, H. Chang, M. Charette, P. Croot, K. Downing, R. Frew, M. Gall, M. Hadfield, J. Hall, M. Harvey, G. Jameson, J. LaRoche, M. Liddicoat, R. Ling, M. T. Maldonado, R. M. McKay, S. Nodder, S. Pickmere, R. Pridmore, S. Rintoul, K. Safi, P. Sutton, R. Strzepek, K. Tanneberger, S. Turner, A. Waite, and J. Zeldis. A mesoscale phytoplankton bloom in the polar southern ocean stimulated by iron fertilization. *Nature*, 407(6805):695–702, Oct 2000.

[12] A. Bracco, A. Provenzale, and I. Scheuring. Mesoscale vortices and the paradox of the plankton. *Proceedings. Biological sciences*, 267(1454):1795–1800, 09 2000.

[13] J. H. E. Cartwright, M. Feingold, and O. Piro. *An Introduction to Chaotic Advection*, pages 307–342. Springer US, Boston, MA, 1999.

[14] M. Cencini, A. Torcini, D. Vergni, and A. Vulpiani. Thin front propagation in steady and unsteady cellular flows. *Phys Fluids*, 15(3):679–88, 2003.

[15] S. Chandresekhar. *Hydrodynamic and Hydromagnetic Stability*. Clarendon Press, Oxford, 1961.

[16] M. Dellnitz, O. Junge, W. S. Koon, F. Lekien, M. W. Lo, J. E. Marsden, K. Padberg, R. Preis, S. D. Ross, and B. Thiere. Transport in dynamical astronomy and multibody problems. *I. J. Bifurcation and Chaos*, 15:699–727, 2005.

[17] A. J. deMello. Control and detection of chemical reactions in microfluidic systems. *Nature*, 442:394 EP –, 07 2006.

[18] P. Dutta and R. Chevray. Enhancement of mixing by chaotic advection with diffusion. *Experimental Thermal and Fluid Science*, 11(1):1–12, 1995.

[19] S. Edouard, B. Legras, F. Lefèvre, and R. Eymard. The effect of small-scale inhomogeneities on ozone depletion in the arctic. *Nature*, 384:444 EP –, 12 1996.

[20] G. Gómez, W. S. Koon, M. W. Lo, J. E. Marsden, J. Masdemont, and S. D. Ross. Connecting orbits and invariant manifolds in the spatial restricted three-body problem. *Nonlinearity*, 17(5):1571, 2004.

[21] D. Gonze, K. Z. Coyte, L. Lahti, and K. Faust. Microbial communities as dynamical systems. *Current Opinion in Microbiology*, 44:41–49, 2018.

[22] M. GORMAN, M. EL-HAMDI, and K. A. ROBBINS. Experimental observation of ordered states of cellular flames. *Combustion Science and Technology*, 98(1-3):37–45, 06 1994.

[23] S. Gowen and T. Solomon. Experimental studies of coherent structures in an advection-reaction-diffusion system. *Chaos*, 25(8):087403, 2015.

[24] A. Hadjighasem, M. Farazmand, D. Blazevski, G. Froyland, and G. Haller. A critical comparison of lagrangian methods for coherent structure detection. *Chaos: An Interdisciplinary Journal of Nonlinear Science*, 27(5):053104, 2018/11/02 2017.

[25] G. Haller. Finding finite-time invariant manifolds in two-dimensional velocity fields. *Chaos: An Interdisciplinary Journal of Nonlinear Science*, 10(1):99–108, 2018/11/02 2000.

[26] G. Haller. A variational theory of hyperbolic lagrangian coherent structures. *Physica D: Nonlinear Phenomena*, 240(7):574–598, 2011.

[27] G. Haller and G. Yuan. Lagrangian coherent structures and mixing in two-dimensional turbulence. *Phys. D*, 147(3-4):352–370, Dec. 2000.

[28] G. Károlyi, I. Scheuring, and T. Czárán. Metabolic network dynamics in open chaotic flow. *Chaos: An Interdisciplinary Journal of Nonlinear Science*, 12(2):460–469, 2018/10/26 2002.

[29] L. H. Kellogg. Chaotic mixing in the earth's mantle. *Advances in Geophysics*, 34:1–33, 1993.

[30] I. Z. Kiss, J. H. Merkin, S. K. Scott, P. L. Simon, S. Kalliadasis, and Z. Neufeld. The structure of flame filaments in chaotic flows. *Physica D: Nonlinear Phenomena*, 176(1):67–81, 2003.

[31] A. N. Kolmogorov, I. G. Petrovskii, and N. S. Piskunov. A study of the diffusion equation with increase in the amount of substance, and its application to a biological problem. *Moscow Univ. Bull. Math*, 1:1, 1937.

[32] R. A. Locke, J. R. Mahoney, and K. A. Mitchell. Mode-locking in advection-reaction-diffusion systems: An invariant manifold perspective. *Chaos: An Interdisciplinary Journal of Nonlinear Science*, 28(1):013129, 2018/12/09 2018.

[33] R. S. Mackay, J. D. Meiss, and I. C. Percival. Transport in hamiltonian systems. *Physica D*, 13:55–81, 1984.

[34] J. Mahoney, D. Bargteil, M. Kingsbury, K. Mitchell, and T. Solomon. Invariant barriers to reactive front propagation in fluid flows. *EPL*, 98:44005, 2012.

[35] J. R. Mahoney, J. Li, C. Boyer, T. Solomon, and K. A. Mitchell. Frozen reaction fronts in steady flows: A burning-invariant-manifold perspective. *Phys. Rev. E*, 92:063005, 2015.

[36] J. R. Mahoney and K. A. Mitchell. Finite-time barriers to front propagation in two-dimensional fluid flows. *Chaos: An Interdisciplinary Journal of Nonlinear Science*, 25(8):087404, 2018/10/26 2015.

[37] J. R. Mahoney and K. A. Mitchell. A turnstile mechanism for fronts propagating in fluid flows. *Chaos*, 23:043106, 2016.

[38] A. M. Mancho, D. Small, and S. Wiggins. A tutorial on dynamical systems concepts applied to lagrangian transport in oceanic flows defined as finite time data sets: Theoretical and computational issues. *Physics Reports*, 437(3):55–124, 2006.

[39] P. Megson, M. Najarian, K. Lilienthal, and T. Solomon. Pinning of reaction fronts by burning invariant manifolds in extended flows. *Phys. Fluids*, 27:023601, 2015.

[40] M. Menzinger and A. K. Dutt. The myth of the well-stirred cstr in chemical instability experiments: the chlorite/iodide reaction. *The Journal of Physical Chemistry*, 94(11):4510–4514, 05 1990.

[41] G. Metcalfe and J. M. Ottino. Autocatalytic processes in mixing flows. *Physical Review Letters*, 72(18):2875–2878, 05 1994.

[42] K. A. Mitchell and J. Mahoney. Invariant manifolds and the geometry of front propagation in fluid flows. *Chaos*, 22(037104), 2012.

[43] J. R. Munkres. *Elements of Algebraic Topology*. Perseus Books Pub, New York, 1993.

[44] Z. Neufeld and E. Hernandez-Garcia. *Chemical and Biological Processes in Fluid Flows: A Dynamical Systems Approach*. Imperial College Press, London, 2009.

[45] G. O'Malley, M. Paoletti, M. Schwartz, and T. H. Solomon. Pinning and mode-locking of reaction fronts by vortices. *Commun Nonlinear Sci Numer Simulat*, 16:4558–4563, 2011.

[46] K. Onu, F. Huhn, and G. Haller. Lcs tool: A computational platform for lagrangian coherent structures. *Journal of Computational Science*, 7:26–36, 2015.

[47] M. S. Paoletti and T. H. Solomon. Experimental studies of front propagation and mode-locking in an advection-reaction-diffusion system. *Europhys. Lett*, 69:819, 2005.

[48] M. S. Paoletti and T. H. Solomon. Front propagation and mode-locking in an advection-reaction-diffusion system. *Phys. Rev. E*, 72:046204, 2005.

[49] T. Peacock and J. Dabiri. Introduction to focus issue: Lagrangian coherent structures. *Chaos: An Interdisciplinary Journal of Nonlinear Science*, 20(1):017501, 2018/11/01 2010.

[50] N. Peters. *Turbulent Combustion*. Cambridge University Press, Cambridge, U.K, 2000.

[51] L. F. Richardson. Atmospheric diffusion shown on a distance-neighbour graph. *Proceedings of the Royal Society of London A: Mathematical, Physical and Engineering Sciences*, 110(756):709–737, 1926.

[52] I. Scheuring, G. KÁrolyi, Á. PÉntek, T. TÉl, and Z. Toroczkai. A model for resolving the plankton paradox: coexistence in open flows. *Freshwater Biology*, 45(2):123–132, 2018/10/26 2001.

[53] I. Scheuring, G. Károlyi, Z. Toroczkai, T. Tél, and Á. Péntek. Competing populations in flows with chaotic mixing. *Theoretical Population Biology*, 63(2):77–90, 2003.

[54] A. Scotti and J. Pineda. Plankton accumulation and transport in propagating nonlinear internal fronts. *J. Mar. Res*, 65(1):117, 2007.

[55] S. Solomon. Stratospheric ozone depletion: A review of concepts and history. *Reviews of Geophysics*, 37(3):275–316, 2018/10/26 1999.

[56] T. H. Solomon and J. P. Gollub. Chaotic particle transport in time-dependent rayleigh-bénard convection. *Phys. Rev. A*, 38:6280, 1988.

[57] T. H. Solomon, S. Tomas, and J. L. Warner. Role of lobes in chaotic mixing of miscible and immiscible impurities. *Physical Review Letters*, 77(13):2682–2685, 09 1996.

[58] T. H. Solomon, S. Tomas, and J. L. Warner. Chaotic mixing of immiscible impurities in a two-dimensional flow. *Physics of Fluids*, 10(2):342–350, 2018/10/29 1998.

[59] G. I. Taylor. Statistical theory of turbulence. *Proceedings of the Royal Society of London A: Mathematical, Physical and Engineering Sciences*, 151(873):421–444, 1935.

[60] T. Tel, A. de Moura, C. Grebogi, and G. Karolyi. Chemical and biologic activity in open flows: A dynamical system approach. *Phys. Rep*, 413:91, 2005.

[61] J. Wainwright. A dynamical systems approach to bianchi cosmologies: orthogonal models of class a. *Classical and Quantum Gravity*, 6(10):1409, 1989.

[62] S. Wiggins. *Chaotic transport in dynamical systems*, volume 2. Springer Science & Business Media, 2013.

[63] F. Williams. *Combustion Theory: The Fundamental Theory of Chemically Reacting Flow Systems*. Benjamin-Cummings, 1985.

[64] X. Yao, Y. Zhang, L. Du, J. Liu, and J. Yao. Review of the applications of microreactors. *Renewable and Sustainable Energy Reviews*, 47:519 – 539, 2015.